Measurement based indoor radio channel model

Siemons, J.J.W.

Award date:
2000

Eindhoven University of Technology
Faculty of Electrical Engineering
Division of Telecommunication Technology and Electromagnetics

Measurement based indoor radio channel model

J.J.W. Siemons
Graduation Thesis

Performed at:	Philips Research Laboratories Eindhoven
Period:	September 1999 – June 2000
Graduate professor:	Prof. dr. ir. G. Brussaard (EUT)
Supervisors:	Dr. ir. P.F.M. Smulders (EUT)
	Ir. L. Leyten (Philips)
	Dr. ir. W.M.C. Dolmans (Philips)

Abstract

In present day telecommunication systems, simulations become more and more important. New concepts are simulated first to obtain the best performance before the systems are actually built. Models are used to simulate the real-life situation. Models based on measurements can be very accurate. In this work, an indoor radio channel model was built, based on measurements. The measurements were performed in one room and a frequency band of 2.0-2.4 GHz, which covers many present day telecommunication systems like DECT, UMTS and Bluetooth. The measurements, however, can be performed in arbitrary indoor environments and arbitrary frequency bands.

A database with the measurement data can be converted into a system simulator. The advantage is that the type of system simulator is independent of the database and therefore any kind of system simulator can be obtained from the measurement database.

In this report the transformation from the (measured) frequency domain to the time domain is described in detail. The processing of the measured data is performed with MATLAB. Several aspects such as aliasing and windowing are elaborated. It is shown that aliasing can be neglected and that a Gaussian window with characteristics comparable to the Hamming window can be used.

Simulations performed with three different radio channel models are presented and compared with the theory. These three models are the additive white Gaussian noise channel (AWGN), the Rayleigh flat fading channel and the two-ray model. The theoretical bit error rate of these three models is derived and compared with the results from the simulations. The simulation results for all three models agree with the theoretical bit error rate.

Subsequently a measurement-based model is obtained. Simulations were performed with this model and the bit error rate of a single carrier system for various bit rates were obtained. The simulation results show an irreducible error floor which agrees with the theory. Furthermore the simulation results show a higher bit error rate for higher bit rates, which also agrees with the theory. The model can be extended with for example multi carrier techniques like OFDM or space-time coding and the performance of these techniques can be obtained.

Finally, Gaussian pulse shaping and Raised Cosine pulse shaping are described. The pulse shape is provided by a transmit and a receive filter. The system performs best if the transfer function is equally divided between the transmit and the receive filter. In this report the impulse response of the transmit and the receive filter is derived.

Contents

1 Introduction **9**

1.1 General introduction 9

1.2 Overview of report 9

1.3 MATLAB 10

2 Indoor Radio Channel Measurements **13**

2.1 Introduction 13

2.2 XY-Table 13

2.3 Network Analyzer 14

2.4 Automation of the Measurement Setup 14

2.5 Data File 15

2.6 Measurements 15

2.7 Conclusions 17

3 Post Processing of the Measured Data **19**

3.1 Introduction 19

3.2 Power Delay Profile 19

3.3 Discrete Fourier Transforms using MATLAB 20

3.3.1 Theory 20

3.3.2 Verification of the scaling factors with a Gaussian function 22

3.3.3 Conclusion 23

3.4 Aliasing 25

3.5 Windowing 27

3.6 Conclusions 31

4 Channel Modelling **33**

4.1 Introduction 33

4.2 The Radio Channel 33

4.3 Tapped Delay Line (TDL) . . . 34
4.4 Distributions . . . 35
4.4.1 Rayleigh distribution . . . 35
4.4.2 Rician distribution . . . 35
4.5 Doppler Spread . . . 37
4.6 Determination of the weighting coefficients of the TDL as a function of time 38
4.7 Time Dispersion Parameters . . . 40
4.8 Conclusions . . . 41

5 Simulations with Radio Channel Models 43
5.1 Introduction . . . 43
5.2 Additive White Gaussian Noise (AWGN) channel . . . 43
5.2.1 Binary Phase Shift Keying (BPSK) . . . 44
5.2.2 Quadrature Phase Shift Keying (QPSK) . . . 45
5.2.3 $\pi/4$ Differential Quadrature Phase Shift Keying ($\pi/4$ DQPSK) . . . 46
5.2.4 Simulations . . . 47
5.3 Flat fading channel . . . 50
5.4 Two-ray Rayleigh fading model . . . 52
5.5 Conclusions . . . 54

6 Measurement Based Indoor Radio Channel Model 55
6.1 Introduction . . . 55
6.2 Measurement parameters . . . 55
6.3 Determination of the binwidth . . . 56
6.3.1 Rectangular pulse shape . . . 56
6.3.2 Gaussian pulse shape . . . 60
6.3.3 Conclusions . . . 60
6.4 8-bins model . . . 64
6.5 Simulations . . . 66
6.6 Conclusions . . . 67

7 Pulse Shaping 69
7.1 Introduction . . . 69
7.2 Nyquist criterion . . . 69
7.3 The Gaussian Filter . . . 69
7.3.1 Definitions . . . 69
7.3.2 Transmit and Receive Filter . . . 70

7.4 The Raised Cosine Rolloff Filter 72
7.4.1 Definitions 72
7.4.2 Transmit and Receive Filter 74
7.5 Conclusions 75

8 Conclusions and Recommendations **77**
8.1 Conclusions 77
8.2 Recommendations 77

9 Acknowledgements **79**

A Impulse response of a Raised Cosine filter with $\alpha = 0.5$ **85**

B Q-function **89**

C Pictures of the Measurement Setup **91**

D Abbreviations **93**

Chapter 1

Introduction

1.1 General introduction

One of the major obstacles to overcome when designing high bit rate data systems for indoor environments is multipath fading. Even when increasing the transmit power, the performance will be limited to the irreducible bit-error-rate. Given the extremely varied nature of the indoor environment, the characteristics of the indoor radio channel can only be determined accurately from actual propagation measurements. Therefore a measurement setup is built and the radio channel is measured with this measurement setup.

The aim of this research is to build a channel model based on measurements of the radio channel [2, 12, 13, 14, 18, 20, 21]. Since the model is based on the measurements it can be used at any frequency depending on the measured frequency band, for example 17 GHz [1, 15, 16, 17] or 60 GHz [4, 8, 10, 15, 17]. In this report a frequency band centred around 2.2 GHz is used for the measurements. With this simulation tool the performance at a particular frequency can be obtained with simulations. Multi-carrier transmission techniques like orthogonal frequency division multiplexing (OFDM) can be implemented in the model and its performance can be simulated. The measurement setup is movable and the measurement can be performed 'anywhere'. A measurement can be performed at a particular location and a model for that specific environment can easily be made.

1.2 Overview of report

In Chapter 2 the measurement setup is described. This setup consists of an XY-table with an antenna attached to it, a Network Analyzer and a personal computer with dedicated software. The data are measured in the frequency domain at different positions in the xy-plane and are saved in a file.

In Chapter 3 is explained how the measured data can be processed in order to obtain the characteristics of the indoor radio channel in the time domain. MATLAB is used to transfer the data from the frequency domain to the time domain. Furthermore, the effect of windowing and aliasing on the impulse response is described.

In Chapter 4 various theoretical issues concerning the radio channel are discussed. The mathematical description of the impulse response is presented and the implementation of

the impulse response in a tapped delay line (TDL) is described. The coefficients of the tapped delay line are stochastic variables with for example a Rayleigh or Rician distribution. These distributions as well as the determination of the coefficients are described in detail in this chapter. Finally, some time dispersion parameters are presented.

In Chapter 5 simulations performed with three different radio channel models are presented and compared with the theory. These three models are the additive white Gaussian noise channel (AWGN), the Rayleigh flat fading channel and the two-ray model. The theoretical bit error rate of these three models is derived and compared with the results from the simulations.

In Chapter 6 the measurement based model is obtained. First the binwidth and the number of bins are determined and then the coefficients of the tapped delay line are derived. Simulations are performed with this model and the bit error rate of a single carrier system for various bit rates is obtained.

Chapter 7 deals with different pulse shapes. The Gaussian pulse shape and the Raised Cosine pulse shape are described. The pulse shape is provided by a transmit and a receive filter. The system performs best if the transfer function is equally divided between the transmit and the receive filter. In this chapter the impulse response of the transmit and the receive filter is derived.

Finally, conclusions are drawn and recommendations are presented in Chapter 8.

1.3 MATLAB

The simulations described in this report are performed with MATLAB Simulink[1]. MATLAB is a high-performance language for technical computing. It integrates computation, visualisation, and programming in an environment where problems and solutions are expressed in familiar mathematical notation. Typical uses include:

- Math and computation
- Algorithm development
- Modelling, simulation, and prototyping
- Data analysis, exploration, and visualisation
- Scientific and engineering graphics
- Application development, including Graphical User Interface building

MATLAB is an interactive system which basic data element is an array that does not require dimensioning. MATLAB has evolved over a period of years with input from many users. In university environments, it is the standard instructional tool for introductory and advanced courses in mathematics, engineering, and science. MATLAB features a family of application specific solutions called toolboxes. Toolboxes are comprehensive collections of MATLAB functions (M-files) that extend the MATLAB environment to solve particular classes of problems. Areas in which toolboxes are available include communication systems, signal processing, wavelets, simulation, etc.

[1] MATLAB and Simulink are registered trademarks of The MathWorks, Inc.

Simulink, a companion program to MATLAB, is an interactive system for simulating non-linear dynamic systems. It is a graphical mouse driven program that allows modelling of a system by drawing a block diagram on the screen and manipulating it dynamically. It can work with linear, non-linear, continuous-time, discrete-time, multi-variable, and multi-rate systems. Blocksets are add-ins to Simulink that provide additional libraries of blocks for specialised applications like communications, signal processing, and power systems.

Both MATLAB and Simulink are created by The MathWorks, Inc. and are available in different versions for the MS Windows, UNIX and Macintosh operating systems. The work in this report is performed with a UNIX operating system (HP 11.0), using MATLAB version 5.3.1 and Simulink version 3.0.1. For the simulations, several blocks from the Communications toolbox (version 1.4) are used. More information on MATLAB and Simulink can be found in their respective reference manuals or at: http://www.mathworks.com.

Chapter 2

Indoor Radio Channel Measurements

2.1 Introduction

Measurements were performed earlier [3]. However, these measurements were performed in the frequency band 1.8-2.2 GHz, which is not a 'clean' frequency band, because GSM 1800 and DECT frequencies are also in this frequency band. Therefore, I had to perform the measurements again, and in a clean frequency band.

The measurement of the indoor radio channel is performed with the aid of an XY-table, a Network Analyzer and a Personal Computer with special software. The XY-table is used to perform measurements in a plane of approximately 1 m^2. The Network Analyzer sweeps through the adjusted frequency band and measures the transfer function of the radio channel. The computer controls the XY-table and saves the measured data in a file yielding a two-dimensional array of complex row vectors. Detailed information about the measurement setup can be found in [3].

2.2 XY-Table

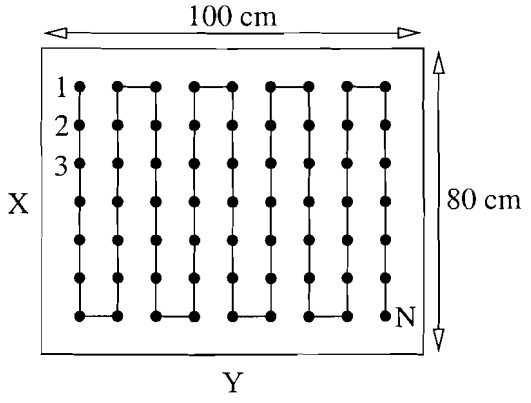

Figure 2.1: **XY-table.**

The XY-table is shown in Figure 2.1. The XY-table is a rectangular table of 80 cm in the x-direction and 100 cm in the y-direction. The measurement setup is shown in Figure 2.2 and in Appendix C. The XY-table works as follows: A beam that can move in the x-direction is mounted on the XY-table. A small table is attached to the beam and is able to move over the beam in the Y-direction. A non-conducting bar with a length of approximately 1 meter is fixed on the small table (in vertical position). One of the antennas (transmit / receive) can be fixed on top of this bar. The XY-table can be controlled by means of a XY-table controller and a computer with special software. The number of points in the X- and Y-direction can be chosen as well as the number of frequency steps per frequency sweep.

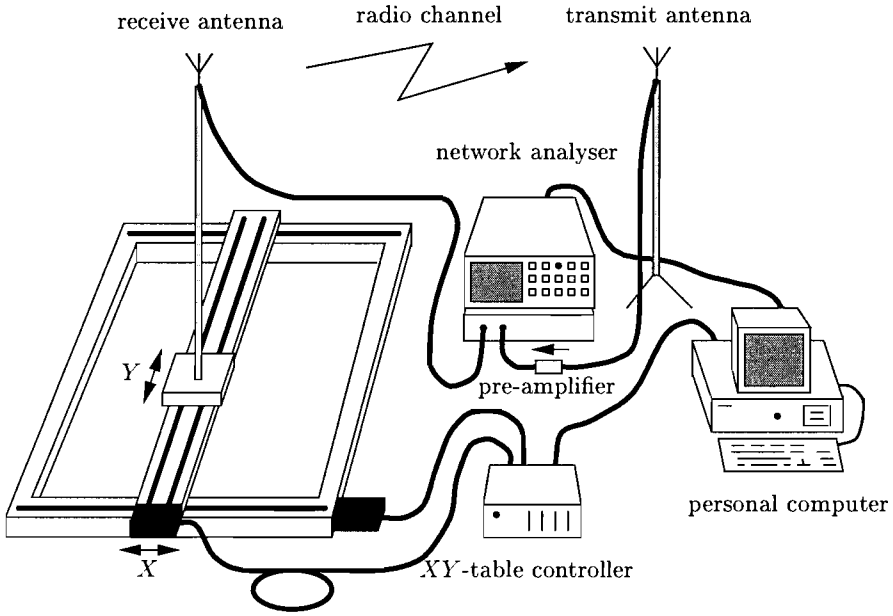

Figure 2.2: **Measurement setup.**

2.3 Network Analyzer

A Network Analyzer is used to measure the transfer function of the radio channel in the frequency domain. The start frequency, stop frequency and the frequency steps can be adjusted. The analyzer sweeps through the adjusted frequency domain and determines the transfer function at each point on the XY-table. The analyzer is able to obtain the actual transfer function without the cable characteristics and the connections. The network analyzer is a HP 8753E and is a high performance vector network analyzer. A picture of the network analyzer is shown in Appendix C.

2.4 Automation of the Measurement Setup

Hewlett-Packard Visual Engineering Environment (HP VEE) is a graphic programming language, which is designed especially to control measurement instruments. Using this

software the XY-table can be controlled [3]. The different parameters that can be adjusted for the measurement are:

- Number of points per (frequency) sweep (K).
- Number of points on the XY-table (N).
- Start- and stop frequency.
- Usage of a power amplifier? (YES/NO)
- Names and locations of the data files.

2.5 Data File

The measured data are saved in a file. These data are complex values. The meaning of these complex values will be explained later. The data are saved in a file in the form

$$\left(\overbrace{f_1, f_2, \ldots, f_K}^{point1}, \overbrace{f_1, f_2, \ldots, f_K}^{point2}, \ldots\ldots\ldots, \overbrace{f_1, f_2, \ldots, f_K}^{pointN} \right) \quad , \tag{2.1}$$

where the first point in the array is the complex transfer value at the first point in the XY-plane at the start frequency. The last point in the array is the complex transfer value at the last point in the XY-plane at the stop frequency. The measurement is finished now and the data can be processed with computer programs, for example MATLAB.

NOTE:
The data are saved with a DOS format. If a UNIX system is used to process the data, the data have to be transformed to UNIX format before processing.

2.6 Measurements

Measurement 1:
This measurement is performed in the large measure room at the fifth floor of building WAY of Philips NATLAB. The measurement is a line of sight (LOS) measurement and the measured frequency band is 2.0-2.4 GHz. The specifications of this measurement are shown in the second column of Table 2.1.

Measurement 2:
This measurement is performed in room 5.76 at the fifth floor of building WAY of Philips NATLAB. The measurement is a non line of sight (NLOS) measurement and measured frequency band is 2.18-2.22 GHz. The specifications of this measurement are shown in the third column of Table 2.1.

Measurement 3:
This measurement is performed at the same location as measurement 2, but with a larger bandwidth (400 MHz instead of 40 MHz). The specifications of this measurement are shown in the fourth column of Table 2.1.

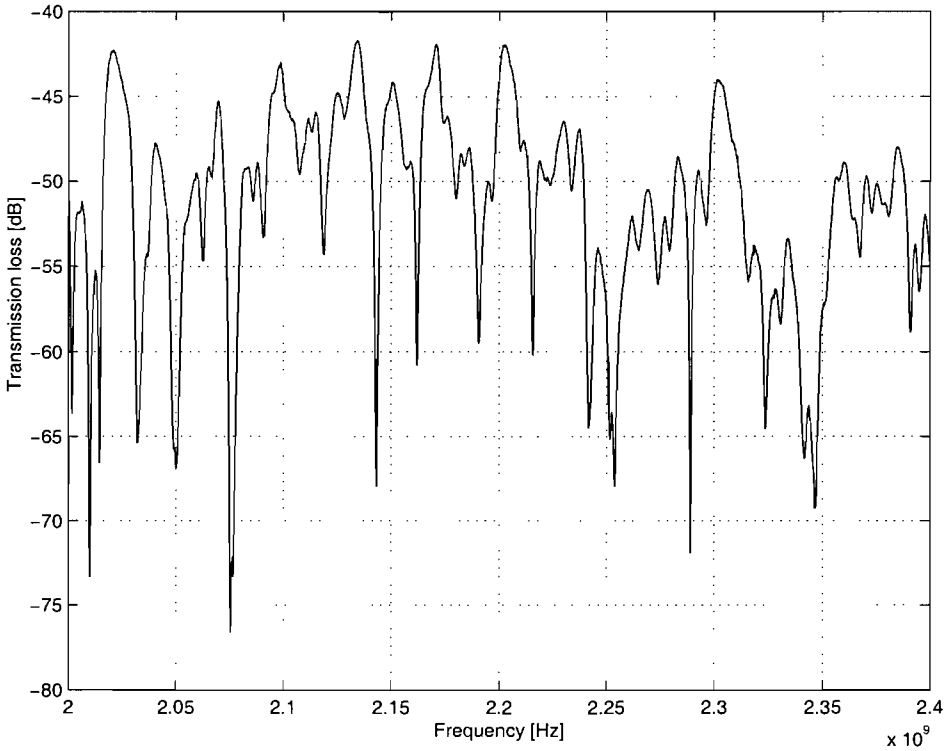

Figure 2.3: **Measurement 1 at one position in the xy-plane.**

Table 2.1: **Specifications of the measurements.**

Parameter	**Measurement 1**	**Measurement 2**	**Measurement 3**
Place	Measure Room, WAY5	WAY 5.76	WAY 5.76
Type	Line Of Sight	Non Line Of Sight	Non Line Of Sight
Distance Tx-Rx	12 m	2-3 m	2-3 m
Frequency	2.0 - 2.4 GHz	2.18 - 2.22 GHz	2.0 - 2.4 GHz
Points/Frequency sweep	1601	1601	1601
Wavelengths in x-direction	3	3	3
Wavelengths in y-direction	3	3	3
Points/wavelength	16	16	16
Points in xy-plane	2401	2401	2401
Source Power	10 dBm	10 dBm	10 dBm
Calibration file	jap1	jap2	jap1
Date of measurement	4-2-2000	9-2-2000	10-2-2000
Data file	meting5b.dat	meting10.dat	meting11.dat
Position Rx	east side of the room	WAY 5.76	WAY 5.76
Position Tx	west side of the room	WAY 5.74	WAY 5.74
Height Rx and Tx	2 m	2 m	2 m
Polarisation Rx and Tx	Vertical	Vertical	Vertical

An example of measurement 1 at a certain position in the xy-plane is shown in Figure 2.3. In the figure it can be seen that the difference between the maximum and the minimum transmission loss is approximately 35 dB. The indoor radio channel is frequency selective within the measured bandwidth.

2.7 Conclusions

Measurements are performed and the transfer function of the indoor radio channel is known at each (measured) position in the xy-plane. It has been found that the difference between the minimum and maximum transmission loss is approximately 35 dB (Figure 2.3). The measured data can be used to model the indoor radio channel.

Chapter 3

Post Processing of the Measured Data

3.1 Introduction

In the previous chapter it is described how the measurement is performed and the data are saved in a data file. In this chapter it is described how the measured data are post processed in such a way that they become suitable for implementation in a system simulator.

First, the transform from frequency domain to time domain in general is explained (section 3.2). After that, differences between discrete Fourier transforms (DFT) in MATLAB and continuous Fourier transforms (FT) are shown (section 3.3). In section 3.4 the effect of aliasing is explained in detail. Finally, the use of windows is discussed (section 3.5).

3.2 Power Delay Profile

An indoor radio channel can be described in the frequency domain and in the time domain. Fourier transforms are used to transform from one domain into the other. The Fourier transforms are defined below:

Fourier Transforms

$$h(t) = \int_{-\infty}^{+\infty} H(f) \cdot e^{j2\pi ft}\, df \quad \Longleftrightarrow \quad H(f) = \int_{-\infty}^{+\infty} h(t) \cdot e^{-j2\pi ft}\, dt \tag{3.1}$$

$$h(t) = \frac{1}{2\pi} \int_{-\infty}^{+\infty} H(\omega) \cdot e^{j\omega t}\, d\omega \quad \Longleftrightarrow \quad H(\omega) = \int_{-\infty}^{+\infty} h(t) e^{-j\omega t}\, dt \tag{3.2}$$

Time	$\Longrightarrow$	Frequency	= Fourier Transform (FT)
Frequency	$\Longrightarrow$	Time	= Inverse Fourier Transform (IFT)

The transfer function *H(f)* is determined by measuring the received power as a function of frequency as explained in the previous chapter. The impulse response *h(t)* can be obtained by means of the inverse Fourier transform (IFT). From the impulse response, the power

delay profile (PDP) in dB can be calculated as

$$PDP = 20 \cdot \log|h(t)| \quad . \tag{3.3}$$

3.3 Discrete Fourier Transforms using MATLAB

A computer program, MATLAB in our case, is used to calculate the Fourier transforms. The differences between the continuous Fourier transform and the discrete Fourier transform in MATLAB are described in this section. The scaling factors are derived and verified with simulations.

3.3.1 Theory

The discrete Fourier transforms are described as:

Discrete Fourier Transform (DFT)

$$h_p[n] = \frac{1}{N}\sum_{k=0}^{N-1} H_p[k] \cdot e^{j\left(\frac{2\pi}{N}\right)kn} \tag{3.4}$$

Discrete Inverse Fourier Transform (DIFT)

$$H_p[k] = \sum_{n=0}^{N-1} h_p[n] \cdot e^{-j\left(\frac{2\pi}{N}\right)kn} \tag{3.5}$$

where

- k = 0,1,2, ... ,...N-1
- n = 0,1,2, ... ,...N-1

and N is the total number of points.

In MATLAB the transforms are defined as

$$h_p[n] = \frac{1}{N}\sum_{k=1}^{N} H_p[k] \cdot e^{j\left(\frac{2\pi}{N}\right)(k-1)(n-1)} \tag{3.6}$$

$$H_p[k] = \sum_{n=1}^{N} h_p[n] \cdot e^{-j\left(\frac{2\pi}{N}\right)(k-1)(n-1)} \tag{3.7}$$

with k = 1,2,3, ... ,...N and n = 1,2,3,... ... ,N.

The only difference between the discrete Fourier transforms and the transforms in MATLAB is that 'k' and 'n' start at '1' in MATLAB instead of '0'. This is because the first point in an array in MATLAB has number 1; for example $H[1]$ and not $H[0]$. From now on (3.4) and (3.5) are used as the Fourier transforms in MATLAB. Now we have to find out what the difference between the (continuous) Fourier transforms and the discrete Fourier

Table 3.1: **Parameters for discrete Fourier Transforms.**

Frequency	**Time**
k=0,1,2, ... ,N-1	n=0,1,2, ... ,N-1
Frequency steps = Δf	Time steps = Δt
Bandwidth (BW) = (N-1) $\cdot\Delta f$	Total time (T) = (N-1) $\cdot\Delta t$
$f_k = k \cdot \Delta f$	$t_n = n \cdot \Delta t$

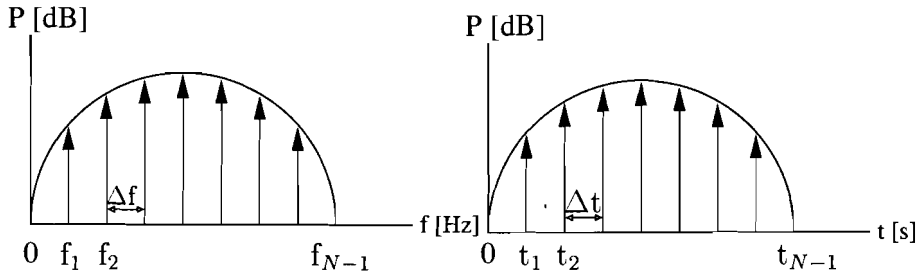

(a) Frequency Domain (b) Time domain

Figure 3.1: **Time and Frequency Domain figures for discrete Fourier Transforms.**

transforms is. The parameters for the discrete Fourier transforms and the corresponding figures are shown in Table 3.1 and Figure 3.1.

Analysis:
We start this analysis with the (continuous) Fourier transform of (3.1)

$$h(t) = \int_{-\infty}^{+\infty} H(f) \cdot e^{j2\pi ft}\, df \quad . \tag{3.8}$$

With the Trapezium Rule we can calculate the (discrete) integral of *H(f)* as

$$\int_{-\infty}^{+\infty} H(f) \cdot df \quad \rightarrow \quad \Delta f \cdot \left[\frac{1}{2}H(0) + H(k \cdot \Delta f) + \frac{1}{2}H\{(N-1) \cdot \Delta f\}\right] \quad , \tag{3.9}$$

with k=1,2,3, ... ,N-2.

We use a window (for example a Gaussian window) to suppress the edges and therefore *H(0)* and *H{(N-1)* $\cdot\Delta f$*}* can be neglected and thus

$$\int_{-\infty}^{+\infty} H(f) \cdot df \quad \rightarrow \quad \sum_{k=0}^{N-1} \Delta f \cdot H(k \cdot \Delta f) \quad , \tag{3.10}$$

and the impulse response is defined as

$$h(t) = \sum_{k=0}^{N-1} \Delta f \cdot H(k \cdot \Delta f) \cdot e^{j2\pi k \Delta f t} \quad . \tag{3.11}$$

With a discrete time ($t = n \cdot \Delta t$), the impulse response becomes

$$h(n \cdot \Delta t) = \sum_{k=0}^{N-1} \Delta f \cdot H(k \cdot \Delta f) \cdot e^{j2\pi k \Delta f n \Delta t} \quad . \tag{3.12}$$

If we choose $1/N = \Delta t \cdot \Delta f$ the impulse response becomes

$$h(n \cdot \Delta t) = \sum_{k=0}^{N-1} \Delta f \cdot H(k \cdot \Delta f) \cdot e^{j\frac{2\pi kn}{N}} \quad . \tag{3.13}$$

In MATLAB the DIFT is defined in (3.4) as

$$h_p[n] = \frac{1}{N} \sum_{k=0}^{N-1} H_p[k] \cdot e^{j(\frac{2\pi}{N})kn} \quad . \tag{3.14}$$

The MATLAB DIFT (3.14) has to be multiplied by $N \cdot \Delta f$ in order to obtain (3.13). The scaling factor for the MATLAB DFT can be found in the same way and is Δt.

Conclusion:
MATLAB can be used to perform Fourier Transforms if we multiply the results with the scaling factors shown in Table 3.2.

Table 3.2: **Scaling Factors for Fourier Transforms.**

Transform	Scaling Factor
MATLAB DIFT	$N \cdot \Delta f$
MATLAB DFT	Δt

3.3.2 Verification of the scaling factors with a Gaussian function

In this section the scaling factors obtained by the analysis in the previous section are verified by simulations in MATLAB. A function for which the transformation can analytically be derived in both domains is used to perform the Fourier transforms with. In this case the Gaussian function is used. The Gaussian function is described in the frequency domain as shown in (3.15) and in the time domain as shown in (3.16).

$$V(\omega) = -\frac{j\sqrt{\pi}}{2a}\left(e^{-\left(\frac{\omega-\omega_0}{2a}\right)^2} - e^{-\left(\frac{\omega+\omega_0}{2a}\right)^2}\right) \cdot e^{-j\omega\tau} \tag{3.15}$$

$$v(t) = \Re\left(e^{-a^2 \cdot (t-\tau)^2} \cdot e^{j\omega_0 \cdot (t-\tau)}\right) \quad , \tag{3.16}$$

where $\Re$ denotes the real part, ω_0 is the centre frequency in radians of the pulse in the frequency domain and τ is centre time of the pulse in the time domain. Parameter 'a' is defined as

$$\Delta f_{-60dB} = 1.67 \cdot a \quad , \tag{3.17}$$

and

$$\Delta t_{-60dB} = \frac{5.26}{a} \quad , \tag{3.18}$$

where Δf_{-60dB} is the filter bandwidth were the amplitude is 60 dB lower than the maximum, and Δt_{-60dB} is the pulse width, were the amplitude is 60 dB lower than the maximum. The pulses are cut off at the -60 dB points to obtain a finite time and frequency in order to implement it in a computer.

In MATLAB only positive frequencies are used. In that case the Gaussian filter $V(\omega)$ becomes

$$V(\omega) = -\frac{j\sqrt{\pi}}{2a}\left(e^{-\left(\frac{\omega-\omega_0}{2a}\right)^2}\right) \cdot e^{-j\omega\tau} \quad . \tag{3.19}$$

Taking the inverse Fourier transform of this function will result in a complex time signal. The real time signal, v(t), is the envelope of this complex signal and is

$$v(t) = \sqrt{v_R(t)^2 + v_I(t)^2} \quad , \tag{3.20}$$

where $v_R(t)$ is the real part and $v_I(t)$ is the imaginary part of the complex time signal.

The parameters and its values are shown in Table 3.3. F_0 is the centre frequency in Hz. In Figure 3.3.3 the Fourier Transforms performed with MATLAB are plotted. In Figure a

Table 3.3: **Parameters Gaussian function.**

Parameters	Value	Unity
τ	4×10^{-7}	[s]
Δf_{-60dB}	400	[MHz]
F_0	1.8	[GHz]
ω_0	11.3×10^9	[rad]
a	2.395×10^8	
Δt_{-60dB}	2.196×10^{-8}	[s]
Amplitude in time	1	
Amplitude in frequency	7.4×10^{-9}	

the analytical Gaussian function in the frequency domain is plotted. In Figure b the DIFT from Figure a with the scaling factor is shown. In Figure c the analytical Gaussian function in the time domain is plotted. In Figure d the DFT from Figure c with the scaling factor is shown. In the figure it can be seen that figure a and figure c are equal and also figure b and d are the same. The analytical functions are the same as the functions obtained by Fourier transformations in MATLAB. Therefore the scaling factors obtained earlier are verified here.

3.3.3 Conclusion

In this section is shown that MATLAB can be used to perform Fourier transformations with. The only adjustment that has to be done is scaling of the amplitude. The scaling factors are obtained by analysis and numerically verified by means of simulations in MATLAB and are correct.

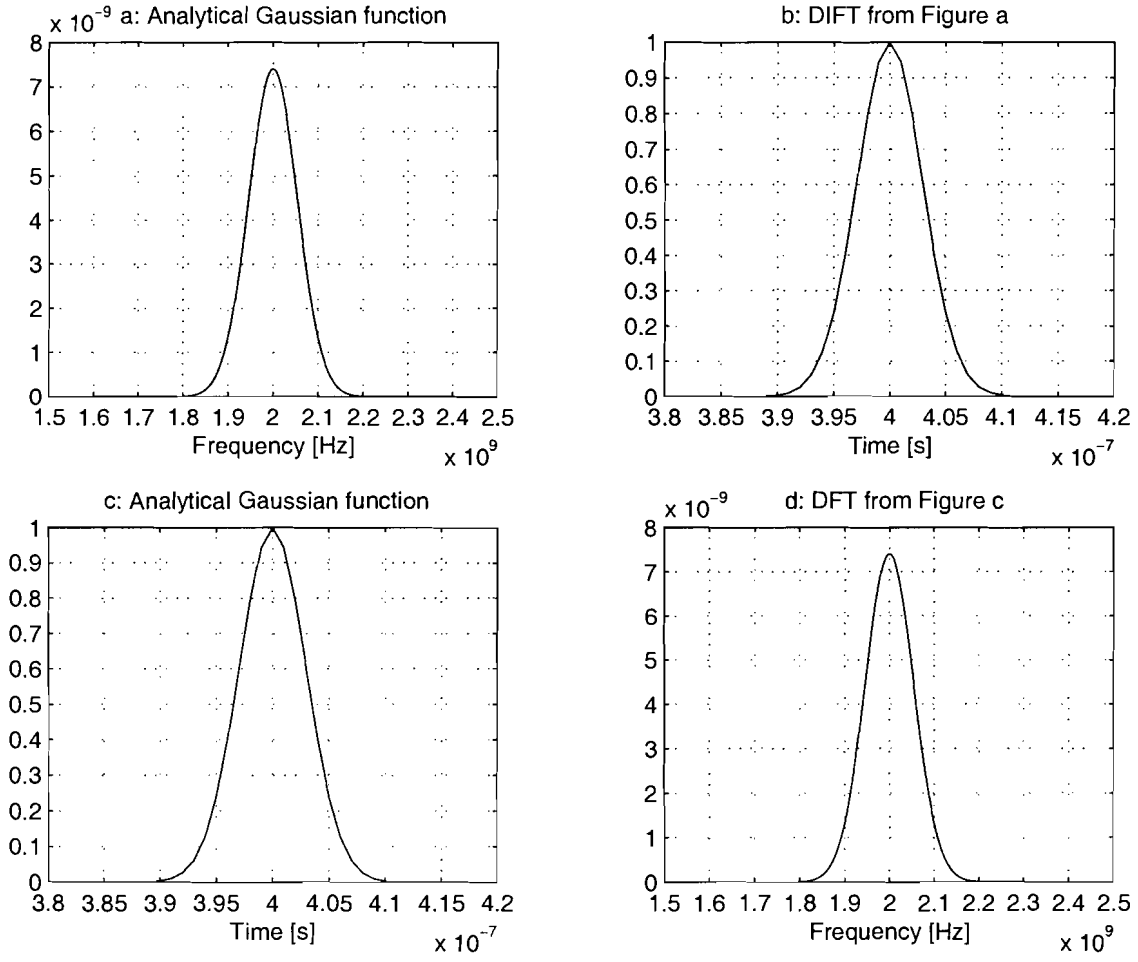

Figure 3.2: **Verification of the scaling factors for DFT and DIFT in MATLAB.**

3.4 Aliasing

The data in the frequency domain are measured at discrete frequencies with fixed frequency steps. This so called sampling in the frequency domain results in a repetition of the impulse response in the time domain [7]. The repetition time is $1/\Delta f$. Aliasing occurs if the signal is not small enough near the edges of the repetition time interval. The signal from the next and the previous interval are added to the original signal, and as a consequence the signal is distorted.

In Figure 3.3a a Gaussian function is plotted in the frequency domain. The frequency step Δf is 10 MHz. This results in a repetition time in the time domain of $1/\Delta f = 1 \times 10^{-7}$ s. An example of three repetition periods is shown in Figure 3.3b. In the figure it can be seen that the signal is small near the edges of the repetition interval and therefore the effect of aliasing is negligible. The inverse Fourier transform of Figure 3.3a is plotted in Figure 3.3c.

In Figure 3.4a a Gaussian function is plotted in the frequency domain. The frequency step (Δf) is 100 MHz. This results in a repetition time in the time domain of: $1/\Delta f = 1 \times 10^{-8}$ s. An example of three repetition periods is shown in Figure 3.4b. These curves are derived analytically in order to explain figure c. In the figure it can be seen that the signals overlap. Aliasing occurs and the inverse Fourier transform of Figure 3.4a is the summation of the signals in Figure 3.4b and is shown in Figure 3.4c.

A window can be used to suppress the power at the edges of the interval and reduces the effect of aliasing. The use of windows is described in the next section.

Another way of reducing the effect of aliasing is increasing the repetition time and thus decreasing the signal near the edges of the interval. This can be done by decreasing the frequency step. However, this results in a longer measurement time and larger data files which reduces the speed of the measurement and the simulations.

In this report the frequency step of the measurement is 250 kHz resulting in a repetition time of 4 μs. At 4 μs the amplitude of the impulse response is small enough [3] to neglect the effect of aliasing.

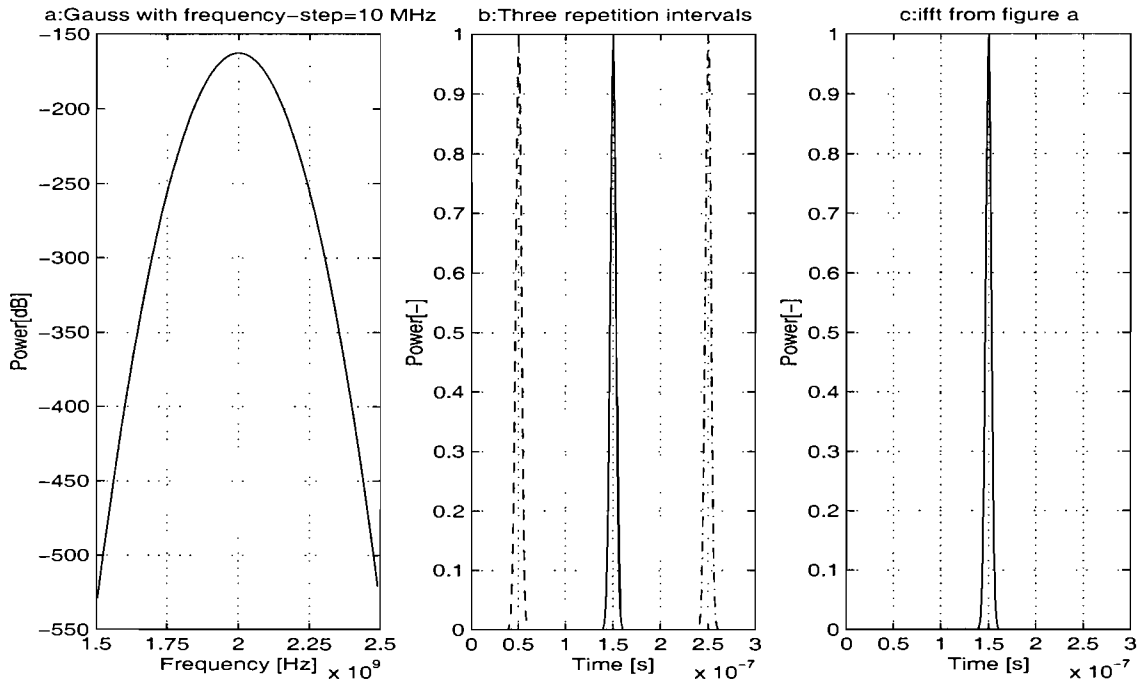

Figure 3.3: **Fourier transform when aliasing is negligible.**

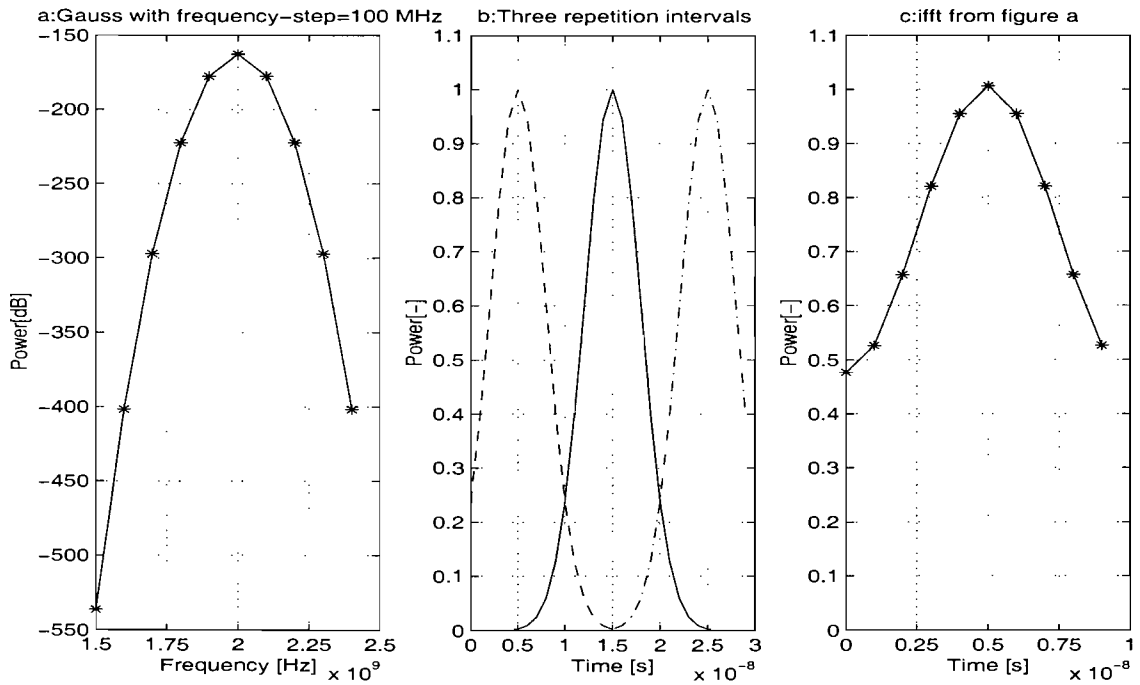

Figure 3.4: **Fourier transform when aliasing occurs.**

3.5 Windowing

In this section the necessity of windowing is explained and different windows are compared with each other.

The bandwidth we measure with the network analyzer is finite. The Fourier transformation performed on these data assumes an infinite spectrum. We can obtain an infinite spectrum by multiplying the measured data with a rectangular window of infinite length. This so called multiplying in the frequency domain results in a convolution in the time domain. As a result side lobes occur in the time domain. The height of the side lobe level is determined by the selected windows [24].

A rectangular window has a highest side lobe level of -13 dB (Figure 3.5). Better windows, which have lower side lobes and a lower suppression of the values at the edges of the interval, are available. However, the suppression of the values near the edges results in a loss of the information at the edges, this is called processing loss. There is a trade-off between processing loss and highest side lobe level.

One type of window is the Gaussian window. The parameter α defines the highest side lobe level and the processing loss of a Gaussian window. The smaller the processing loss, the higher the side lobe level (Table 3.4). The performance of a Gaussian window with an α of 2.5 is comparable with a Hamming window (Table 3.4). Simulations were performed with

Table 3.4: **Window parameters.**

Window Type		**Highest Side lobe level [dB]**	**Worst Case Process Loss [dB]**	**Figure**
Rectangular		-13	3.92	3.5
Triangle		-27	3.07	-
Gaussian	$\alpha = 2.5$	-42	3.14	3.6
	$\alpha = 3.0$	-55	3.40	3.7
	$\alpha = 3.5$	-69	3.73	3.8
	$\alpha = 3.71$	-77	> 3.73	3.9
Hamming		-43	3.10	-

MATLAB to verify these parameters [24]. The number of points to define the windows (N)is 50. On both sides of the windows enough zeros (approximately 1000) were added to make sure the Fourier Transforms are performed well. Without the zeros MATLAB the window is repeated after 50 points and aliasing can occur. The zeros are shown only in Figure 3.5.

Relation between a and α

In [24] the Gaussian window is defined as

$$w(n) = e^{-\frac{1}{2}\left(\alpha \frac{n}{N/2}\right)^2} \quad , \tag{3.21}$$

where $N = 50$, α defines the pulse width and $n = 1, 2, 3, ...N$ is a particular point. The

formula we use for the Gaussian window is (3.19)

$$V(\omega) = -\frac{j\sqrt{\pi}}{2a}\left(e^{-\left(\frac{\omega-\omega_0}{2a}\right)^2}\right)\cdot e^{-j\omega\tau} \quad . \tag{3.22}$$

Except from the amplitude and the delay time, (3.21) and (3.22) are equal if

$$-\frac{1}{2}\left(\alpha\frac{n}{N/2}\right)^2 = -\left(\frac{\omega-\omega_0}{2a}\right)^2 \quad , \tag{3.23}$$

or

$$a = \frac{BW[rad\cdot s^{-1}]}{2\sqrt{2}\cdot\alpha} \quad . \tag{3.24}$$

The relation between a and α for various values of α is shown in Table 3.5. In figures

Table 3.5: **Relation between a and α.**

α	**a**
2.50	3.55×10^8
3.00	2.96×10^8
3.50	2.54×10^8
3.71	2.40×10^8

3.5-3.9 different windows and their Fourier transform are plotted. From these figures the highest side lobe levels can be determined. These levels correspond to the values in Table 3.4.

In the past [3] the Gaussian window with an α of 3.71 (Figure 3.9) was used. The side lobes are much smaller than the side-lobes of the a the Gaussian function with an α of 2.5. However the processing loss is much larger. If we use a Gaussian window with an α of 2.5 the side lobes are small enough (-43 dB) compared to the signal to noise ratio of the measurement. The process loss is also smaller thus a better resolution is obtained. This Gaussian window is comparable with a Hamming window (Table 3.4).

Conclusions:
We will use Gaussian windows, for several reasons:

- The mathematical formula is analytically manipulable, and can easily be implemented in a computer program.
- The parameter 'a' or α can easily be adjusted for the trade-off between processing loss and highest side lobe level.

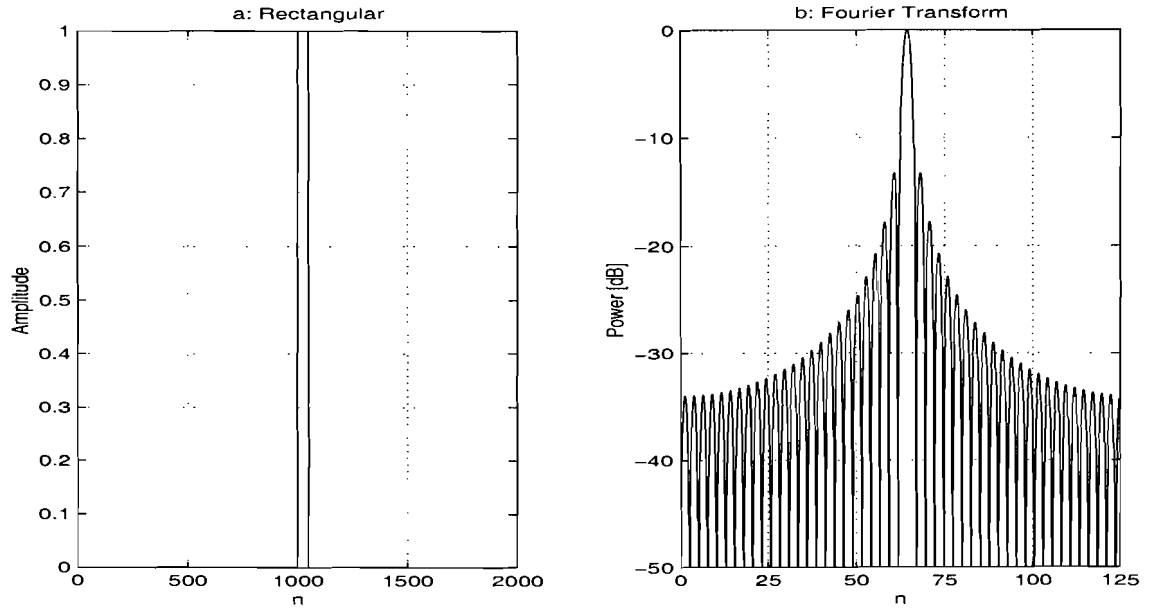

Figure 3.5: **Fourier Transform of a Rectangular Window.**

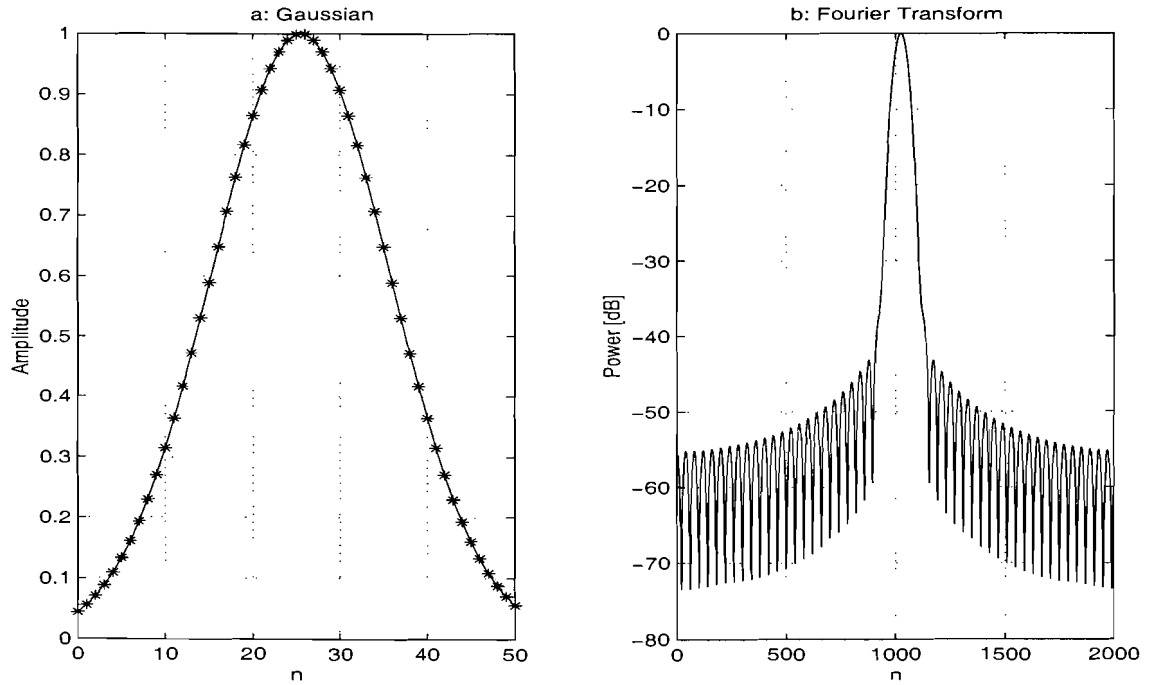

Figure 3.6: **Fourier Transform Gaussian Window with $\alpha = 2.5$.**

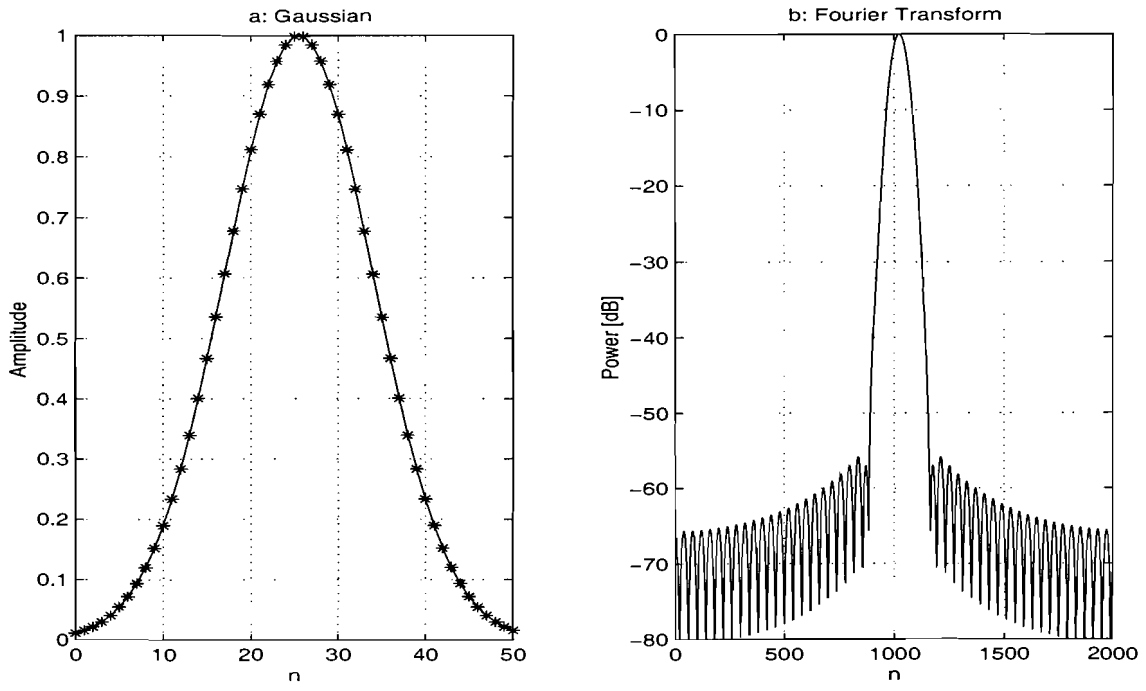

Figure 3.7: **Fourier Transform Gaussian Window with $\alpha = 3$.**

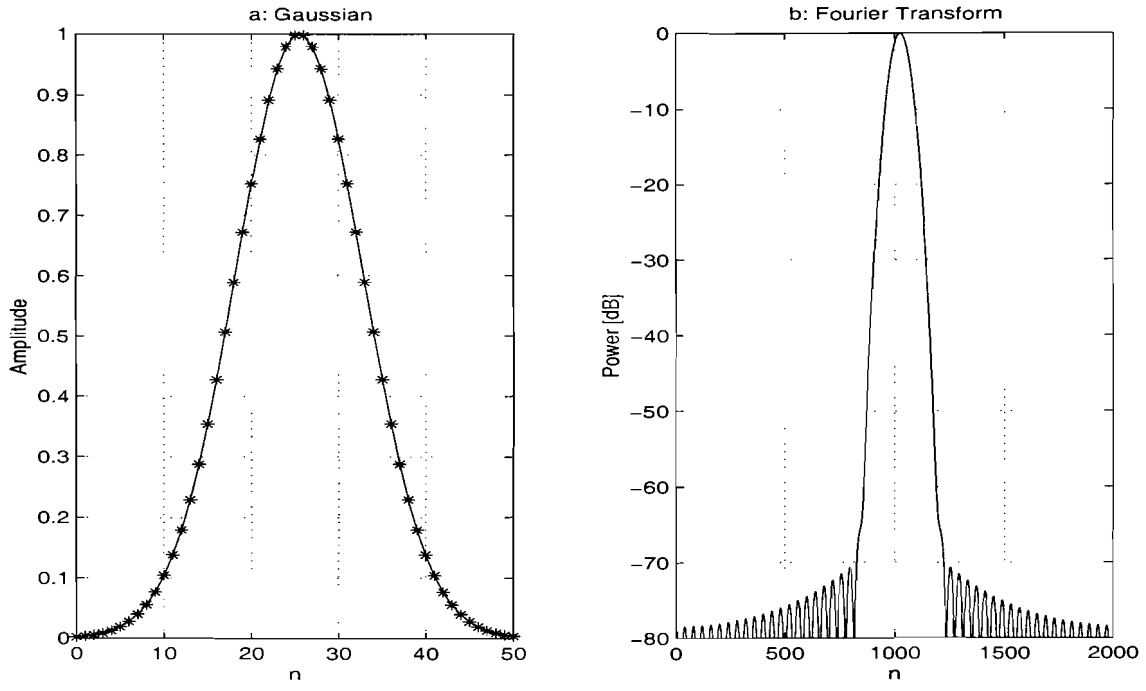

Figure 3.8: **Fourier Transform Gaussian Window with $\alpha = 3.5$.**

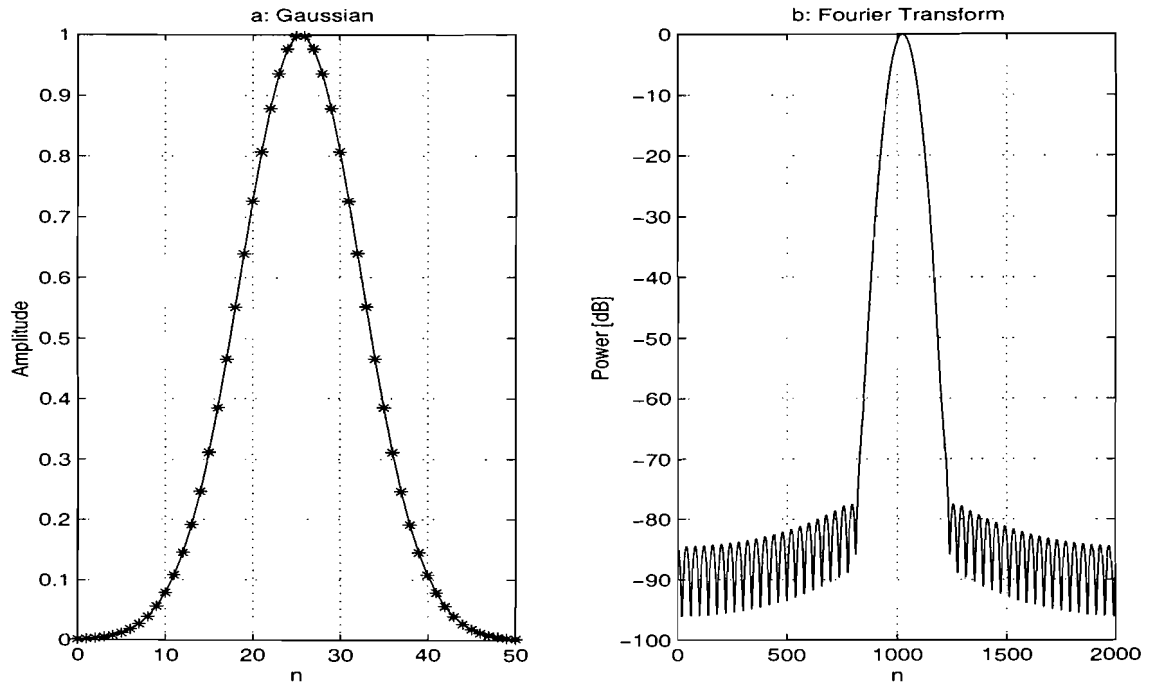

Figure 3.9: **Fourier Transform Gaussian Window with $\alpha = 3.71$ (=BW60dB).**

Example of impulse responses with different windows

In the past [1, 3] a Gaussian window with a 60 dB suppression of the edges was used. Or in other words a Gaussian window with $\alpha = 3.71$. This results in a highest side lobe level of -77 dB (see Table 3.4). However, this suppression is too stringent and a highest side lobe level of -42 dB or an α of 2.5 is a better choice. Using this window results in a smaller process loss and a better resolution. The resolution is determined by the reciprocal of the bandwidth. Sharper filters decrease the bandwidth and this results in a worser resolution. In Figures 3.10 and 3.11 impulse responses of the radio channel around 2.2 GHz are plotted. In Figure 3.10 a Gaussian window with $\alpha = 3.71$ is used while in Figure 3.11 a Gaussian window with $\alpha = 2.5$ is used. It is obvious that Figure 3.11 has a better resolution. The Gaussian window with $\alpha = 2.5$ will be used in this report.

3.6 Conclusions

We now know the impulse responses at each (measured) position in the xy-plane. These impulse response can be used to model the indoor radio channel or to determine typical radio channel parameters like rms delay spread.

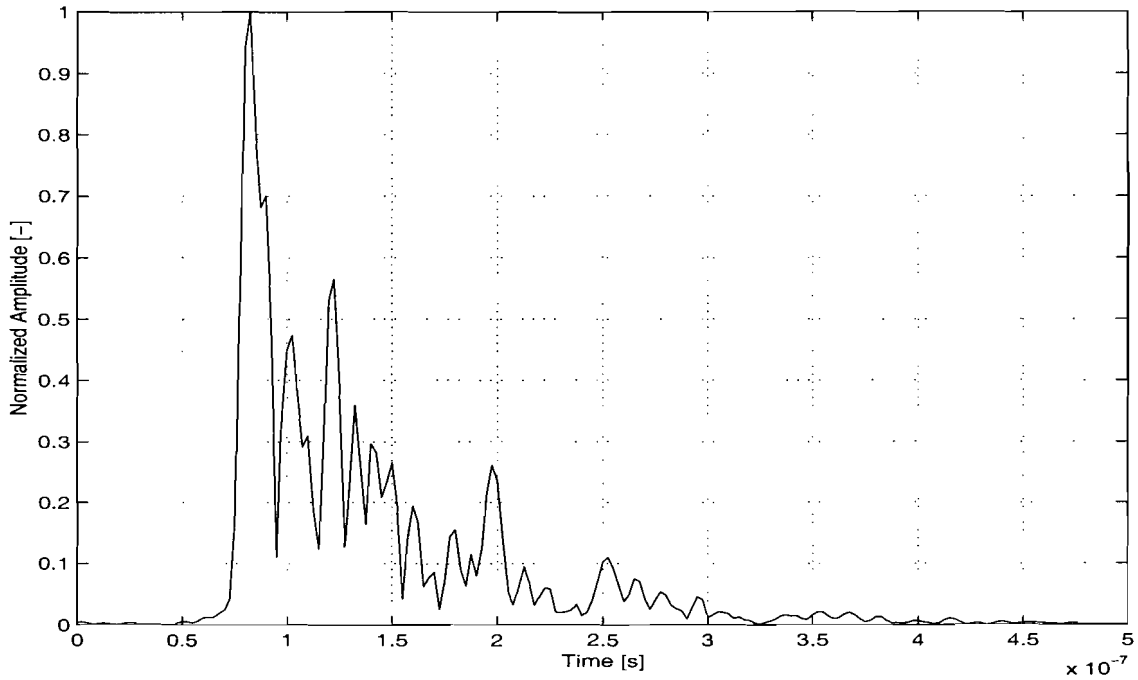

Figure 3.10: **Normalised Impulse Response with a Gaussian Window with α = 3.71.**

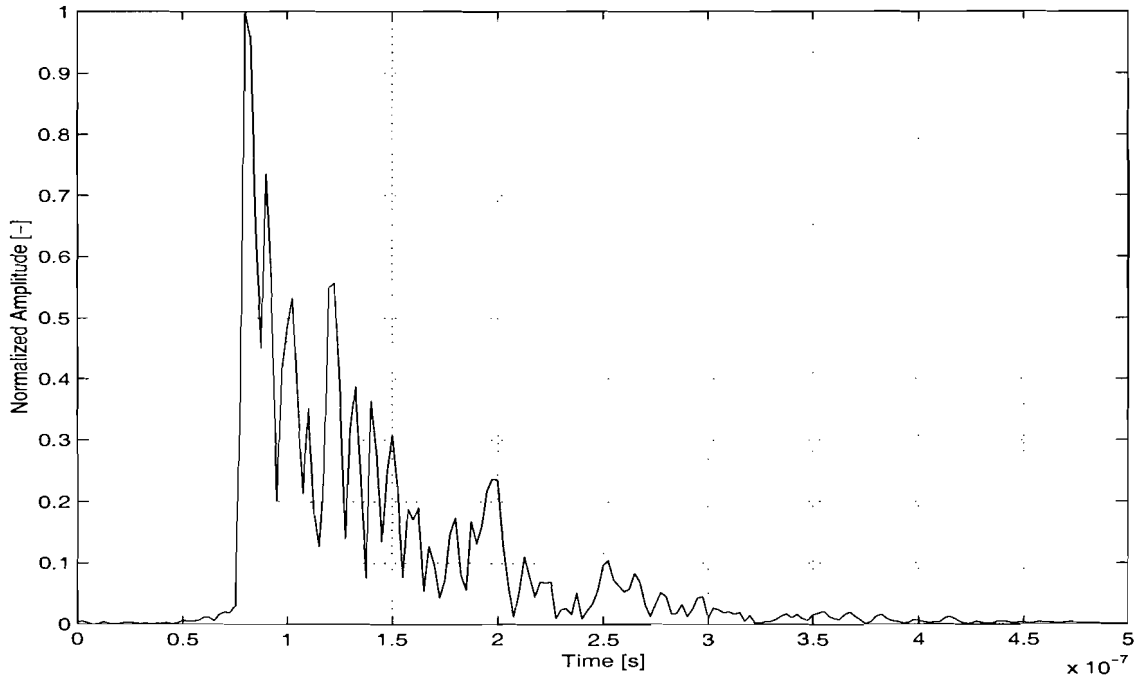

Figure 3.11: **Normalised Impulse Response with a Gaussian Window with α = 2.5.**

Chapter 4

Channel Modelling

4.1 Introduction

In this chapter the theory which is necessary for the channel modelling is described. First the theory of the radio channel is described (Section 4.2). The impulse response of the radio channel can be implemented in a tapped delay line (TDL) as is described in section 4.3. The coefficients of the TDL can have fixed values or stochastic values. The Rayleigh and Rician distribution are examples of stochastic distributions often used to describe the indoor radio channel and are presented in section 4.4. The way the coefficients are updated depends on the Doppler spread (Section 4.5). In section 4.6 is described how the coefficients are updated in this report. The chapter ends with some time dispersion parameters (Section 4.7).

4.2 The Radio Channel

The indoor radio channel can be modelled as a linear time-varying filter at each point in space. The impulse response can be written as [19]

$$h(t,\tau) = \sum_{k=0}^{N(\tau)-1} a_k(t) \cdot \delta\{\tau - \tau_k(t)\} \cdot e^{j\theta_k(t)} \quad . \tag{4.1}$$

with:

τ	= observation time
t	= application time
$N(\tau)$	= number of multipath components
$a_k(t)$	= random time-varying amplitude sequence
$\tau_k(t)$	= random time-varying arrival-time sequence
$\theta_k(t)$	= random time-varying phase sequence
δ	= delta function

The channel is completely characterised by these parameters. The mathematical description of the signal is shown in Figure 4.1.

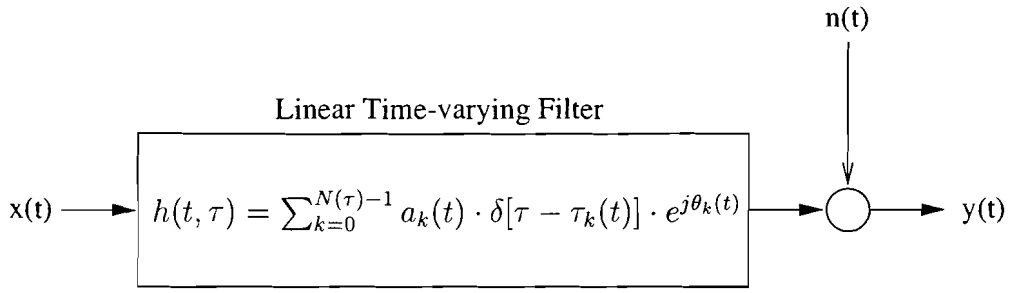

$$y(t) = \int_{-\infty}^{+\infty} x(\tau) \cdot h(t,\tau) \cdot d\tau + n(t)$$

Figure 4.1: **Mathematical model of the signal**

The output *y(t)* can be calculated by convolution of the input signal *x(t)* with the impulse response in (4.1). In most applications the impulse response can be considered as constant during several bit periods. In that case the impulse response from (4.1) becomes

$$h(t) = \sum_{k=0}^{N-1} a_k \cdot \delta\{t - t_k\} \cdot e^{j\theta_k} \quad . \tag{4.2}$$

The output *y(t)* of the radio channel due to a transmitted signal *s(t)* becomes

$$y(t) = \int_{-\infty}^{+\infty} s(\tau) \cdot h(t-\tau) \cdot d\tau + n(t) \quad , \tag{4.3}$$

where *n(t)* is the base-band complex-valued additive Gaussian noise.

If the input signal

$$x(t) = \Re\{s(t) \cdot e^{j\omega_0 t}\} \tag{4.4}$$

is transmitted through the channel the output *y(t)* becomes:

$$y(t) = \Re\{\rho(t) \cdot e^{j\omega_0 t}\} \quad , \tag{4.5}$$

where

$$\rho(t) = \sum_{k=0}^{N-1} a_k \cdot s(t - t_k) \cdot e^{j\theta_k} + n(t) \quad . \tag{4.6}$$

4.3 Tapped Delay Line (TDL)

The impulse response derived in the previous section can be implemented as a tapped delay line (Figure 4.2). The number of taps determines the resolution of the model. The more taps the more accurate the model is. However, increasing the number of taps decreases the speed of the simulations and a compromise has to be found. The values of the weighting coefficients (W_n) can be complex and represent a phase and an amplitude. It is also possible to update the coefficients after a certain time, which makes it possible to model a time varying impulse response (see (4.1)). A more detailed description of the TDL is presented later on in this report when the TDL is actually used in the model (Section 6.5). In Figure 4.2 an example of a tapped delay line is shown.

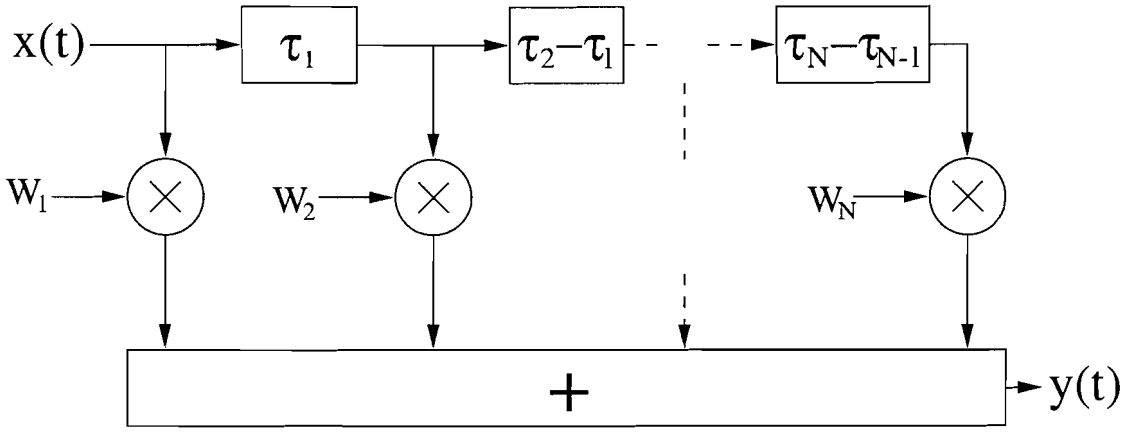

Figure 4.2: **Tapped Delay Line**

4.4 Distributions

Well-known distributions of the magnitude of a narrowband received signal for the indoor radio channel are the Rayleigh distribution for the non-line-of-sight (NLOS) and Rician distribution for the line-of-sight (LOS) distribution (see Figure 4.3).

4.4.1 Rayleigh distribution

The probability density function (PDF) of the Rayleigh distribution can be written as

$$Pr_{(a_k=r)} = \begin{cases} \frac{r}{\sigma^2} \cdot e^{-\frac{r^2}{2\sigma^2}} & (0 \leq r \leq \infty) \\ 0 & (r < 0) \end{cases} \tag{4.7}$$

where σ is the rms value of the magnitude (the most probable value).

In the Rayleigh distribution the in-phase (I) and quadrature (Q) components are independent. The Gaussian distributed random variables result in a joint distribution of the magnitude (x) of

$$x = \sqrt{I^2 + Q^2} \quad . \tag{4.8}$$

The cumulative distribution function (CDF) of the Rayleigh distribution is

$$P(r \leq R) = 1 - e^{-\frac{R^2}{2\sigma^2}} \quad . \tag{4.9}$$

4.4.2 Rician distribution

If a dominant pulse (LOS) is present the Rician distribution is a better distribution than the Rayleigh distribution. The Rician probability function consists of a deterministic part, e.a. the dominant pulse, and a Rayleigh distributed part which results in the following distribution

$$Pr_{(a_k=r)} = \begin{cases} \frac{r}{\sigma^2} \cdot e^{-\frac{r^2+A^2}{2\sigma^2}} \cdot I_0\left(\frac{Ar}{\sigma^2}\right) & (A \geq 0, r \geq 0) \\ 0 & (r < 0) \end{cases} \tag{4.10}$$

where

- I_0 is the zero-order modified Bessel-function of the first kind.
- The Rician factor K describes the ratio between the power of the dominant component and the power of the scattered components.
- A is the magnitude of the deterministic component.
- σ^2 is proportional to the power of the Rayleigh component.

The Rician factor K can be calculated with

$$K_{(dB)} = 10 \cdot \log\left(\frac{A^2}{2\sigma^2}\right) \quad . \tag{4.11}$$

Figure 4.3 shows the Rayleigh and Rician distribution functions. In the figure it can be seen that for $K >> 1$ the Rician distribution function is approximately Gaussian distributed about the mean.

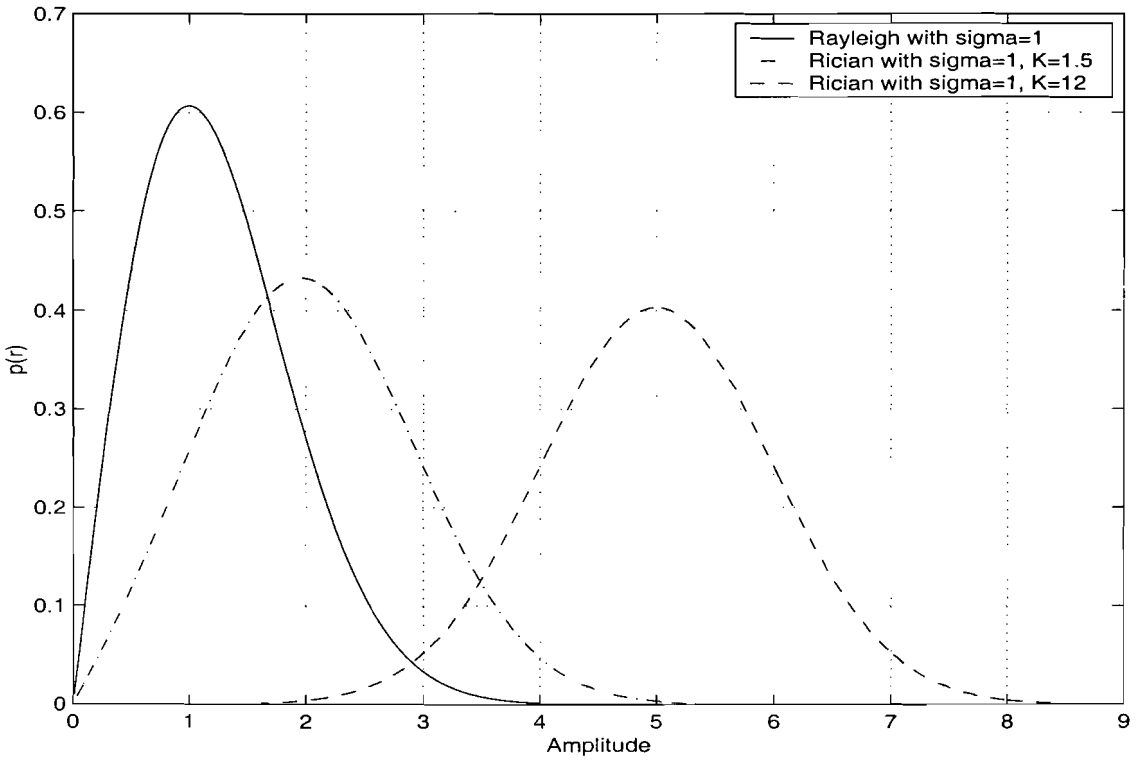

Figure 4.3: **Rayleigh and Rician probability density functions**

4.5 Doppler Spread

The Doppler spread is a measure of the spectral broadening caused by motion of the receiver and/or transmitter, or the motion of objects and/or people in the environment. The coherence time T_c is the time domain dual of the Doppler spread and is used to characterise the time varying nature of the frequency dispersion of the channel in the time domain [6]. The Doppler spread and the coherence time are inversely proportional to one another. A popular rule of thumb for modern digital communications posed by [6] is

$$T_C = \sqrt{\frac{9}{16 \cdot \pi \cdot f_m^2}} = \frac{0.423}{f_m} \quad , \tag{4.12}$$

where f_m is the maximum Doppler shift. The maximum Doppler shift is given by

$$f_m = \frac{v}{\lambda} \cdot \cos(\theta) = \frac{f_c \cdot v}{c} \cdot \cos(\theta) \quad , \tag{4.13}$$

where λ is the wavelength of the carrier frequency f_c, c is the velocity of light, v is the velocity of the portable station, and θ is the angle between the direction of the motion of the portable station and the direction of the arrival of the wave at the base station.

The maximum Doppler shift in a typical indoor environment for a carrier frequency of $f_c = 2.2$ GHz and a moving object having a velocity of 5 km/h (1.4 m/s) is 10.3 Hz. This results in a coherence time greater than 41.2 ms. As long as the symbol rate is greater than $1/T_C$=24 bps, the channel will not cause distortion due to motion. Mobile systems about 2 GHz for example DECT have symbol rates in the order of 1 Mbps which is much larger than 24 bps.

Conclusion
Systems like DECT are not distorted due to Doppler spread. They are distorted due to frequency selective fading. The rate of change of the frequency selective fading is determined by the Doppler spread.

4.6 Determination of the weighting coefficients of the TDL as a function of time

As a result of multipath, different rays arrive at the same time at the receiver and are added. The rays have different phases and amplitudes and may cause destructive and constructive interference. In literature [11, 22, 23] is shown that a good approximation of the amplitude is the Rayleigh distribution while the phase is uniformly distributed within $[0, 2\pi]$.

The transmission loss in dB in the xy-plane at 2.2 GHz can be obtained from the measurement and is plotted in Figure 4.4a. An example of the transmission loss along a straight line in the xy-plane is plotted in Figure 4.4b. In Chapter 6 will be explained how the parameter σ from the Rayleigh distribution (Section 4.4) can be obtained from the measurements.

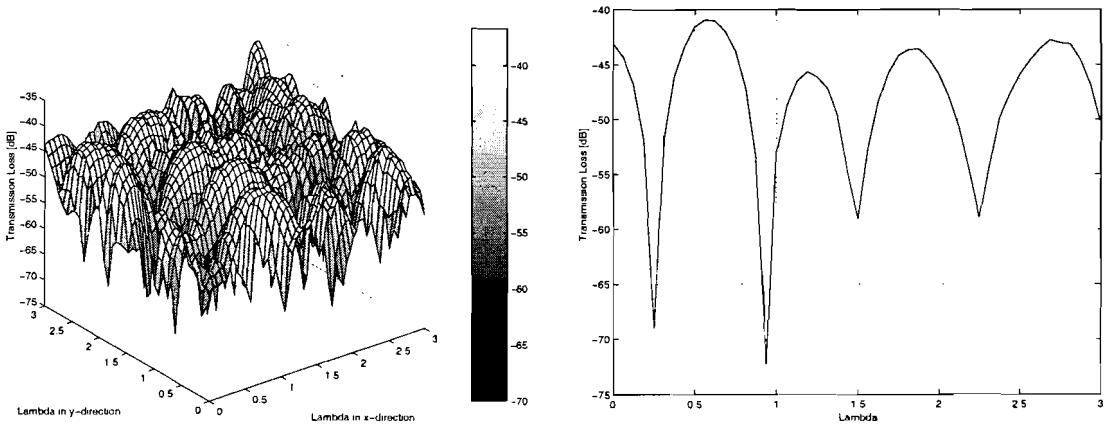

(a) Transmission Loss in xy-plane

(b) Transmission along one line

Figure 4.4: **Transmission Loss at 2.2 GHz.**

In section 4.7.2 of [6] is explained how a Rayleigh fading simulator can be built. With this Rayleigh fading simulator a typical Rayleigh fading channel at a particular receiver speed can be imitated. The Doppler frequency f_m presented in the previous section is used to implement the speed of the receiver in the fading simulator. Examples of typical envelopes of Rayleigh fading simulations at a speed v of 50 km/h (f_m = 100 Hz) and v=5 km/h (f_m = 10 Hz) at 2.2 GHz are shown in Figure 4.5 and Figure 4.6.

However if a fading simulator is used, simulations will take to much time. If for example the bit rate R_b = 2 Mbit/s, the symbol time $T_s = 1\mu s$ for QPSK modulation. In this case, simulations at a receiver speed of 5 km/h and a duration of 1 s, which corresponds with a distance of 1.4 m (Figure 4.6), would last 50 hours. In this simulation the BER is obtained for only one value of E_b/N_o and at one bit rate. These simulations will take too much time and therefore the fading simulator is not implemented in the model.

Instead of the fading generator, a random Rayleigh generator is used to simulate the amplitude. Every 100 symbols the generator generates a Rayleigh distributed amplitude

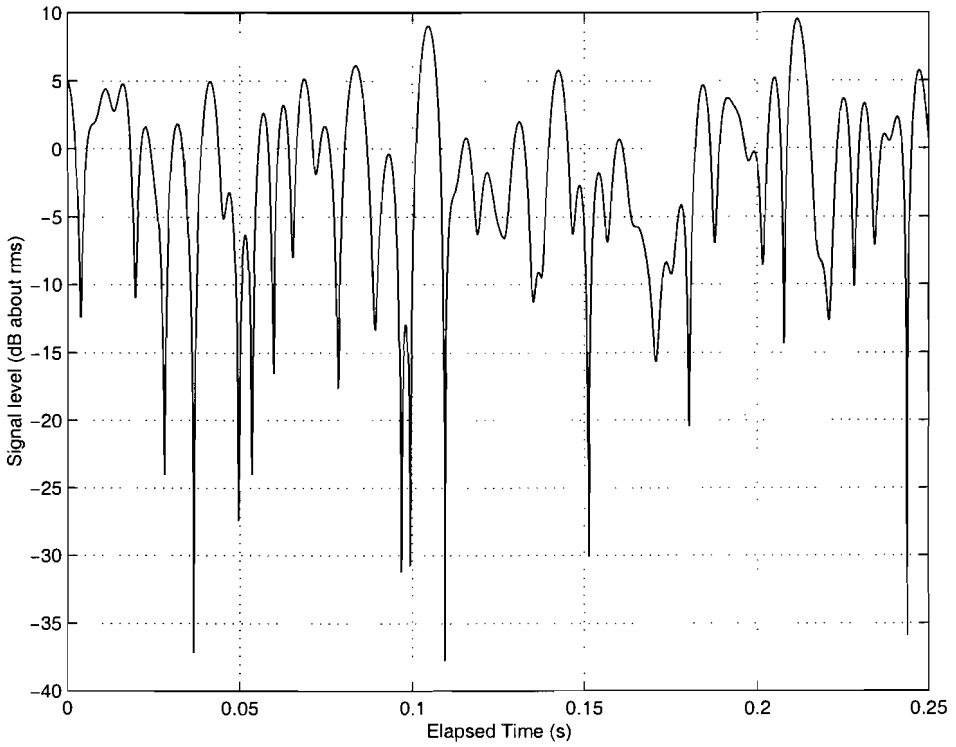

Figure 4.5: **Fading simulator with v=50 km/h, $f_c = 2.2$ GHz and $f_m = 100$ Hz.**

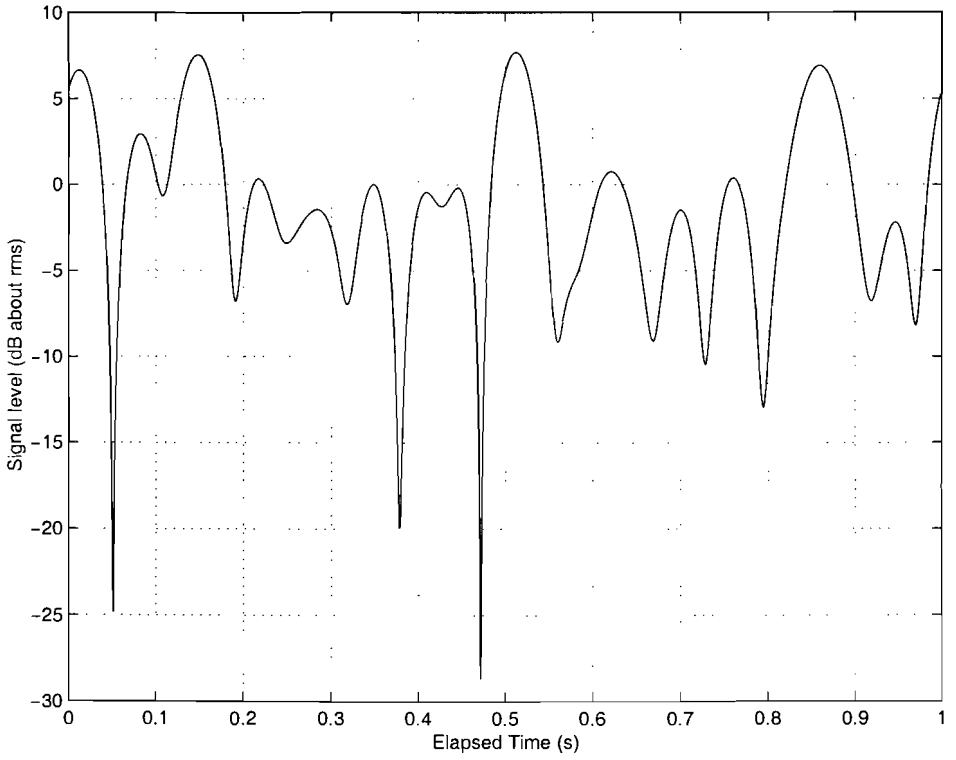

Figure 4.6: **Fading simulator with v=5 km/h, $f_c = 2.2$ GHz and $f_m = 10$ Hz.**

and the amplitudes within these 100 symbols are linearly interpolated as is shown in Figure 4.7.

The phase is simulated with a uniform generator which generates an uniformly distributed phase from $[0, 2\pi]$ every 100 symbols and the phases within these 100 symbols are linearly interpolated in the same way as the amplitude.

The amplitudes and phases are constant during one symbol.

Simulations performed with this technique are approximately 100 times as fast as the simulations with the Rayleigh fading simulator.

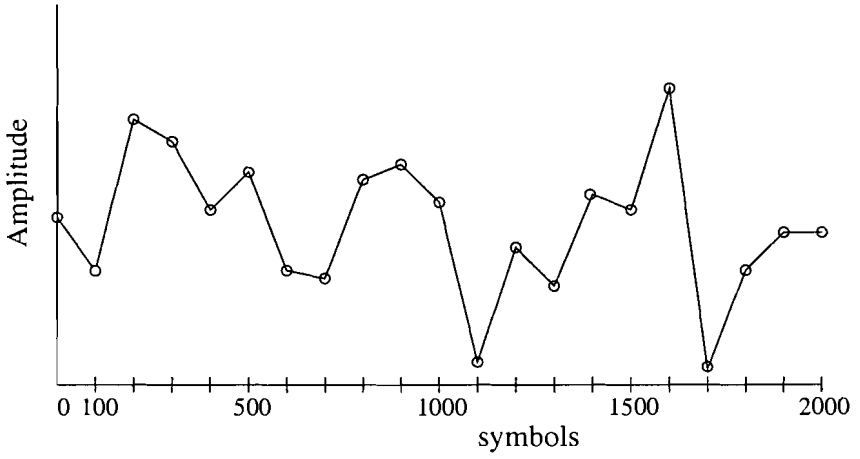

Figure 4.7: **Randomly chosen values from a Rayleigh distribution.**

4.7 Time Dispersion Parameters

In order to compare the time dispersion of different indoor radio channels various quantities can be used. The *mean excess delay, rms delay spread,* and *maximum excess delay* are multipath channel quantities that can be determined from the power delay profile. The *mean excess delay* is the first moment of the power delay profile and is defined to be

$$\overline{\tau} = \frac{\sum_k \alpha_k^2 \cdot \tau_k}{\sum_k \alpha_k^2} = \frac{\sum_k P(\tau_k) \cdot \tau_k}{\sum_k P(\tau_k)} \quad . \tag{4.14}$$

The *rms delay spread* is the square root of the second central moment of the power delay profile and is defined to be

$$\sigma_\tau = \sqrt{\overline{\tau^2} - (\overline{\tau})^2} \quad , \tag{4.15}$$

where

$$\overline{\tau^2} = \frac{\sum_k \alpha_k^2 \cdot \tau_k^2}{\sum_k \alpha_k^2} = \frac{\sum_k P(\tau_k) \cdot \tau_k^2}{\sum_k P(\tau_k)} \quad . \tag{4.16}$$

These delays are measured relative to the first detectable signal arriving at the receiver at $\tau_0 = 0$. These equations do not rely on the absolute power within $P(\tau)$, but only on the relative amplitudes of the multipath components within $P(\tau)$.

The *maximum excess delay* (X dB) of the power delay profile is defined to be the time delay during which multipath energy falls to X dB below the maximum.

The rms delay spread σ_τ is ab often used time dispersion parameter used to describe the (indoor) radio channel, because of its relation with the bit error rate.

4.8 Conclusions

In this chapter is shown that the impulse response of the indoor radio channel can be described as a linear time-varying filter and can be implemented in a tapped delay line.

From this chapter can also be concluded that systems like DECT, UMTS and Bluetooth are not distorted due to Doppler spread but they are distorted due to frequency selective fading. The rate of change of the frequency selective fading is determined by the Doppler spread.

The coefficients of the tapped delay line are Rayleigh distributed values.

Finally, it can be concluded that the Rayleigh fading simulator is a good simulation tool, but needs long simulation time. A Rayleigh random generator is used instead, which results in shorter simulations.

Chapter 5

Simulations with Radio Channel Models

5.1 Introduction

In this chapter the simulations performed with three different radio channel models are presented. The simulations performed with these three models are used to verify the correctness of the simulations by means of comparing the simulation results with the theoretical bit error rates.

The first radio channel model is the additive white Gaussian noise (AWGN) channel (section 5.2). This model is simulated with the following modulation techniques, binary phase shift keying (BPSK), quadrature phase shift keying (QPSK) and $\pi/4$ differential quadrature phase shift keying ($\pi/4$ DQPSK). In section 5.3 the flat fading channel is described. Finally the two-ray Rayleigh fading model is presented in section 5.4.

5.2 Additive White Gaussian Noise (AWGN) channel

In this section simulations performed with different linear modulation techniques in an additive white Gaussian noise (AWGN) channel are described. In a linear modulation scheme, the amplitude of the transmitted signal $s(t)$ varies linearly with the modulating signal $m(t)$. In a linear modulation scheme, the transmitted signal $s(t)$ can be expressed as [6]

$$s(t) = Re\left(A \cdot m(t) \cdot e^{j2\pi f_c \cdot t}\right) \tag{5.1}$$

$$= A \cdot [m_R(t) \cdot \cos(2\pi f_c \cdot t) - m_I(t) \cdot \sin(2\pi f_c \cdot t)] \quad , \tag{5.2}$$

where A is the amplitude, f_c is the carrier frequency and $m(t)$ is a complex envelope representation of the modulated signal,

$$m(t) = m_R(t) + j \cdot m_I(t) \quad . \tag{5.3}$$

The linear modulation techniques described in this section are binary phase shift keying (BPSK), quadrature phase shift keying (QPSK) and $\pi/4$ differential quadrature phase shift keying ($\pi/4$ DQPSK).

5.2.1 Binary Phase Shift Keying (BPSK)

In BPSK the information is contained in the phase of the carrier. The amplitude of the carrier is constant. A binary 1 corresponds to a phase of zero degrees while a binary 0 corresponds to a phase of 180 degrees. The binary values can be plotted in a so called constellation diagram as shown in Figure 5.1. In this figure E_b is the energy per bit, I is the in-phase and Q is the quadrature term of the signal. The two possible signals $s_1(t)$

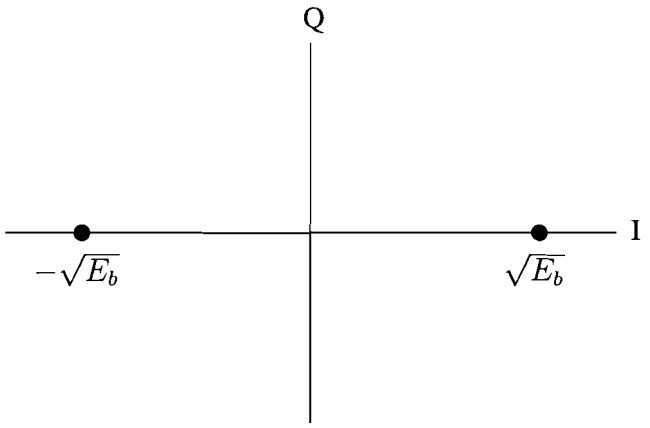

Figure 5.1: **BPSK constellation diagram.**

and $s_2(t)$ for the binary 1 and 0 respectively for BPSK modulation are

$$s_1(t) = \sqrt{\frac{2E_b}{T_b}}\cos(2\pi f_c t) \quad 0 \leq t \leq T_b \tag{5.4}$$

$$s_2(t) = -\sqrt{\frac{2E_b}{T_b}}\cos(2\pi f_c t) \quad 0 \leq t \leq T_b \tag{5.5}$$

where the energy per bit $E_b = \frac{1}{2}A_c^2 T_b$ and A_c is the amplitude of the carrier.

In an additive white Gaussian noise (AWGN) channel, the error probability depends on the distance between the points in the constellation diagram, $2\sqrt{E_b}$ in this case, and the noise spectral density N_0. The error probability in an AWGN channel for BPSK is derived in [6] as

$$P_{e,BPSK} = Q\left(\sqrt{\frac{2E_b}{N_0}}\right) \quad , \tag{5.6}$$

where $Q(x)$ is the Q-function (see Appendix B).

The error probability function from (5.6) is plotted in Figure 5.10 (dashed line).

5.2.2 Quadrature Phase Shift Keying (QPSK)

The principle of quadrature phase shift keying (QPSK) is the same as that of BPSK, with the only difference that the phase has 4 different values. Two possible constellation diagrams are shown in Figure 5.2. If the constellation diagram on the left-hand side of

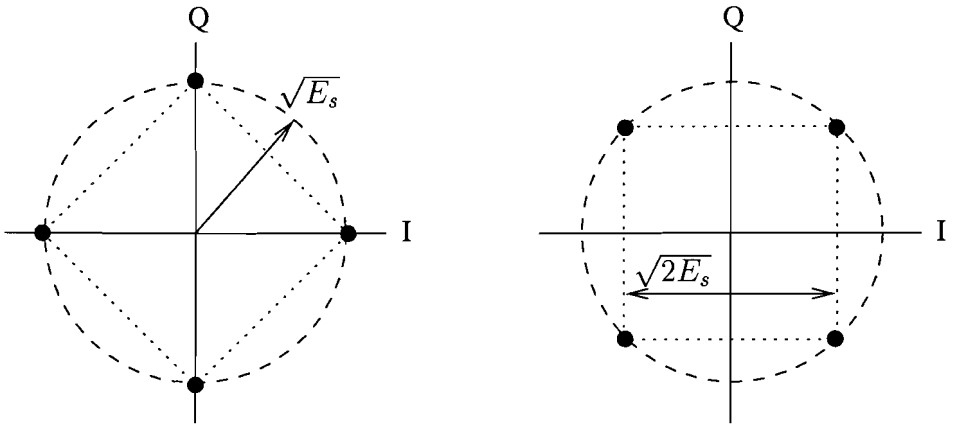

Figure 5.2: **QPSK constellation diagrams.**

Figure 5.2 is used, the four possible signals $s_1(t)$, $s_2(t)$, $s_3(t)$ and $s_4(t)$ for the bit-pairs 00, 01, 11 and 10 respectively for QPSK modulation can be written as

$$s_1(t) = \sqrt{\frac{2E_s}{T_s}}\cos(2\pi f_c t) \quad 0 \leq t \leq T_s \tag{5.7}$$

$$s_2(t) = \sqrt{\frac{2E_s}{T_s}}\sin(2\pi f_c t) \quad 0 \leq t \leq T_s \tag{5.8}$$

$$s_3(t) = -\sqrt{\frac{2E_s}{T_s}}\cos(2\pi f_c t) \quad 0 \leq t \leq T_s \tag{5.9}$$

$$s_4(t) = -\sqrt{\frac{2E_s}{T_s}}\sin(2\pi f_c t) \quad 0 \leq t \leq T_s \tag{5.10}$$

where the symbol time $T_s = 2T_b$ and E_s is the energy per symbol.

In the figure can be seen that the distance between adjacent points is $\sqrt{2E_s}$. Each symbol corresponds with two bits and therefore $E_s = 2E_b$, and thus the distance between adjacent symbols is $2E_b$. This is the same distance as for BPSK modulation and therefore the error probability for QPSK is the same as the error probability for BPSK (see Figure 5.10)

$$P_{e,QPSK} = Q\left(\sqrt{\frac{2E_b}{N_0}}\right) \quad . \tag{5.11}$$

However, twice as much data can be sent in the same bandwidth for QPSK modulation.

5.2.3 $\pi/4$ Differential Quadrature Phase Shift Keying ($\pi/4$ DQPSK)

$\pi/4$ differential quadrature phase shift keying ($\pi/4$ DQPSK) is a modulation technique where the symbols are chosen from the two constellation plots in Figure 5.2. The symbols are chosen alternately from the left and the right figure. All possible states and possible transitions are shown in Figure 5.3. The transitions or phase shifts ϕ_k are chosen according

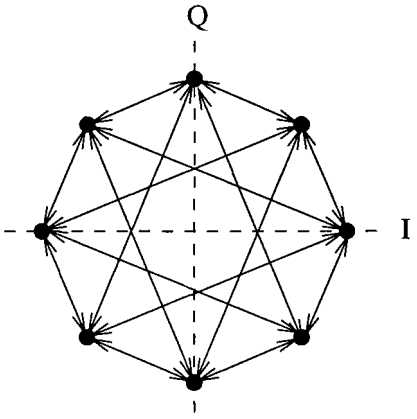

Figure 5.3: **All possible states and transitions in a $\pi/4$ QPSK constellation diagram.**

to the phase shifts in Table 5.1. The in-phase term I_k and the quadrature term Q_k can be determined with

$$I_k = \cos\theta_k \tag{5.12}$$

$$Q_k = \sin\theta_k \tag{5.13}$$

where

$$\theta_k = \theta_{k-1} + \phi_k \tag{5.14}$$

and θ_k is the phase of the k th symbol and θ_{k-1} is the phase of the $k-1$ st symbol (the previous symbol) and θ_0 is assumed to be 0.

Table 5.1: **Phase shifts corresponding with various input bit pairs.**

Input bits	Phase shift ϕ_k
11	$\frac{1}{4}\pi$
01	$\frac{3}{4}\pi$
00	$\frac{5}{4}\pi$
10	$\frac{7}{4}\pi$

The signal is demodulated using baseband differential detection. The demodulation is performed as is shown in Figure 5.4. The theoretical error probability function is given in

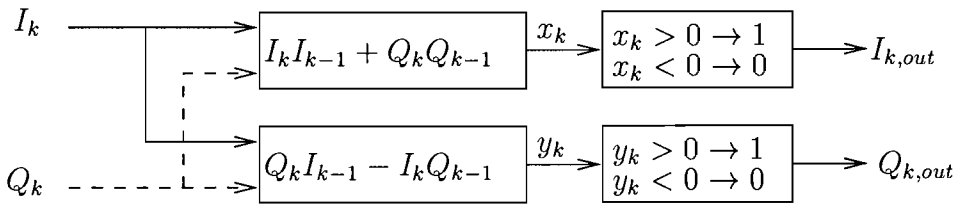

Figure 5.4: $\pi/4$ **DQPSK baseband demodulator.**

[28] as

$$P_b \approx Q\left(\sqrt{\frac{2E_b}{N_o} \cdot 4\sin^2\left(\frac{\pi}{8}\right)}\right) \quad , \tag{5.15}$$

and plotted in Figure 5.10 (solid line).

5.2.4 Simulations

BPSK

In Figure 5.5 the simulink model for BPSK modulation in a AWGN channel is shown. The *Random bit generator* block produces random zeros and ones with equal chance of occurrence. The pulse shape is rectangular and the bit time T_b can be adjusted. A seed can be chosen and the sequence is repeatable for a given seed.

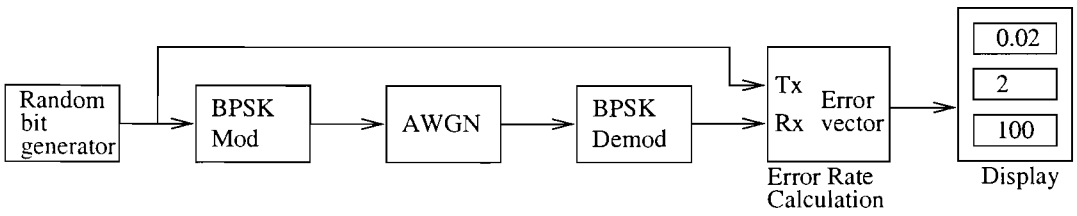

Figure 5.5: **Simulink model BPSK modulation.**

The *BPSK mod* block maps the input bits in the complex plane as is shown in table 5.2.

Table 5.2: **Mapping Gray-coded BPSK in the complex plane.**

Bit	Complex value
0	-1+0i
1	+1+0i

The modulated values are applied to an *AWGN* block which adds (complex) white Gaussian noise to the signal. The parameter E_b/N_o can be adjusted in the *AWGN* block. In [25] is shown that the optimum receive filter for BPSK demodulation takes the form of a matched filter when the noise is white. The matched filter (for rectangular pulses) can be implemented as an integrate and dump correlation receiver. The *BPSK Demod* block is a correlation receiver as shown in Figure 5.6, where $\Re$ denotes the real part. The *Error Rate Calculation* block compares the input bits with the output bits. The error vector is

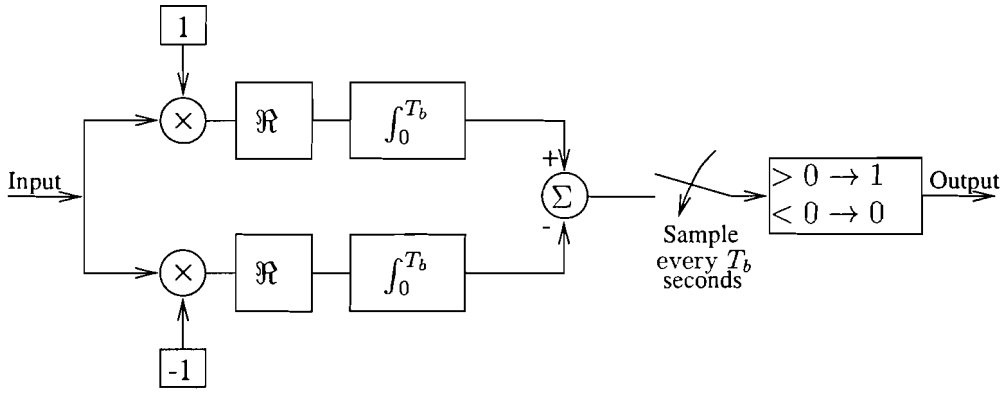

Figure 5.6: **Correlation Receiver.**

1 when an error occurs and a zero when the bits are equal. The number of bits sent, the number of errors as well as the error rate are shown on the *display* block.

The BER is simulated for different values of E_b/N_o (the ratio of energy per bit to noise spectral density). The number of errors is always much larger than 100 and the number of bits sent is always larger than 10000, in order to provide a reliable BER. The number of samples per bit is 100. The results of the simulations are shown in Figure 5.10. In the figure can be seen that the simulations match well with the theoretical results in section 5.2.1.

QPSK

In Figure 5.7 the simulink model for QSPK modulation in a AWGN channel is shown. The *Gray coded QPSK Mod* block maps the input bits in the complex plane as is shown in table 5.3. The *Gray coded QPSK Demod* block has the same principle as the correlation

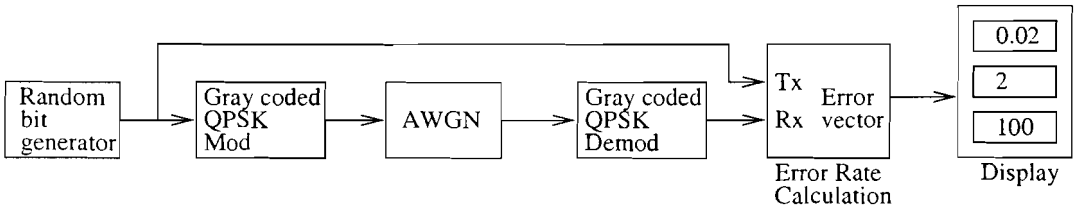

Figure 5.7: **Simulink model QPSK modulation.**

Table 5.3: **Mapping Gray coded QPSK in the complex plane.**

Bits	Complex value (for modulation)	Complex conjugated values (for demodulation)
00	1	1
01	i	-i
10	-i	i
11	-1	-1

receiver from Figure 5.6. The QPSK demodulator is shown in Figure 5.8. The input signal is multiplied by the complex conjugated values from Table 5.3. Multiplying the

complex value with its complex conjugated value gives 1. At the sample moment the decision circuit chooses the highest of the 4 inputs and sends the bits corresponding with this input to the output.

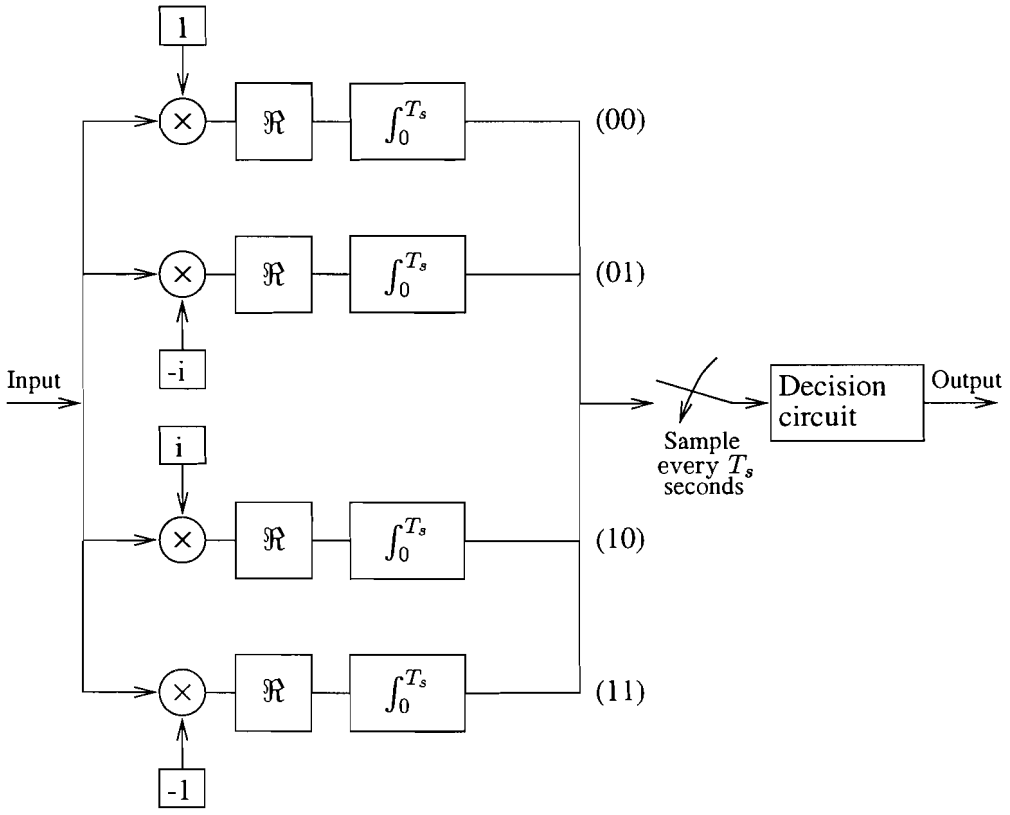

Figure 5.8: **QPSK demodulator.**

The results of the simulations are shown in Figure 5.10. In the figure can be seen that the simulations match well with the theoretical results in section 5.2.2.

$\pi/4$ DQPSK

In Figure 5.9 the simulink model used for simulations with $\pi/4$ DQPSK modulation in an AWGN channel is shown. The $\pi/4$ *DQPSK Mod* block maps the input bits in the complex plane as explained in section 5.2.3. The $\pi/4$ *DQPSK Demod* block operates as shown in Figure 5.4. Simulations were performed with $\pi/4$ DQPSK and the results of

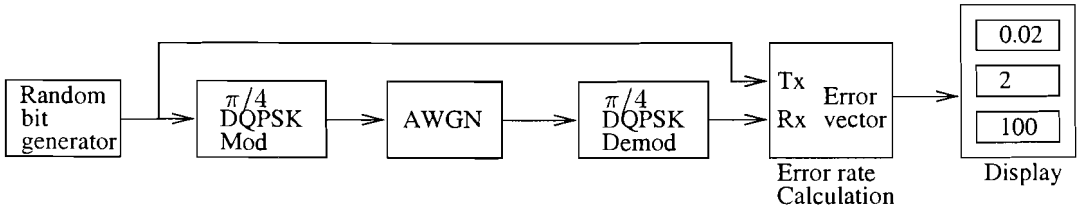

Figure 5.9: **Simulink model $\pi/4$ DQPSK modulation.**

the simulations as well as the theoretical curve from (5.15) are shown in Figure 5.10. In the figure it can be seen that the simulations match well with the theoretical results in section 5.2.3.

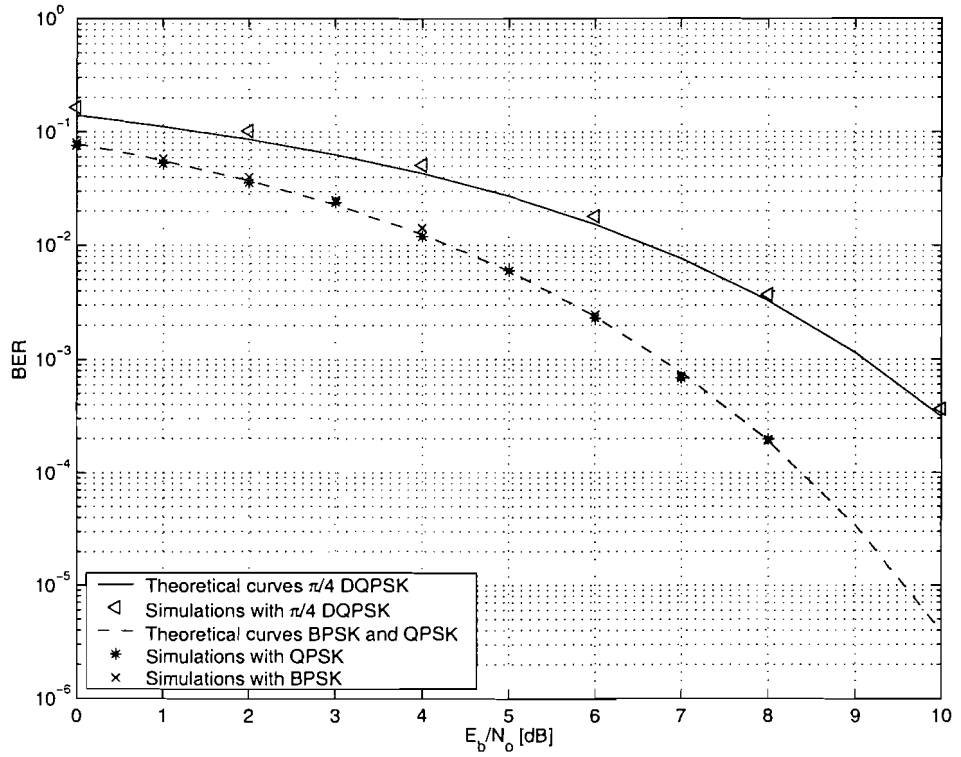

Figure 5.10: **BER versus E_b/N_o in an AWGN channel.**

5.3 Flat fading channel

If the coherence bandwidth of the channel is greater than the bandwidth of the transmitted signal the signal undergoes flat fading. In a flat fading channel the frequency characteristics are preserved but the strength of the received channel changes with time. This is due to the fluctuations in gain caused by multipath.

In a slow flat fading channel the gain $\alpha(t)$ can be considered constant during one symbol period. The received signal $r(t)$ can be described as

$$r(t) = \alpha(t)e^{-j\theta(t)}s(t) + n(t) \quad , \tag{5.16}$$

where $s(t)$ is the transmitted signal, $\theta(t)$ is the phase shift of the channel and $n(t)$ is the additive white Gaussian noise. For coherent detection the phase shift is known and the flat fading channel can be modelled as is shown in Figure 5.11. In this model a Rayleigh fading channel is assumed. The bit error rate for coherent binary phase shift keying in a Rayleigh slow flat fading channel is derived in [6] and is

$$P_{e,PSK} = \frac{1}{2}\left[1 - \sqrt{\frac{\Gamma}{\Gamma+1}}\right] \quad , \tag{5.17}$$

where $\Gamma = \frac{E_b}{N_o}\overline{\alpha^2}$ is the average value of the signal-to-noise ratio.

Simulations where performed with BPSK modulation and the slow Rayleigh fading channel. The simulations were performed with $\overline{\alpha^2} = 1$. This corresponds to Rayleigh distribu-

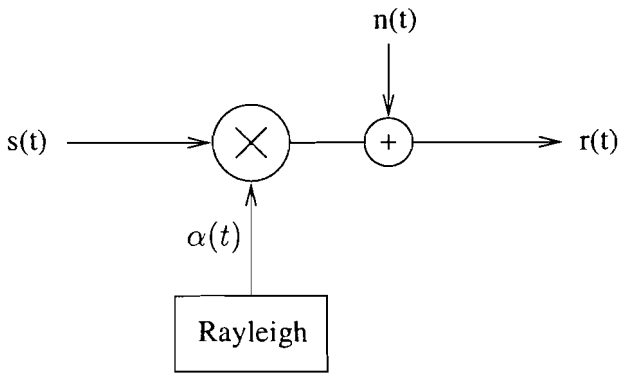

Figure 5.11: **Model of a Rayleigh flat fading channel.**

tions with $\sigma = \frac{1}{\sqrt{2}}$, because

$$E[r^2] = 2\sigma^2 \quad , \tag{5.18}$$

where r represents the Rayleigh distributed amplitude and $E[\bullet]$ is the expectation operator.

The model in Figure 5.12 is used for the simulations. The results of the simulation together

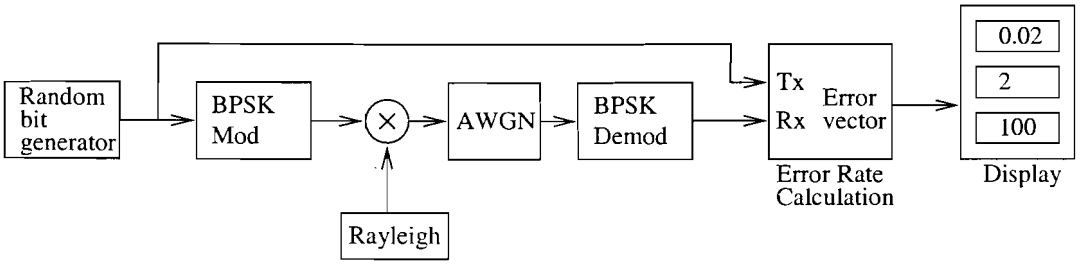

Figure 5.12: **Simulink model flat-fading channel with BPSK modulation.**

with the theoretical bit error rate from (5.17) are plotted in Figure 5.13. In this figure can be seen that the simulations match well with the theoretical curve. Also plotted in the figure is the theoretical bit error rate curve for BPSK modulation in an AWGN channel. Comparing the theoretical curve for the flat-fading channel with the theoretical curve for the AWGN channel shows the degradation of the performance caused by flat fading.

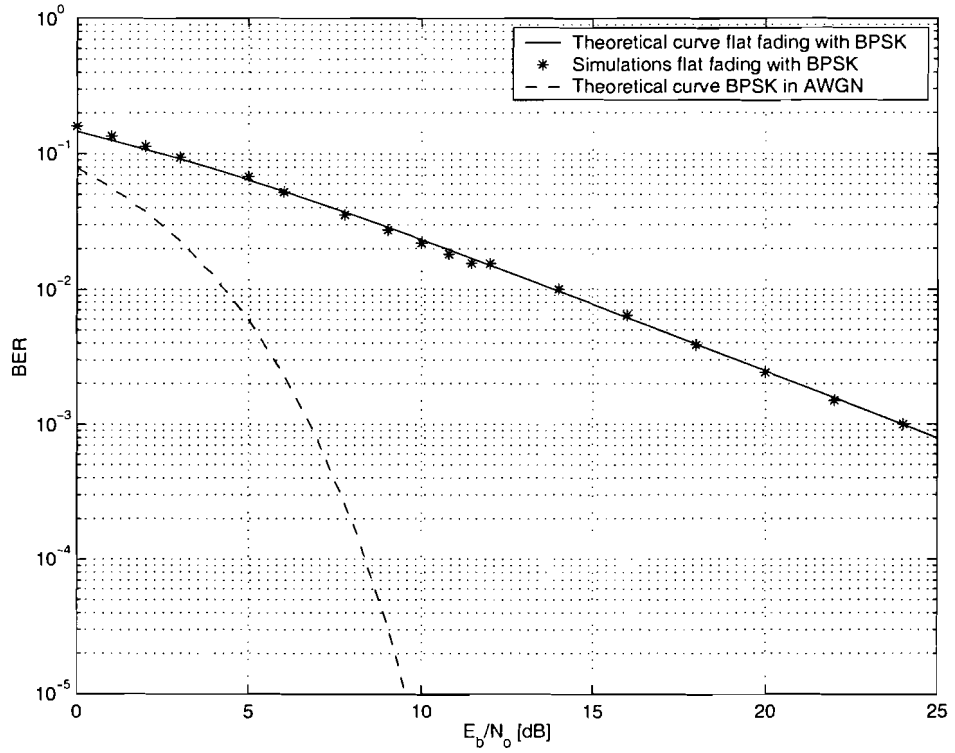

Figure 5.13: **BER versus E_b/N_o in a Rayleigh flat fading channel with BPSK.**

5.4 Two-ray Rayleigh fading model

Frequency selective fading occurs if the bandwidth of the transmitted signal is much larger than the coherence bandwidth of the radio channel. Different frequencies have different fading characteristics. The two-ray Rayleigh fading model is one of the methods to model frequency selective fading. The two-ray Rayleigh fading model consists of two delta pulses separated in time. The amplitudes vary corresponding to a Rayleigh distribution and the phases are uniformly distributed within $[0, 2\pi]$. Mathematically this can be formulated as [26]

$$h(kT) = \alpha_1 e^{j\theta_1(kT)}\delta(kT) + \alpha_2 e^{j\theta_2(kT)}\delta(kT - \tau) \quad , \tag{5.19}$$

where α_1 and α_2 are independent and Rayleigh distributed, θ_1 and θ_2 are independent and uniformly distributed over $[0, 2\pi]$, τ is the delay time between the pulses and T is the sample period which is 1/100 of the symbol time in this report. A scheme of the two-ray model is shown in Figure 5.14.

In the simulations the main ray and the delayed ray have the same power

$$E\left[\alpha_1^2\right] = E\left[\alpha_2^2\right] \quad , \tag{5.20}$$

where $E[\bullet]$ is the expectation operator. Since the sample period is 1/100 of the symbol time, the delay time τ is

$$\tau = 0.01 \cdot k \cdot T_s \quad , \tag{5.21}$$

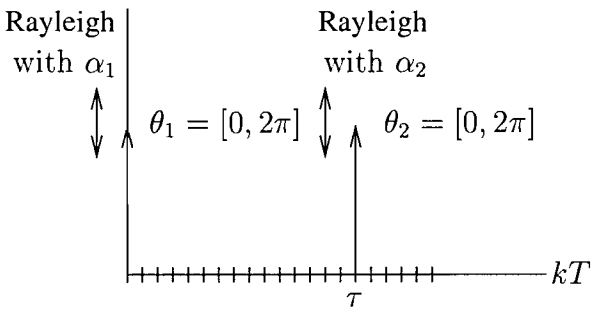

Figure 5.14: **Scheme of the two-ray Rayleigh fading model.**

where T_s is the symbol time and k is an integer.

The amplitudes and phases of both rays are independent, fixed during one symbol period, updated every 100 symbols and interpolated in between as was explained in Section 4.6.

The simulations were performed with $\pi/4$ DQPSK modulation for various values of τ/T_s. The results of these simulations are shown in Figure 5.17. These results match very well with the results obtained in [26].

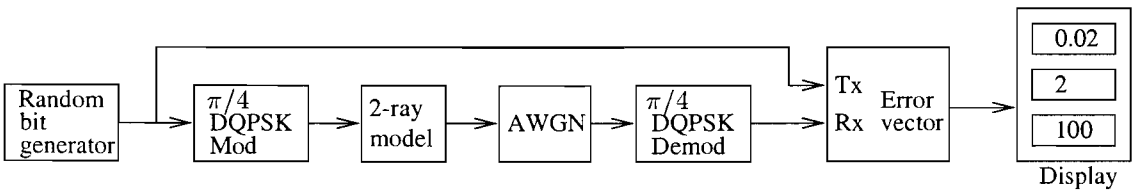

Figure 5.15: **Simulink model two-ray Rayleigh fading model.**

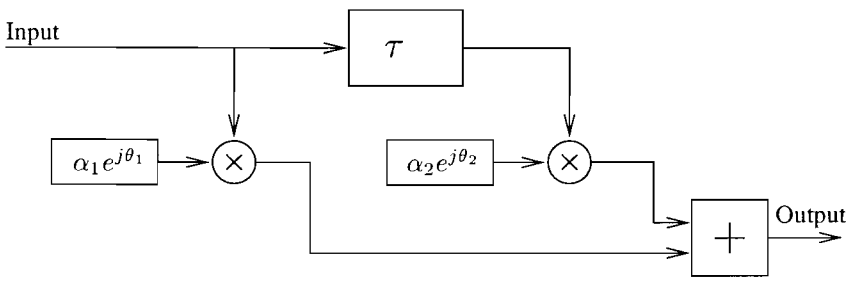

Figure 5.16: **Two-ray model.**

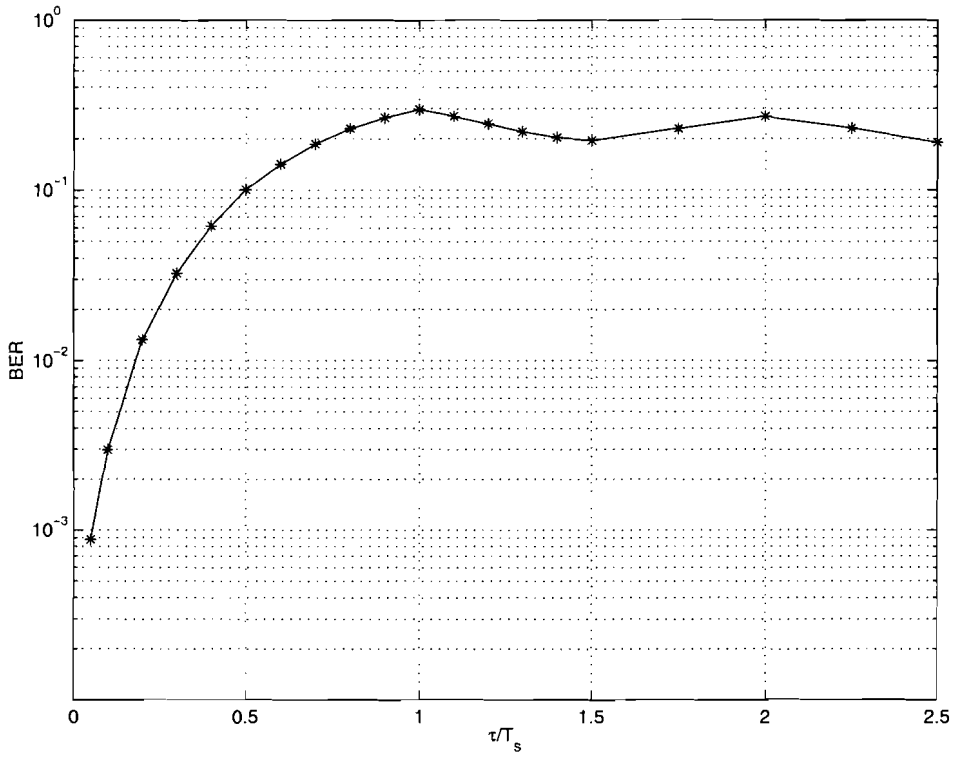

Figure 5.17: **BER versus τ/T_s in the two-ray Rayleigh fading model**

5.5 Conclusions

The simulations performed with an AWGN channel for three modulation techniques, BPSK, QPSK and $\pi/4$ DQPSK, are compared with analytically derived bit error rate curves. From the results can be concluded that the simulation results agree with the theoretical curves. Therefore it can be concluded that the AWGN channel and the different modulation techniques are correctly implemented in Simulink.

The system is extended with Rayleigh flat fading. Simulation are performed with BPSK modulation and the results are compared with the analytically derived error rate function for Rayleigh flat fading with BPSK modulation. From this comparison it can be concluded that the simulation results agree with the theoretical curve and therefore it can be concluded that the flat fading channel is correctly implemented in Simulink. Furthermore it can be concluded that the flat fading channel causes a considerable degradation in performance compared to the performance of an AWGN channel.

Finally, frequency selectivity is added to the system by means of a two-ray model. The simulation results are compared with simulations in literature [26] and match well. From this it can be conclude that the frequency selectivity is implemented well in the system.

The Simulink models described in this chapter can be used as a base for the measurement based model.

Chapter 6

Measurement Based Indoor Radio Channel Model

6.1 Introduction

In the previous chapter, simulations were performed with different radio channel models. First the simplest form of a radio channel model, the AWGN channel, was implemented in Simulink. After that the model was extended with multipath and frequency selectivity. In this chapter the model is extended with the results of measurements and a measurement based indoor radio channel model is obtained. The measurements were performed in an indoor environment, i.e. a room in one of the buildings of Philips Natlab (see section 2.6).

Section 6.2 starts with the presentation of some measurement parameters. After that the distance between the taps (or bins) is obtained (section 6.3). The distance between the taps (bins) is also called the binwidth. The binwidth is determined and 8 bins are used for the tapped delay line (section 6.4) and simulations are performed with the 8-bins model (section 6.5). Finally, conclusions are drawn in section 6.6.

6.2 Measurement parameters

The model of the indoor radio channel is based on the measurement named "Measurement 1" which is described in section 2.6 and Table 2.1. The bandwidth, BW, of the measurement is 400 MHz. The resolution in the time domain T_{res} is the reciprocal of the bandwidth and is 2.5 ns. The number of point per frequency step $N = 1601$, resulting in frequency steps $\Delta f = 250$ kHz. The total time of the impulse response is

$$T_{tot} = (N-1) \cdot T_{res} = 4\mu s \quad . \tag{6.1}$$

The measurement is performed at 2401 points in the xy-plane, i.e. 3 wavelengths in the x- and 3 wavelengths in the y-direction with 16 points per wavelength.

6.3 Determination of the binwidth

The impulse response can be implemented in a tapped delay line (TDL). The number of tap, also called bins, and the distance between the taps (=the binwidth), can be adjusted. In this section the number of bins and the binwidth of the measurement based model are determined. A maximum bit rate of 8 Mbit/s is assumed. This is high enough because communication systems at approximately 2 GHz, like DECT, UMTS and Bluetooth have maximum bit rates of a few Mbit/s. The symbol time of QPSK modulation at 8 Mbit/s is 250 ns. In the simulations one symbol consists of 100 samples, which means a sample time of 2.5 ns for 8 Mbit/s. 2.5 ns is also the resolution of the impulse response.

6.3.1 Rectangular pulse shape

In Figure 6.1 an example of a normalised impulse response is shown together with a rectangular pulse with a bit rate of 8 Mbit/s. The received signal is obtained by convolution of the input pulse and the impulse response of the radio channel. Convolving the pulse from Figure 6.1 with the impulse response from Figure 6.1 results in the signal shown in Figure 6.2. The resolution of the impulse response in this case is 2.5 ns as mentioned

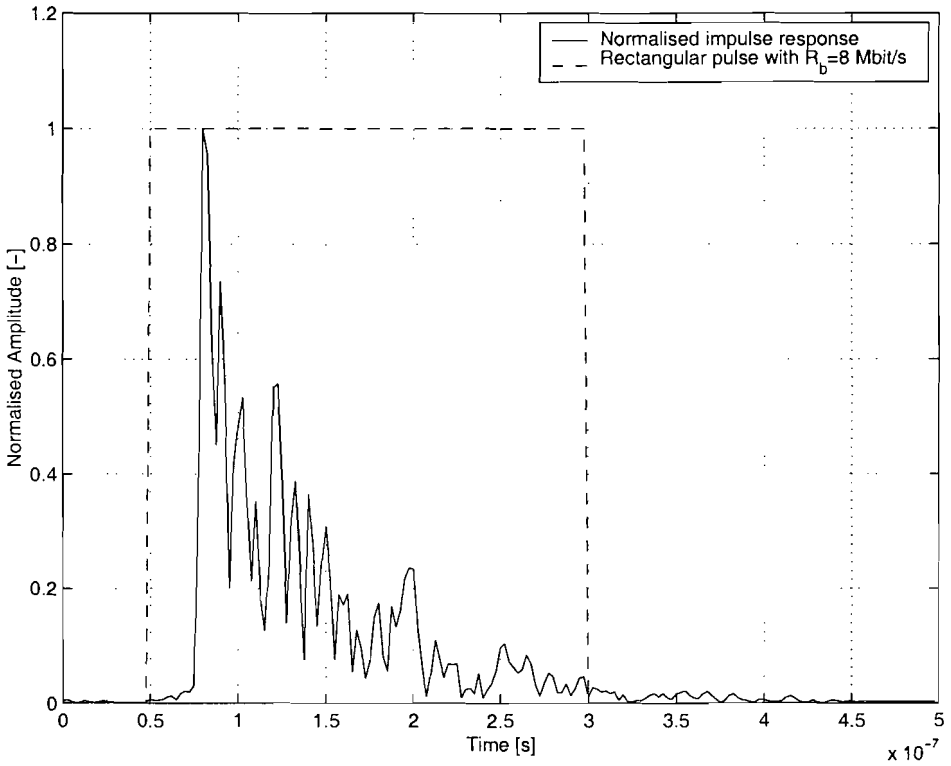

Figure 6.1: **Normalised impulse response, solid line, and a rectangular pulse, dashed line.**

earlier. At approximately 300 ns after the maximum value, the impulse response is drown in noise. A model with a resolution of 2.5 ns and 300 ns duration would require 120 bins. This results in large simulation times. A smaller number of bins results in faster simulations, however the smaller the number of bins, the more inaccurate the model. The

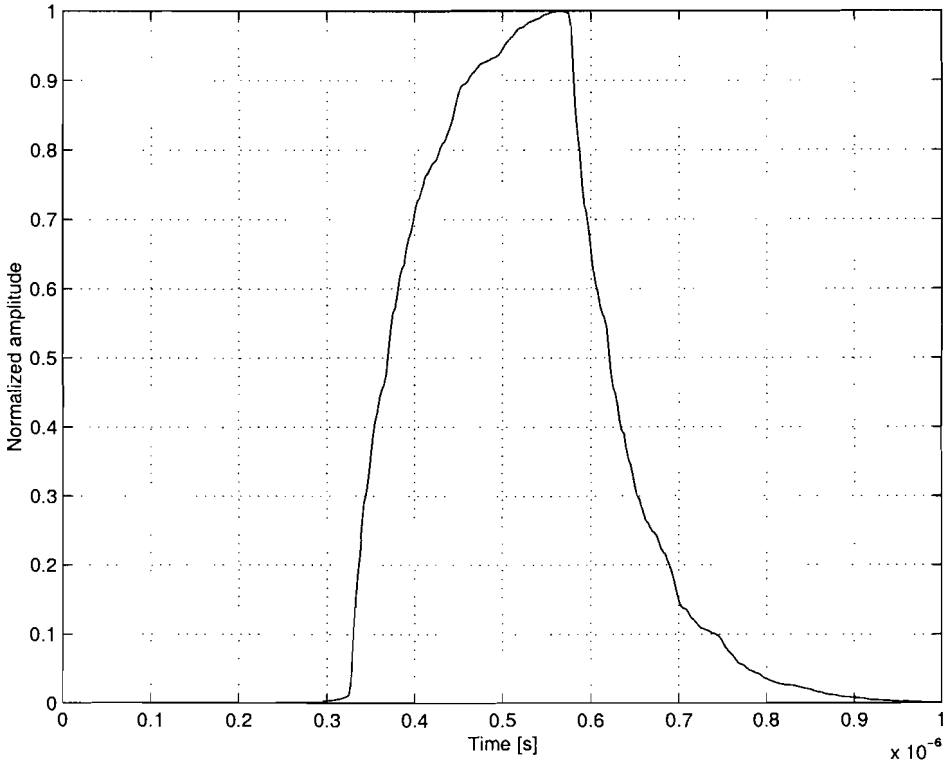

Figure 6.2: **Convolution of the impulse response and rectangular pulse.**

bins are determined with

$$B_n = \sqrt{\frac{1}{N} \sum_{k=(n-1)\cdot N+1}^{n\cdot N} h_k^2} \quad , \tag{6.2}$$

where B_n denotes the amplitude of the n th bin, N is the number of points within the bin interval and h_k is the amplitude of the k th point of the impulse response.

Now the bins for three different models are derived. Model 1 has 16 bins and a binwidth of 8 points ($N = 8$), model 2 has 8 bins and a binwidth of 16 points ($N = 16$) and model 3 has 5 bins and a binwidth of 32 points ($N = 32$).

Model 1

The bins for a binwidth of 8 corresponding with a binwidth of 8 $\times$ 2.5 ns = 20 ns and a total number of 16 bins, corresponding with a length of 300 ns are calculated with (6.2) and shown in Figure 6.3. Also shown in the figure is the convolution of these bins with the rectangular pulse from Figure 6.1 and the convolution from Figure 6.2.

Model 2

The bins for a binwidth of 16 corresponding with a binwidth of 16 $\times$ 2.5 ns = 40 ns and a total number of 8 bins, corresponding with a length of 280 ns are determined and shown in Figure 6.4. Also shown in the figure is the convolution of these bins with the rectangular pulse from Figure 6.1 and the convolution from Figure 6.2.

Model 3

The bins for a binwidth of 32 corresponding with a binwidth of 32 $\times$ 2.5 ns = 80 ns and a

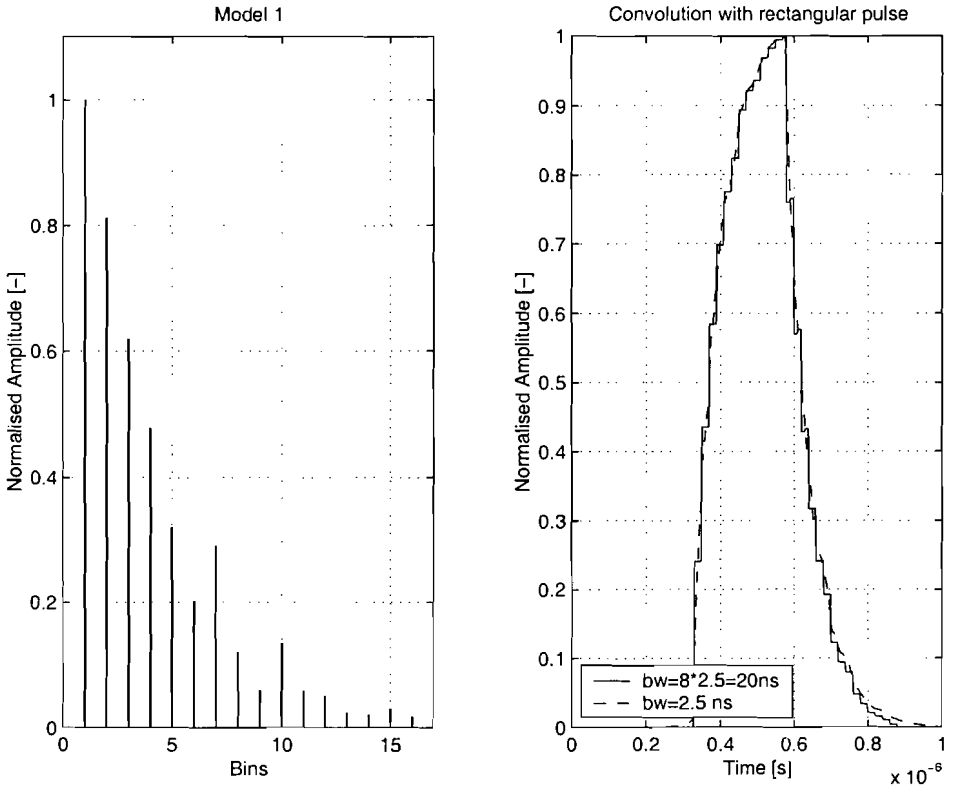

Figure 6.3: **The convolution of model 1 with a rect. pulse with R_b=8 Mbit/s.**

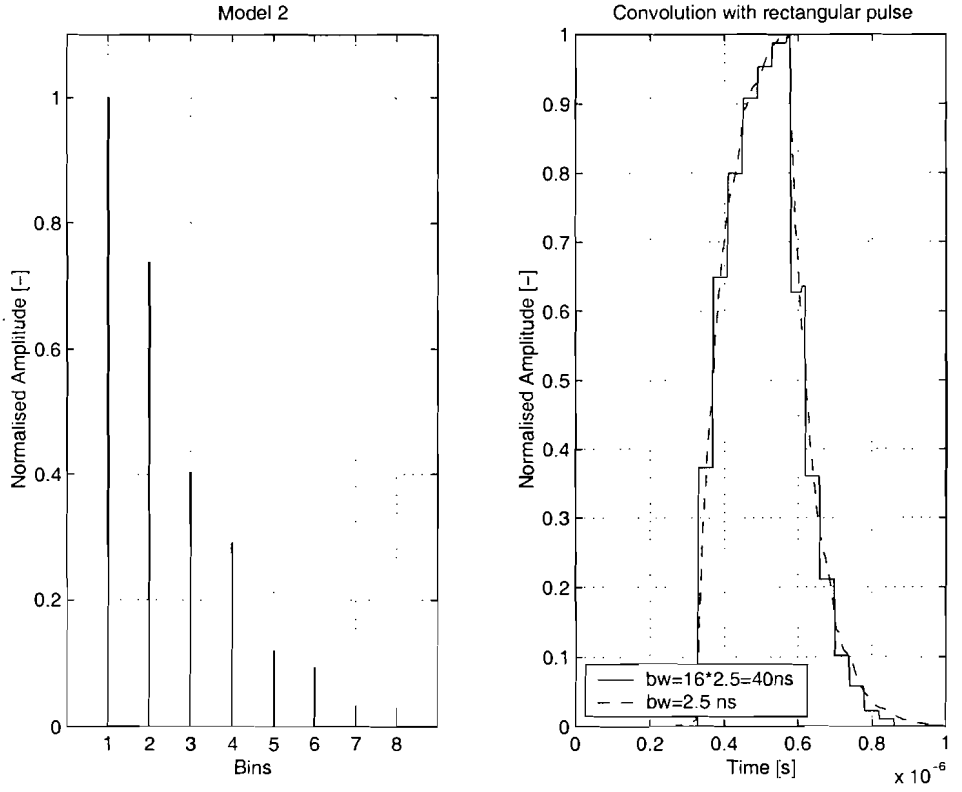

Figure 6.4: **The convolution of model 2 with a rect. pulse with R_b=8 Mbit/s.**

total number of 5 bins, corresponding with a length of 320 ns are determined and shown in Figure 6.5. Also shown in the figure is the convolution of these bins with the rectangular pulse from Figure 6.1 and the convolution from Figure 6.2.

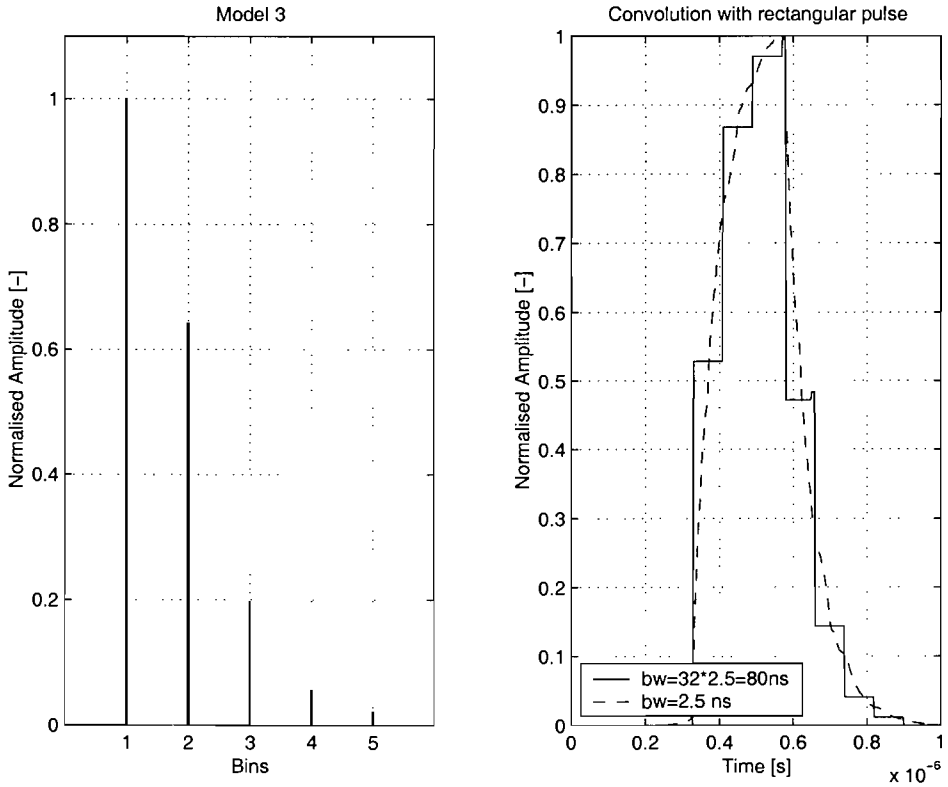

Figure 6.5: **The convolution of model 3 with a rect. pulse with R_b=8 Mbit/s.**

Discrepancy

The discrepancy D between model 1, model 2, model 3 and the impulse response can be calculated with

$$D = \sqrt{\frac{1}{M}\sum_{n=1}^{M}(x_n - y_n)^2} \quad , \tag{6.3}$$

where M is the number of points in the time domain (120 in this case), x_n is the amplitude of the impulse response at the n th position and y_n is the amplitude of the bin if the bin is present at that position or else $y_n = 0$. The discrepancy for various binwidths is shown in Table 6.1.

A compromise has to be found between the discrepancy and the speed of the simulations. In this report model 2 is used. This means the discrepancy is less than 5 % and the number of bins is 8.

Table 6.1: **Discrepancy between the measured impulse response and the models for rectangular pulses.**

Model	Binwidth bw [ns]	Number of bins	Discrepancy [%]
1	$8 \times 2.5 = 20$ ns	16	2.21 %
2	$16 \times 2.5 = 40$ ns	8	4.34 %
3	$32 \times 2.5 = 80$ ns	5	8.08 %

6.3.2 Gaussian pulse shape

In this section the pulse shape is Gaussian instead of rectangular. The received signal is obtained by convolution of the input pulse and the impulse response of the radio channel. Convolving the Gaussian pulse from Figure 6.6 with the impulse response from Figure 6.6 results in the signal shown in Figure 6.7. The results of the convolutions are shown in Table 6.2. In the table it can be seen that for a discrepancy smaller than 5% a model with 5 bins with a binwidth of 32 can be used.

Table 6.2: **Discrepancy between the measured impulse response and the models for Gaussian pulses.**

Model	Binwidth bw [ns]	Number of bins	Discrepancy [%]
1	$8 \times 2.5 = 20$ ns	16	0.58 %
2	$16 \times 2.5 = 40$ ns	8	1.28 %
3	$32 \times 2.5 = 80$ ns	5	3.79 %
4	$50 \times 2.5 = 125$ ns	4	6.22 %

6.3.3 Conclusions

Different models are determined and convoluted with rectangular pulses and Gaussian pulses. It can be concluded that the performance is better if Gaussian pulses are used instead of rectangular pulses. Furthermore it is shown that for the 8-bins model with rectangular pulses the discrepancy is less than 5%.

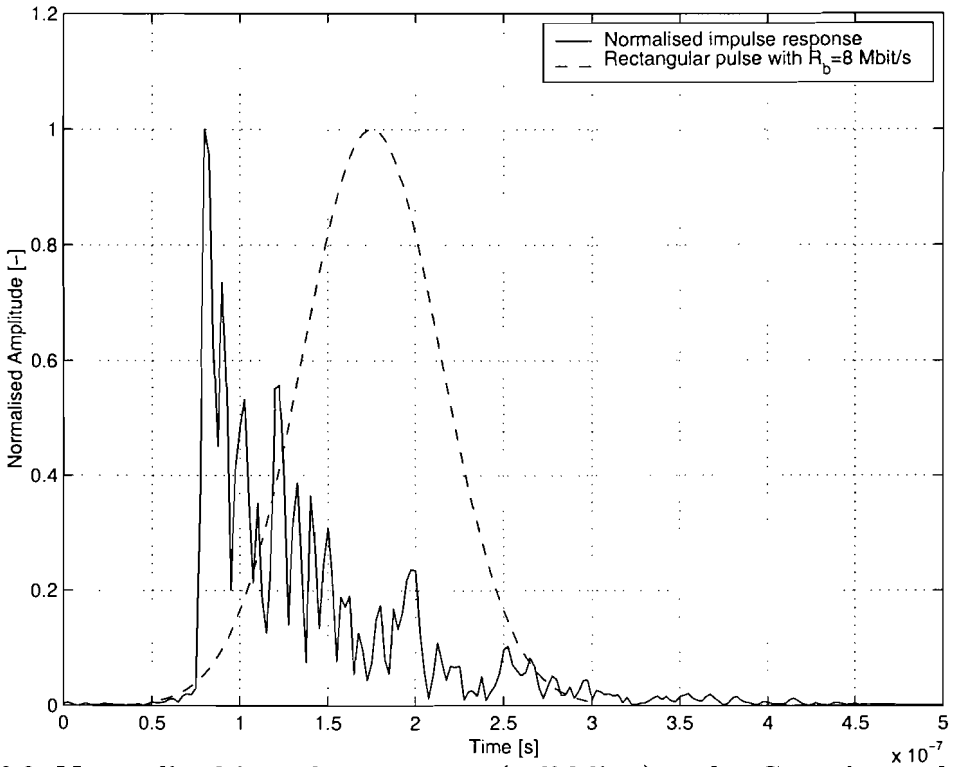

Figure 6.6: **Normalised impulse response (solid line) and a Gaussian pulse with R_b=8 Mbit/s (dashed line).**

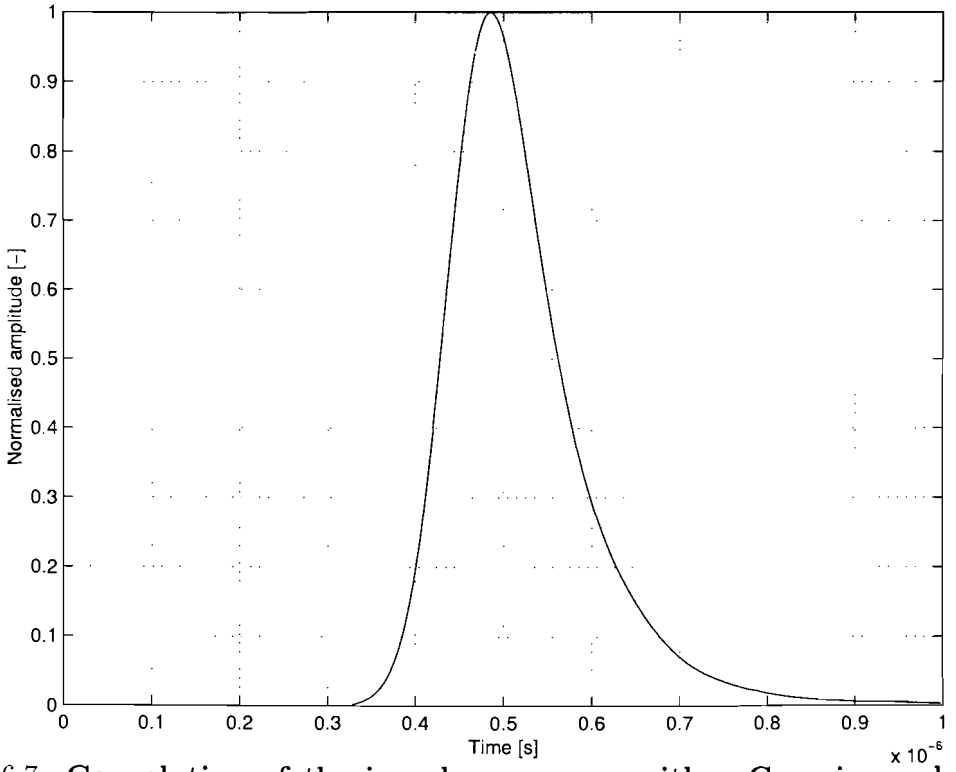

Figure 6.7: **Convolution of the impulse response with a Gaussian pulse with R_b=8 Mbit/s.**

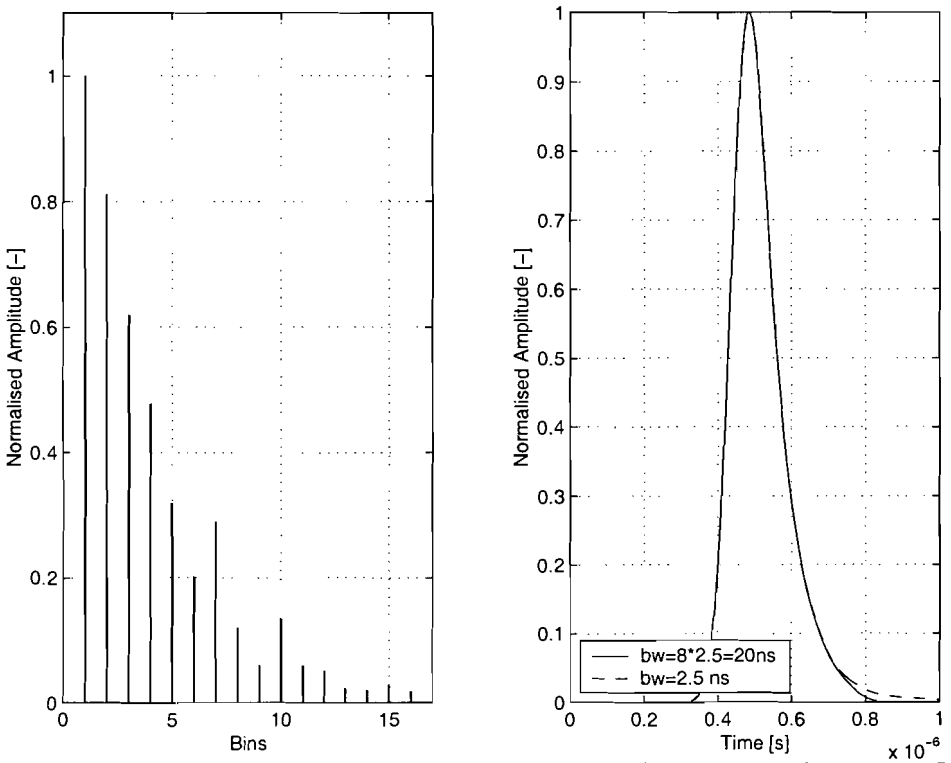

Figure 6.8: **The convolution of model 1 with a Gaussian pulse with R_b=8 Mbit/s.**

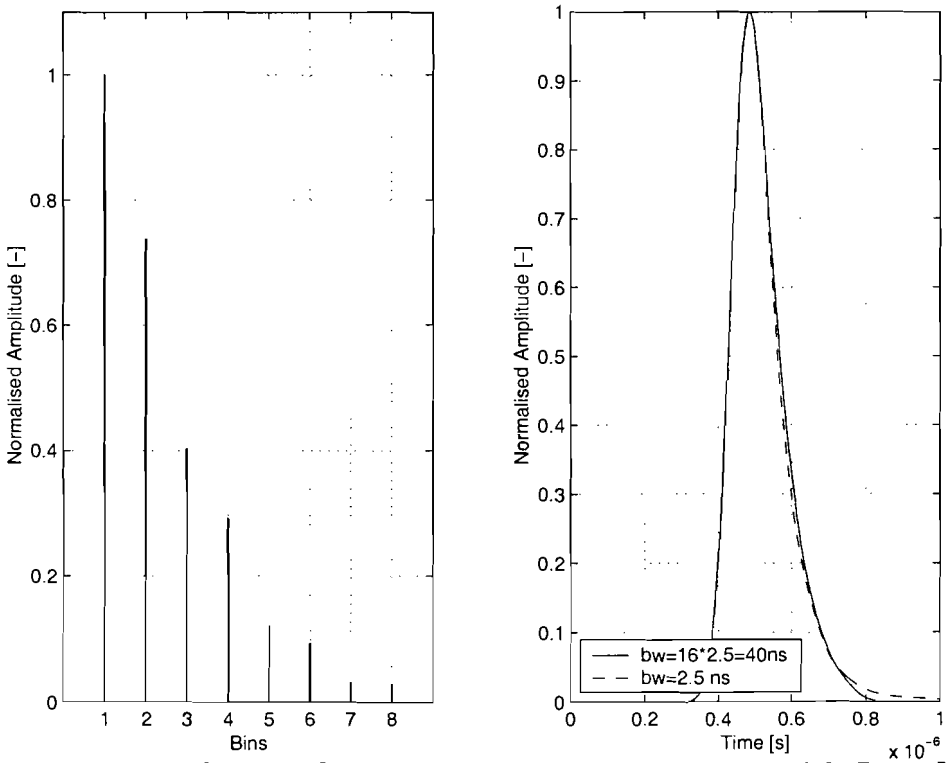

Figure 6.9: **The convolution of model 2 with a Gaussian pulse with R_b=8 Mbit/s.**

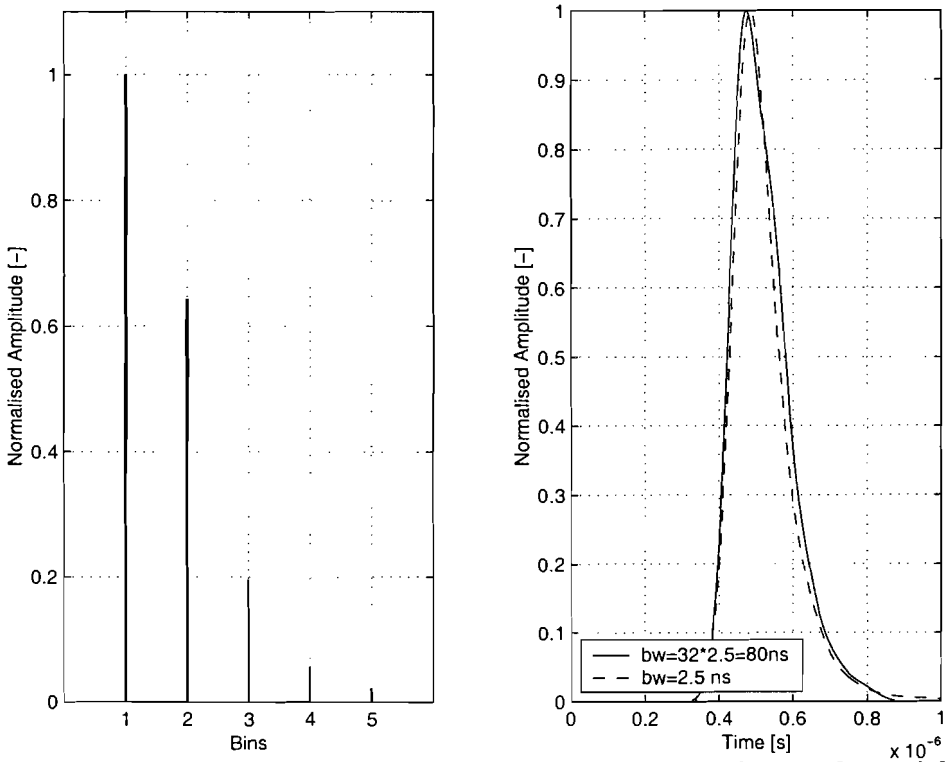

Figure 6.10: **The convolution of model 3 with a Gaussian pulse with R_b=8 Mbit/s.**

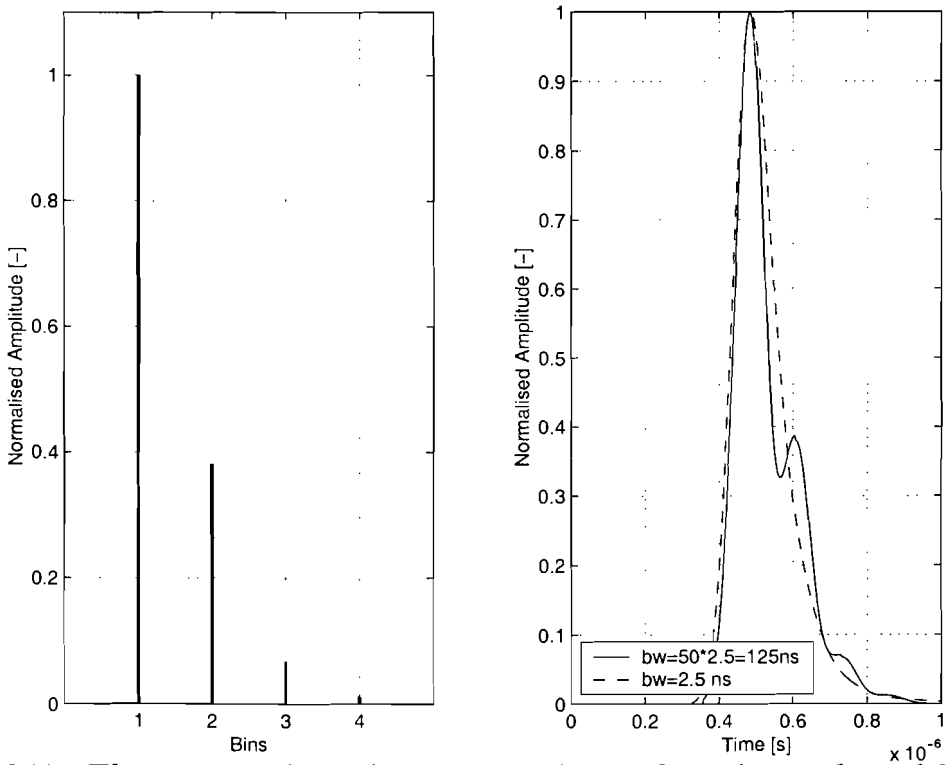

Figure 6.11: **The convolution of model 3 with a Gaussian pulse with R_b=8 Mbit/s.**

6.4 8-bins model

Rectangular pulses can easily be implemented in Simulink and are therefore used for the simulations. In this case 8 bins are used to model the measurement. The width of each bin is 40 ns which corresponds to 16 points in time and the total length of the model is 280 ns.

Before the bins can be determined, each impulse response has to be scaled to provide the maximum value is positioned in the middle of the first interval. This is shown in Figure 6.12 A tapped delay line is used for the model. The amplitudes of the coefficients are Rayleigh distributed, while the phases are uniformly distributed within $[0, 2\pi]$. The only parameter in the Rayleigh distribution is σ and the power of the Rayleigh distribution is σ^2. The energy of an impulse response in a bin interval at a certain position in the xy-plane is determined as

$$E_n(x,y) = \frac{1}{N} \sum_{k=(n-1)\cdot N+1}^{n\cdot N} h^2_{k(x,y)} \quad , \tag{6.4}$$

where $E_n(x,y)$ is the energy of the n th bin at position (x,y) in the xy-plane, N is the number of points in the bin interval and $h_{k(x,y)}$ is the amplitude of k th point of the impulse response at position (x,y) in the xy-plane.

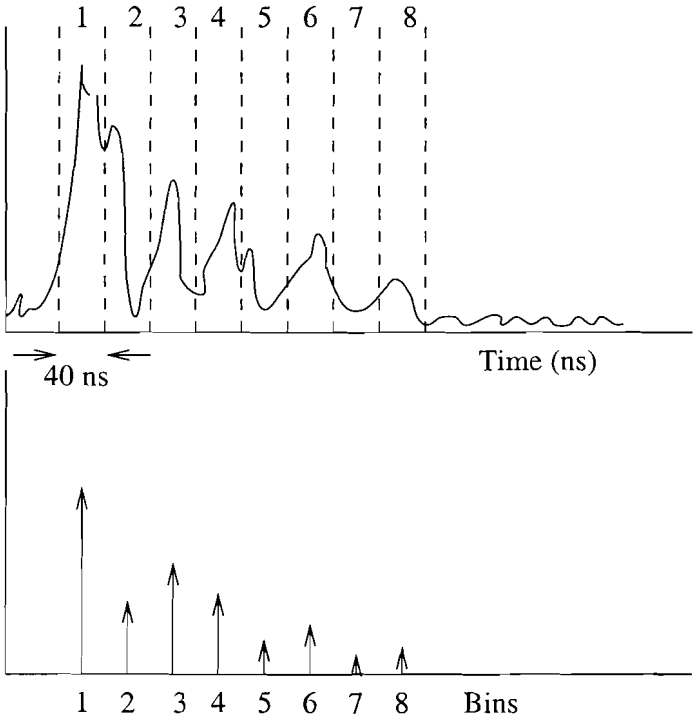

Figure 6.12: **8-bins model**

First the bins for each position in the xy-plane are determined, then the bins of the whole xy-plane are determined by averaging over the xy-plane.

The values of the 8-bins are shown in Table 6.3 and Figure 6.13.

Table 6.3: **Coefficients of the measurement based 8-bins model.**

Bin	Phase	Amplitude	σ
1	Uniform $[0, 2\pi]$	Rayleigh	1.00×10^{0}
2	Uniform $[0, 2\pi]$	Rayleigh	4.96×10^{-1}
3	Uniform $[0, 2\pi]$	Rayleigh	2.56×10^{-1}
4	Uniform $[0, 2\pi]$	Rayleigh	1.67×10^{-1}
5	Uniform $[0, 2\pi]$	Rayleigh	9.22×10^{-2}
6	Uniform $[0, 2\pi]$	Rayleigh	5.70×10^{-2}
7	Uniform $[0, 2\pi]$	Rayleigh	3.06×10^{-2}
8	Uniform $[0, 2\pi]$	Rayleigh	1.87×10^{-2}

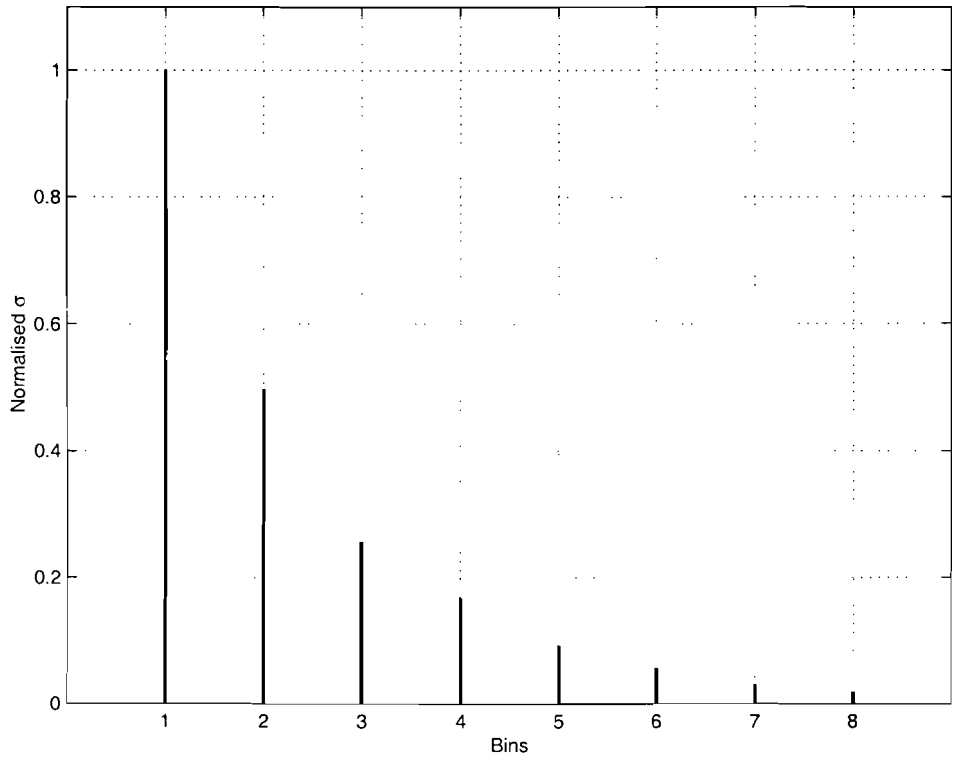

Figure 6.13: **Bins of the measurement based 8-bins model.**

Delay spread

The rms delay spread for this model can be calculated with (4.15) in Section 4.7 and is 31.3 ns.

6.5 Simulations

The coefficients of the bins are determined in the previous section and can be implemented in the model. The simulations with the measurement based 8-bins model are performed in the same way as the simulations with the two-ray model from Section 5.4. The total system used for the simulations is shown in Figure 6.14 and the 8-bins model in Figure 6.15. $\pi/4$ DQPSK modulation is used in the simulations. The advantage of $\pi/4$ DQPSK modulation is that it can be non coherently detected, which greatly simplifies the receiver design. Furthermore, $\pi/4$ DQPSK has a good performance in a multipath environment. The disadvantage of $\pi/4$ DQPSK is that it needs approximately 2-3 dB extra E_b/N_o for the same BER (Figure 5.10).

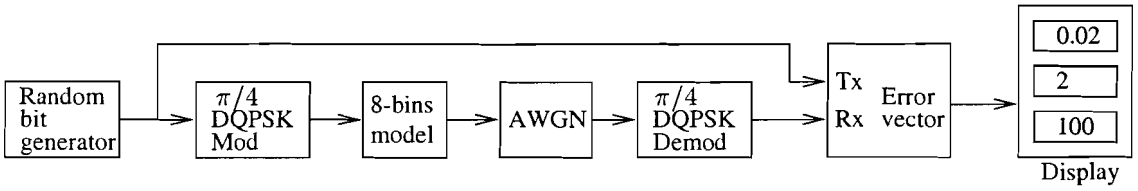

Figure 6.14: **Simulink model total system 8-bins model.**

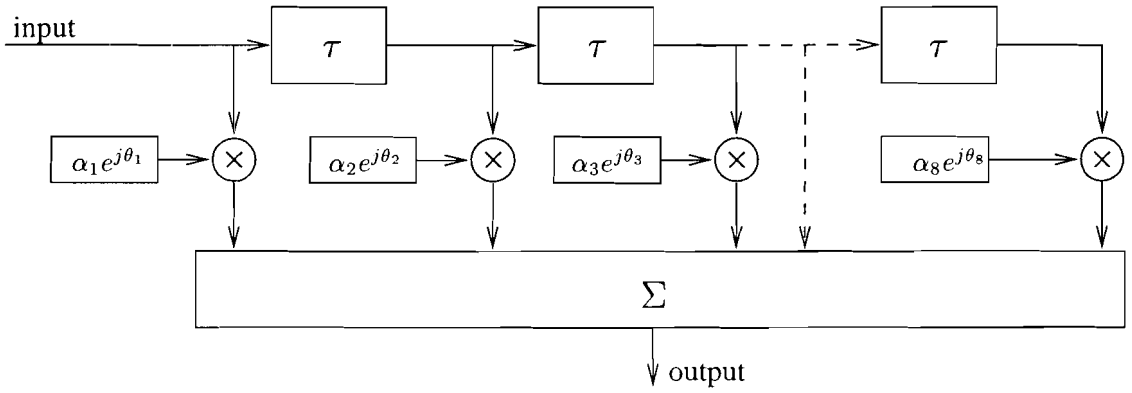

Figure 6.15: **8-bins model.**

The simulations are performed for different bit rates and the BER is determined as a function of the ratio E_b/N_o. The results of the simulations are shown in Figure 6.16. The bit-error-rate curve for $\pi/4$ DQPSK modulation in an AWGN channel is also plotted in the figure. In the figure it can be seen that the BER increases for increasing bit rates. This is in agreement with the theory. Furthermore it can be seen that for large E_b/N_0 an error floor occurs. This error floor or irreducible error floor is caused by the time dispersion of the indoor radio channel.

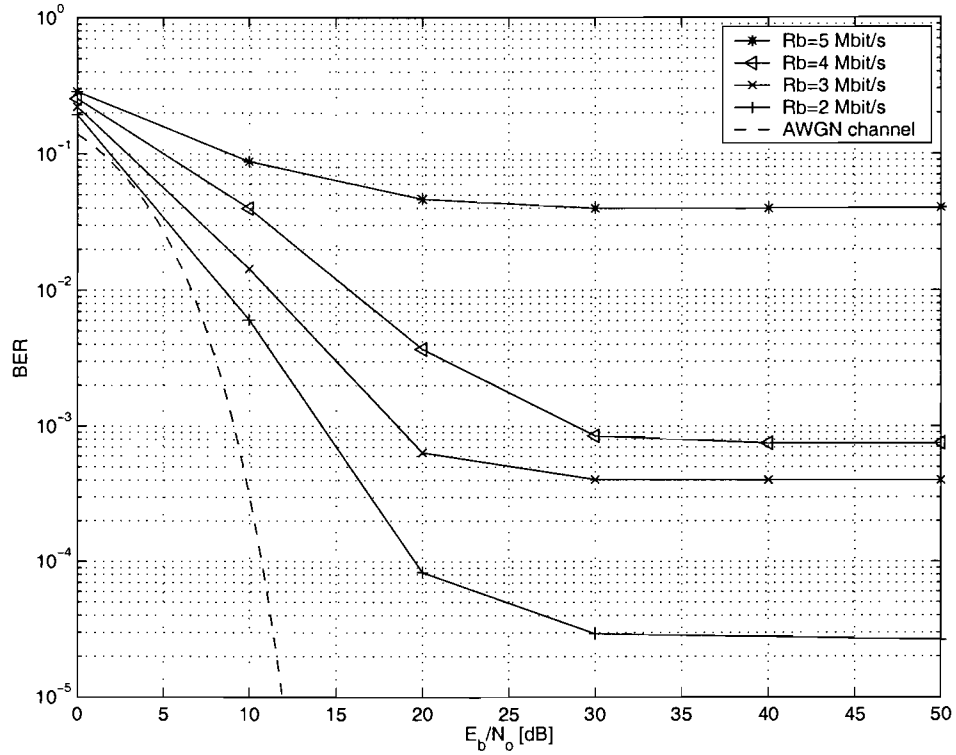

Figure 6.16: **BER versus E_b/N_o in the 8-bins measurement based model with $\pi/4$ DQPSK modulation.**

6.6 Conclusions

In this chapter it is shown that for the 8-bins model with rectangular pulses the discrepancy is less than 5%.

The indoor radio channel is implemented in a tapped delay line with 8 bins. Simulations are performed with this so called measurement based indoor radio channel model. The bit error rate is obtained for different bit rates as a function of E_b/N_o. From these simulations (Figure 6.16) can be concluded that the shape of the curves corresponds with our expectations, i.e. an irreducible error floor occurs and the BER is larger for higher bit rates.

Chapter 7

Pulse Shaping

7.1 Introduction

In the simulations rectangular pulses have been used. However, rectangular pulses have an infinite bandwidth and can not physically be built. In practise other pulse shapes are used. For example the Gaussian and the raised cosine pulse shape. Both pulse shapes are described in this chapter.

7.2 Nyquist criterion

As a result of the band limited radio channel rectangular pulses will spread in time. The pulse for each symbol will smear into the time interval of succeeding symbols. This results in inter symbol interference (ISI) which decreases the performance of the system. One way to overcome the problem of ISI is to make sure the effect of ISI is zero at the sampling time. In formula form this condition is defined as

$$h_{eff}(nT_s) = \begin{cases} K & n = 0 \\ 0 & n \neq 0 \end{cases} \tag{7.1}$$

where n is an integer and T_s is the symbol time. This condition is called the Nyquist criterion for ISI cancellation.

7.3 The Gaussian Filter

7.3.1 Definitions

The Gaussian low-pass filter has a transfer function given by [6]

$$H_G(f) = e^{-\alpha^2 \cdot f^2} \quad , \tag{7.2}$$

and is plotted in Figure 7.1.

The 3-dB bandwidth is defined as the frequency at which the power decrease is 3-dB or a factor 2. In that case the amplitude decreases with a factor $\sqrt{2}$. The parameter α is

related to B, the 3-dB bandwidth of the baseband Gaussian shaping filter,

$$\alpha = \frac{\sqrt{ln2}}{\sqrt{2} \cdot B} = \frac{0.5887}{B} \quad . \tag{7.3}$$

As α increases, the spectral occupancy of the Gaussian filter decreases and time dispersion of the applied signal increases. The impulse response of the Gaussian filter is given by

$$h_G(t) = \frac{\sqrt{\pi}}{\alpha} \cdot e^{-\frac{\pi^2}{\alpha^2} \cdot t^2} \quad , \tag{7.4}$$

and is plotted in Figure 7.2.

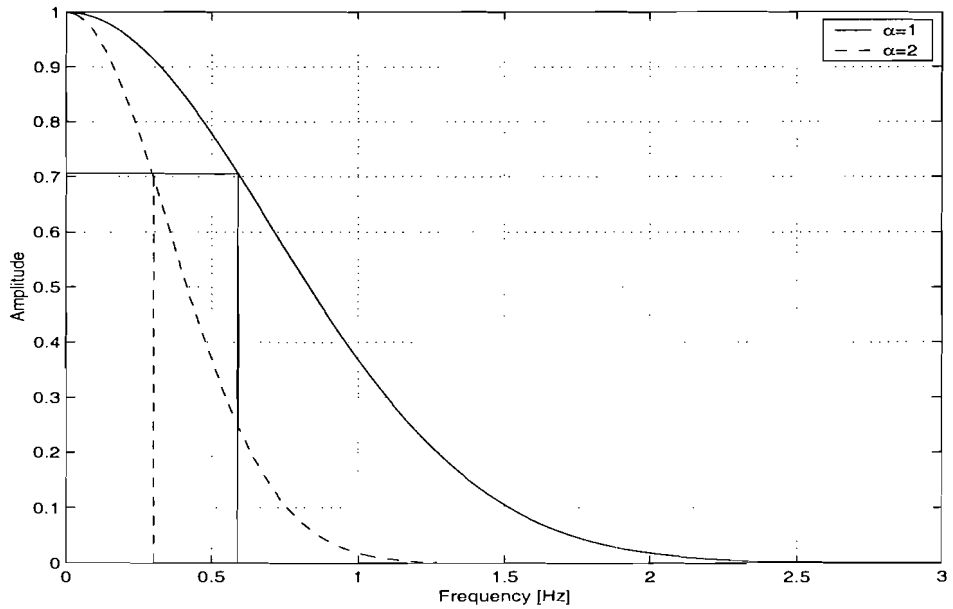

Figure 7.1: **Gaussian filter in the frequency domain.**

The Gaussian pulse-shaping filter does not satisfy the Nyquist criterion for ISI cancellation and therefore ISI occurs. Thus, a trade-off is made between the desired RF bandwidth and the irreducible error due to ISI of adjacent symbols.

The Gaussian pulse is completely described by its BT_s-product, where B is defined in (7.3) and T_s is the symbol period which is the inverse of the symbol rate.

7.3.2 Transmit and Receive Filter

In a communication system the pulse-shaping is provided by a transmit and a receive filter. In [25] is derived that the performance of the system is optimum if the pulse-shaping is equally divided between the transmit and the receive filter, which means that the receive filter $H_T(f)$ and the transmit filter $H_R(f)$ have the same transfer function

$$H_T(f) = H_R(f) = \sqrt{H_G(f)} = \sqrt{e^{-\alpha^2 \cdot f^2}} \quad . \tag{7.5}$$

This equation can be written as

$$H_T(f) = H_R(f) = e^{-\frac{1}{2} \cdot \alpha^2 \cdot f^2} \quad . \tag{7.6}$$

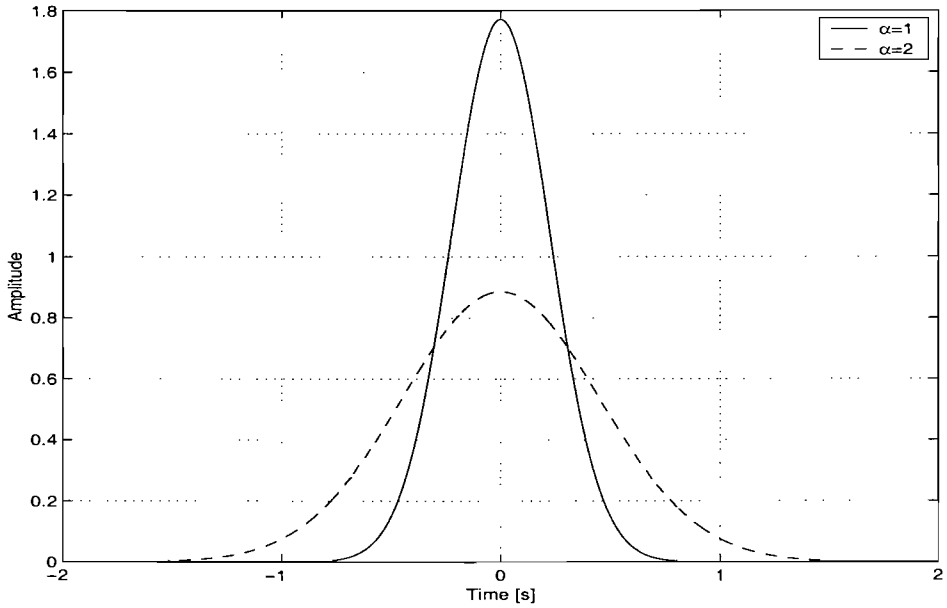

Figure 7.2: **Gaussian filter in the time domain.**

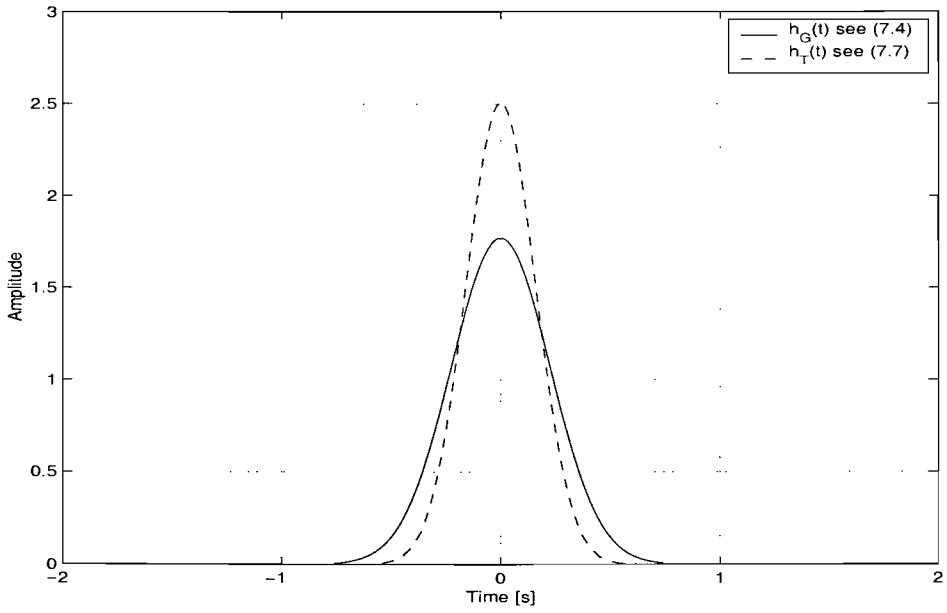

Figure 7.3: **Impulse responses of the Gaussian pulse shape, $h_G(t)$, and its transmit filter, $h_T(t)$.**

The impulse response of these filters can be derived from (7.4) by replacing α by $\frac{\alpha}{\sqrt{2}}$ and becomes

$$h_T(t) = h_R(t) = \frac{\sqrt{2 \cdot \pi}}{\alpha} \cdot e^{-2 \cdot \frac{\pi^2}{\alpha^2} \cdot t^2} \quad , \tag{7.7}$$

and is shown in Figure 7.3.

7.4 The Raised Cosine Rolloff Filter

7.4.1 Definitions

The raised cosine belongs to the class of filters which satisfy the Nyquist criterion (see section 7.2). The transfer function of the raised cosine filter is given by

$$H_{RC}(f) = \begin{cases} 1 & 0 \leq |f| \leq (1-\alpha)/2Ts \\ \frac{1}{2}\left[1 + \cos\left(\frac{\pi[(2T_s \cdot |f|) - 1 + \alpha]}{2 \cdot \alpha}\right)\right] & (1-\alpha)/2Ts \leq |f| \leq (1+\alpha)/2Ts \\ 0 & |f| > (1+\alpha)/2Ts \end{cases} \tag{7.8}$$

where α is the rolloff factor which ranges between 0 and 1. The raised cosine transfer function is plotted in Figure 7.4 for different values of α. For $\alpha = 0$ the filter is a rectangular filter of minimum bandwidth.

The impulse response is given by

$$h_{RC}(t) = \left(\frac{\sin(\pi t/T_s)}{\pi t}\right) \cdot \left(\frac{\cos(\pi \alpha t/T_s)}{1 - [4\alpha t/(2T_s)]^2}\right) \quad . \tag{7.9}$$

The impulse response of the raised cosine filter can be seen in Figure 7.5.

In the figures it can be seen that increasing the bandwidth results in a decrease in sidelobe level of the impulse response. Thus, there is a tradeoff between the bandwidth and the sidelobe-level. An additional advantage of the raised cosine filter with $\alpha = 1$ is the occurrence of extra zero-crossings at $\frac{3}{2}T_s, \frac{5}{2}T_s, etc.$

From (7.8) the symbol rate can be derived as

$$R_s = \frac{B}{1+\alpha} \quad . \tag{7.10}$$

From this formula the BT_s-product can be derived as

$$BT_s = 1 + \alpha \quad , \tag{7.11}$$

and ranges between 1 and 2.

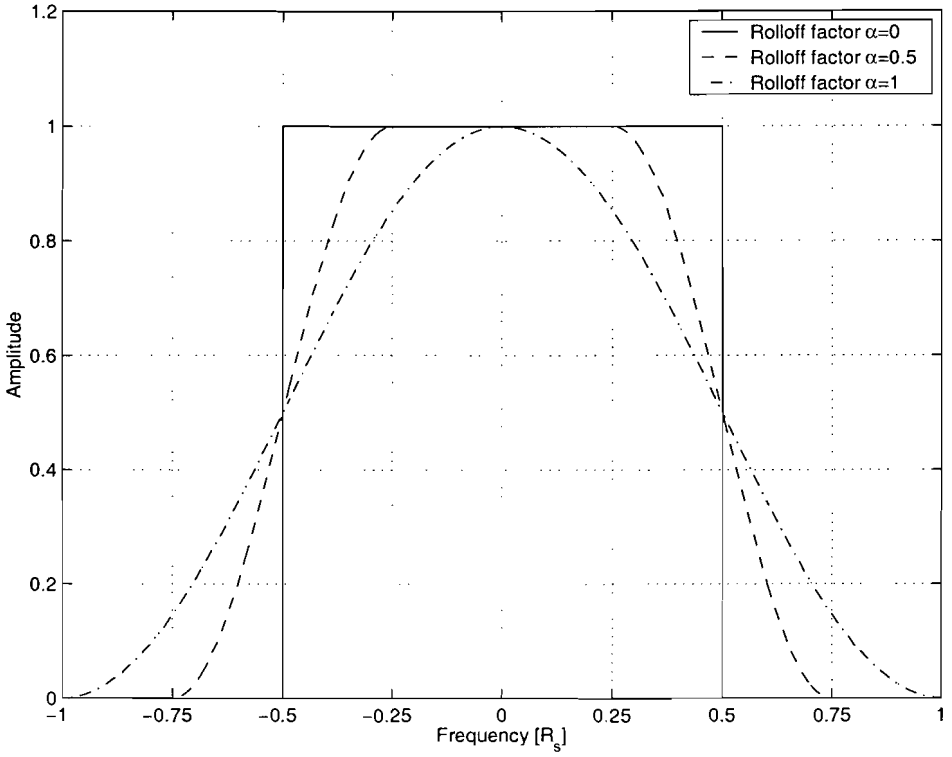

Figure 7.4: **Raised cosine rolloff filter in the frequency domain**

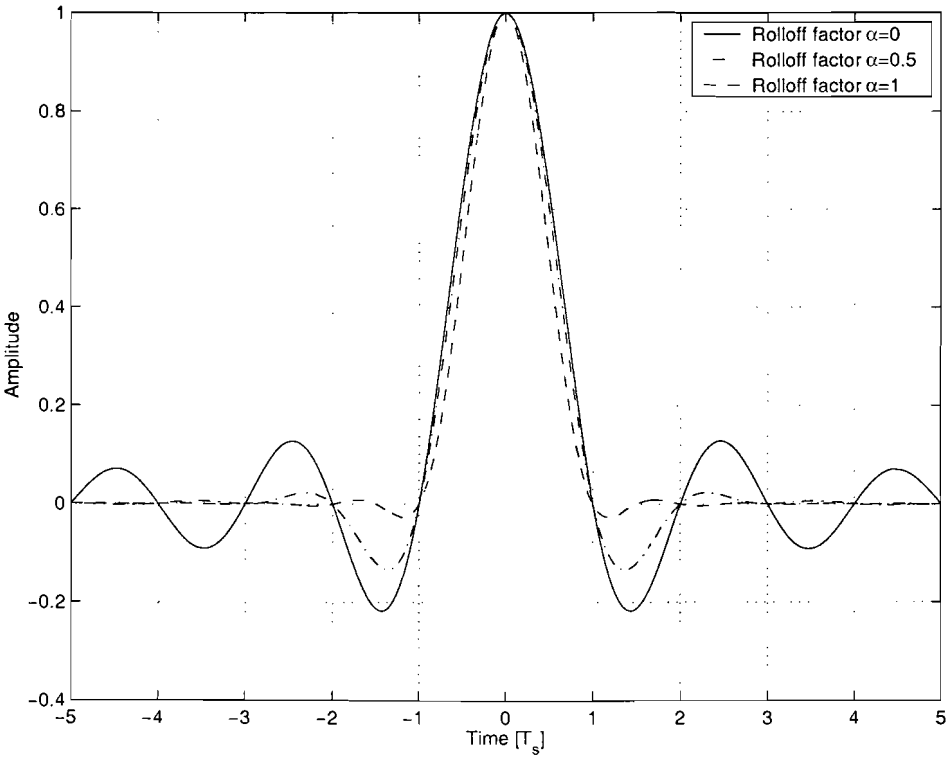

Figure 7.5: **Raised cosine rolloff filter in the time domain**

7.4.2 Transmit and Receive Filter

The transmit and receive filter can be derived from (7.8) with

$$H_T(f) = H_R(f) = \sqrt{H_{RC}(f)} \quad . \tag{7.12}$$

The impulse response of the transmit and receive filter can be obtained by taking the inverse Fourier Transform. The impulse responses for various values of α are presented below.

Transmit and receive filter with $\alpha = 0$
For $\alpha = 0$ the transfer function becomes

$$H_{RC}(f) = 1 \quad , \tag{7.13}$$

for $-\frac{1}{2T_s} \leq f \leq \frac{1}{2T_s}$ and zero elsewhere. With (7.12) the transmit and receive filter for $\alpha = 0$ is equal to $H_{RC}(f)$ and therefore the impulse response is the same as the impulse response in (7.9) with $\alpha = 0$

$$h_{T,RC}(t) = \left(\frac{\sin(\pi t/T_s)}{\pi t}\right) \quad . \tag{7.14}$$

Transmit and receive filter with $\alpha = 0.5$
The impulse response of the transmit and receive filter for the Raised Cosine pulse shaping with $\alpha = 0.5$ is derived in Appendix A and is

$$h_{T,RC}(t) = \frac{1}{\pi\left(1 - 4t^2R^2\right)}\left[\frac{1}{t}\sin\left(\frac{1}{2}\pi tR\right) + 2R\cos\left(\frac{3}{2}\pi tR\right)\right] \quad . \tag{7.15}$$

Transmit and receive filter with $\alpha = 1$
For $\alpha = 1$ the transfer function (7.8) becomes

$$\begin{aligned} H_{RC}(f) &= \frac{1}{2}\left[1 + \cos\left(\frac{\pi[(2T_s \cdot |f|) - 1 + \alpha]}{2 \cdot \alpha}\right)\right] && (7.16)\\ &= \frac{1}{2}\left[1 + \cos\left(\pi \cdot T_s \cdot |f|\right)\right] && (7.17)\\ &= \frac{1}{2}\left[1 + \cos\left(\pi \cdot T_s \cdot f\right)\right] && (7.18)\\ &= \cos^2\left(\frac{\pi}{2} \cdot T_s \cdot f\right) \quad , && (7.19) \end{aligned}$$

for $-\frac{1}{T_s} \leq f \leq \frac{1}{T_s}$ and zero elsewhere. With (7.12) the transmit and receive filter for $\alpha = 1$ becomes

$$H_{T,RC}(f) = \sqrt{H_{RC}} = \cos\left(\frac{\pi}{2}T_s f\right) \quad , \tag{7.20}$$

for $-\frac{1}{T_s} \leq f \leq \frac{1}{T_s}$ and zero elsewhere. With the aid of formula (5.26) and (5.27) in [25] the impulse response can be derived and becomes

$$h_{RC}(t) = \frac{1}{T_s} \cdot \frac{4 \cdot \cos\left(2\pi t/T_s\right)}{\pi \cdot \left(1 - 16 \cdot t^2/T_s^2\right)} \quad . \tag{7.21}$$

7.5 Conclusions

The impulse responses of the transmit and receive filter for the Gaussian pulse shape as well as the raised cosine pulse shape are derived in this chapter and implemented in Simulink. Because of the limited amount of time, the simulations of the BER are performed with rectangular pulses.

In GSM for example, Gaussian pulse shaping is used. If GSM has to be modelled it is recommended to implement the Gaussian pulse shaping in the model. The impulse responses of the transmit and receive filter derived in this chapter can then be used.

Chapter 8

Conclusions and Recommendations

8.1 Conclusions

In this report the foundation of a measurement based indoor radio channel model has been laid.

- Earlier measurements were performed in the frequency band 1.8-2.2 GHz. These measurements were not accurate, because of the interference of GSM 1800 and DECT in this frequency band. Therefore, I performed measurements in a clean frequency band from 2.0-2.4 GHz.
- The processing of the measured data is described in detail. Accurate impulse responses can be derived from the (frequency domain) measurements.
- The simulation results for the radio channel models, such as the AWGN channel, the Rayleigh flat fading channel and the two-ray model correspond with the theory, i.e. the simulated bit error rate corresponds with the analytically derived bit error rate function. Therefore it can be concluded that these models are implemented correctly.
- The 8-bins model gives a good approximation of the indoor radio channel.
- It is now possible to simulate the BER with $\pi/4$ DQPSK modulation based on a measurement.
- The simulations performed with the measurement-based indoor radio channel model correspond with the expectations, i.e. an irreducible error floor occurs and the BER is larger for higher bit rates.

8.2 Recommendations

To start with, measurements can be performed at different locations. The measurement based indoor radio channel model can be obtained for this specific location, and simulations

can be done to obtain the performance of the system. The performance of the system for different locations, with different rms delay spread, can be compared with each other and conclusion can be drawn.

With the simulation tool described in Chapter 5 various modulation techniques can be simulated for channels of which the BER is known, for example the AWGN channel, and compared with the theory. If the simulated bit error rate agrees with the theoretical bit error rate function, the modulation technique can be implemented in the measurement based model and the performance of the system for that specific modulation technique can be obtained.

QPSK modulation can be implemented in the model. The kind of detector needed for this modulation technique and the optimum detection moment can be investigated.

In this report only rectangular pulses are used for simulations. Different pulse shapes (see Chapter 7) can be implemented in the model and the effect of pulse shaping can be investigated.

Multi-carrier techniques like OFDM and space-time coding can be implemented in the model. Simulations can be performed with different parameter values and the parameter setting that gives the best performance can be obtained.

Finally, all the work described in this report is based on the frequency band 2.0-2.4 GHz, however all the work is also applicable for other frequencies. Measurements can be performed at other frequencies and the model for this frequency can be obtained.

Chapter 9

Acknowledgements

I would like to thank Philips for giving me the opportunity to perform my graduation project at Philips Research Laboratories Eindhoven. I would also like to thank my supervisors from the Eindhoven University of Technology, Prof. dr. ir. G. Brussaard and Dr. ir. P.F.M. Smulders and my supervisor from Philips, ir. L. Leyten for the supervision during my graduation project. Furthermore I wish to thank Guido Dolmans, Paul Mattheijssen, Jac Romme, Gerben Kuijpers and Wim Rouwet for the useful discussions.

Finally, I would like to thank all members and colleagues within the Integrated Transceivers Group and all my friends, my parents and my girl-friend for their continuous support and their interest in my project.

Jasper Siemons, June 2000

Bibliography

[1] Verstraeten, D., *"Karakterisering van 10 GHz en 17 GHz radiokanalen met behulp van microstrip antennes*, Philips Research Laboratories, Eindhoven, 1999, Technical Note 166/99

[2] Mangold, S., *Evaluation of the OFDM Multicarrier Transmission scheme for radio channels by means of Ray-Tracing"*, Philips Research Laboratories, Redhill, 1998, Technical Note No. 3666, 3/1998

[3] Beek, W.H.M. van. and Kerkhof, A.E.M. van de., *Radiokanaal modellering en karakterisering""*, Philips Research Laboratories, Eindhoven, 1998, Technical Note 813/98

[4] Smulders, P.F.M., *Broadband Wireless LANs: A Feasibility Study"*, Doctoral dissertation, Eindhoven University of Technology, 1995

[5] Dolmans, W.M.C., *"Effect of Indoor Fading on the Performance of an Adaptive Antenna System"*, Doctoral dissertation, Eindhoven University of Technology, 1997

[6] Rappaport, T.S., *Wireless Communications: Principles and Practice"*, Upper Saddle River, NJ: Prentice-Hall, 1996

[7] Enden, A.W.M. van den. and Verhoeckx, N.A.M., *"Digitale signaalbewerking*, DELTA PRESS BV, Second Edition, Amerongen, 1994

[8] Meerendonk, H.J.A. van den. and Smulders, P.F.M., *""On the Achievement of High Data Rates in Indoor Pico Cells"*, HTT-S European Wireless '98, Amsterdam, Oct '98, p. 75-80

[9] Dolmans, G. and Leyten, L., *Performance of an adaptive antenna handset for indoor communications*, IEE Proc. Microwave Antennas Propagation, Vol. 146, No. 2, April 1999, p. 138-144

[10] Ji-Hoon Park, Yungsoo Kim, Young-Sik Hur, Kyutae Lim and Ki-Ho Kim, *Analysis of 60 GHz Band Indoor Wireless Channels with Channel Configurations"*, Proc. of the ninth int. symp. on PIMRC'98, Vol. 2, p. 617-620, Boston, MA, USA, 8-11 sept. '98

[11] Rappaport, T.S., Seidel, S.Y. and Takamizawa, K., *"Statistical Channel Impulse Response Models for Factory and Open Plan Buildings Radio Communication*

System Design, IEEE Transactions on Communications, Vol. 39, No. 5, May 1991, p. 794-807

[12] Holloway, C.L., Cotton, M.G. and McKenna, P., *"A Model for Predicting the Power Delay Profile Characteristics Inside a Room""*, IEEE Transactions on Vehicular Technology, Vol. 48, No. 4, July 1999, p. 1110-1119

[13] Lacroix, D., Despins, C.L., Delisle, G.Y. and Spiegel, V., *Impulse Response Measurements in the UHF and SHF Bands for Outdoor Microcellular Quasi-static Environment"*, GLOBECOMM' 97, IEEE Global Telecommunication Conf. , Phoenix, AZ, USA, 3-8 Nov '97, Vol. 3, p. 1584-1588

[14] Mangold, S., Lott, M., Evans, D. and Fifield, R., *Indoor Radio Channel Modelling: Bridging from Propagation Details to Simulation""*, Proc. of Ninth Int. Symp. on Personal, Indoor, and Mobile Radio Communications, Boston, MA, USA, 8-11 Sept. 1998, Vol. 2, p. 625-629 Proc. of GLOBECOM '95, Singapore, 13-17 Nov. 1995, Vol. 1, p. 744-748

[15] Radi, H., Fiacco, M., Parks, M.A.N. and Saunders, S.R., *Simultaneous Indoor Propagation Measurements at 17 GHz and 60 GHz for Wireless Local Area Networks""*, Vehicular Technology Conf. '98, p.510-514

[16] Nobles, P. and Halsall, F., *Delay Spread and Received Power Measurements Within a Building at 2 GHz, 5 GHz and 17 GHz*, 10th Int. Conf. on Antennas and Propagation, 14-17 April 1997, Edinburgh, Vol. 2, p. 2.319-2.324

[17] Droste, H. and Kadel, G., *Measurement and Analysis of Wide Band Indoor Propagation Characteristics at 17 GHz and 60 GHz"*, Ninth Int. Conf. On Antennas and Propagation (Conf. Publ. No. 407), Vol. 2, Eindhoven

[18] Hashemi, H., *Impulse Response Modelling of Indoor Radio Propagation Channels"*, IEEE Journal on Selected Areas in Communications, Vol. 11, No. 7, September 1993, p. 967-978

[19] Hashemi, H., *The Indoor Radio Propagation Channel"*, Proc. of the IEEE, Vol. 81, No. 7, July 1993, p. 943-768

[20] Rappaport, T.S. and Fung, V., *"Simulation of Bit Error Performance of FSK, BPSK, and $\pi/4$ DQPSK in Flat Fading Indoor Radio Channels Using a Measurement-Based Channel Model""*, IEEE Transactions on Vehicular Technology, Vol. 40, November 1991, p. 731-740

[21] Rappaport, T.S., *Characterisation of UHF Multi path Radio Channels in Factory Buildings*, IEEE Transactions on Antennas and Propagation, Vol. 37, No. 8, August 1989, p. 1058-1069

[22] Saleh, A.A.M. and Valenzuela, R.A., *"A Statistical Model for Indoor Multipath Propagation"*, IEEE Journal on Selected Areas in Communications, Vol. SAC-5, No. 2, February 1987, p. 128-137

[23] Suzuki, H., *A statistical Model for Urban Radio Propagation"*, IEEE Transactions

on Communications, Vol. COM-25, No. 7, July 1977, p. 673-680

[24] Harris, F.J., *On The Use of Windowing for Harmonic Analysis with the Discrete Fourier Transform"*, Proceedings of the IEEE, Vol. 66, No. 1, January 1978, p. 51-83

[25] Shanmugam, K.S., *Digital and Analog Communication Systems*, John Wiley & Sons, Inc., University of Kansas, 1985

[26] Rappaport, T.S.,Thoma, B., and Fung, V., *Bit Error Simulation for $\pi/4$ DQPSK Mobile Radio Communications using Two-Ray and Measurement-Based Impulse Response Models* , IEEE Journal on Selected Areas in Communications, Vol. 1, No. 3, April 1993, p. 393-405

[27] Chennakeshu, S., and Saulnier, G.J., *Differential Detection of $\pi/4$-shifted-DQPSK for digital cellular radio* , Proc. IEEE Vehic. Techn. Conf., St. Louis., May 1991, p. 186-191

[28] Ha, T.T., *Digital Satellite Communications*, McGraw-Hill Communications series, second edition, New York, 1990

*****

Appendix A

Impulse response of a Raised Cosine filter with $\alpha = 0.5$

The transmit filter for raised cosine pulse shaping in the frequency domain is

$$H_{T,RC}(f) = \begin{cases} H_1(f) = \cos\left(\frac{2\pi f}{2R} + \frac{1}{4}\pi\right) & -\frac{3}{4}R \leq f \leq -\frac{1}{4}R \\ H_2(f) = 1 & -\frac{1}{4}R \leq f \leq \frac{1}{4}R \\ H_3(f) = \sin\left(\frac{2\pi f}{2R} + \frac{1}{4}\pi\right) & \frac{1}{4}R \leq f \leq \frac{3}{4}R \end{cases} \tag{A.1}$$

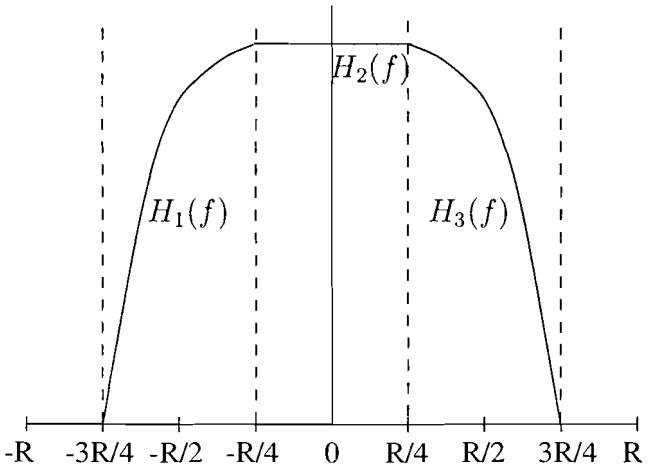

Figure A.1: **Transmit Filter Raised Cosine with $\alpha = 0.5$.**

$$h_{T,RC}(t) = \int_{-\infty}^{+\infty} H_{T,RC}(f) e^{j2\pi ft} df \tag{A.2}$$

$$= \int_{-\infty}^{+\infty} \left[H_1(f) + H_2(f) + H_3(f)\right] e^{j2\pi ft} df \tag{A.3}$$

$$= h_1(t) + h_2(t) + h_3(t) \tag{A.4}$$

Derivation of $h_1(t)$

$$\begin{aligned}
h_1(t) &= \int_{-\frac{3}{4}R}^{-\frac{1}{4}R} \cos\left(\frac{2\pi f}{2R} + \frac{1}{4}\pi\right) \cdot e^{j2\pi ft} df \\
&= \int_{-\frac{3}{4}R}^{-\frac{1}{4}R} \frac{1}{2}\left(e^{j\left(\frac{2\pi f}{2R}+\frac{1}{4}\pi\right)} + e^{-j\left(\frac{2\pi f}{2R}+\frac{1}{4}\pi\right)}\right) \cdot e^{j2\pi ft} df \\
&= \frac{1}{2}\int_{-\frac{3}{4}R}^{-\frac{1}{4}R} e^{j\left(\frac{\pi f}{R}+\frac{1}{4}\pi+2\pi ft\right)} + e^{-j\left(\frac{\pi f}{R}+\frac{1}{4}\pi-2\pi ft\right)} df \\
&= \frac{1}{2}\left[\frac{1}{j\left(\frac{\pi}{R}+2\pi t\right)} e^{j\left(\frac{\pi f}{R}+\frac{1}{4}\pi+2\pi ft\right)} + \frac{1}{-j\left(\frac{\pi}{R}-2\pi t\right)} e^{-j\left(\frac{\pi f}{R}+\frac{1}{4}\pi-2\pi ft\right)}\right]_{-\frac{3}{4}R}^{-\frac{1}{4}R} \\
&= \frac{1}{2j\left[\left(\frac{\pi}{R}\right)^2-(2\pi t)^2\right]}\left[Ae^{j\left(\frac{\pi f}{R}+\frac{1}{4}\pi+2\pi ft\right)} - Be^{-j\left(\frac{\pi f}{R}+\frac{1}{4}\pi-2\pi ft\right)}\right]_{-\frac{3}{4}R}^{-\frac{1}{4}R} \\
&= C\cdot\left[Ae^{j\left(\frac{\pi}{R}\cdot-\frac{1}{4}R+\frac{1}{4}\pi+2\pi t\cdot-\frac{1}{4}R\right)} - Be^{-j\left(\frac{\pi}{R}\cdot-\frac{1}{4}R+\frac{1}{4}\pi-2\pi t\cdot-\frac{1}{4}R\right)}\right] \\
&\quad - C\cdot\left[Ae^{j\left(\frac{\pi}{R}\cdot-\frac{3}{4}R+\frac{1}{4}\pi+2\pi t\cdot-\frac{3}{4}R\right)} - Be^{-j\left(\frac{\pi}{R}\cdot-\frac{3}{4}R+\frac{1}{4}\pi-2\pi t\cdot-\frac{3}{4}R\right)}\right]
\end{aligned} \tag{A.5}$$

where $A = \frac{\pi}{R} - 2\pi t$, $B = \frac{\pi}{R} + 2\pi t$ and $C = \frac{1}{2j\left[\left(\frac{\pi}{R}\right)^2-(2\pi t)^2\right]}$.

$$\begin{aligned}
h_1(t) &= C\cdot\left[Ae^{-j\frac{1}{2}\pi tR} - Be^{-j\frac{1}{2}\pi tR} - Ae^{j\left(-\frac{1}{2}\pi-\frac{3}{2}\pi tR\right)} + Be^{-j\left(-\frac{1}{2}\pi+\frac{3}{2}\pi tR\right)}\right] \\
&= C\left[-4\pi te^{-j\left(\frac{1}{2}\pi tR\right)} + 2j\frac{\pi}{R}e^{-j\left(\frac{3}{2}\pi tR\right)}\right]
\end{aligned} \tag{A.6}$$

and thus

$$h_1(t) = \frac{1}{2j\left[\left(\frac{\pi}{R}\right)^2-(2\pi t)^2\right]}\left[-4\pi te^{-j\left(\frac{1}{2}\pi tR\right)} + 2j\frac{\pi}{R}e^{-j\left(\frac{3}{2}\pi tR\right)}\right] \tag{A.7}$$

Derivation of $h_2(t)$

$$h_2(t) = \frac{R}{2}\frac{sin(\pi tR/2)}{\pi tR/2} = \frac{R}{2}sinc\left(\frac{1}{2}tR\right) \tag{A.8}$$

Derivation of $h_3(t)$

$$\begin{aligned}
h_3(t) &= \int_{\frac{1}{4}R}^{\frac{3}{4}R} \cos\left(\frac{2\pi f}{2R} - \frac{1}{4}\pi\right) \cdot e^{j2\pi ft} df \\
&= \int_{\frac{1}{4}R}^{\frac{3}{4}R} \frac{1}{2}\left(e^{j\left(\frac{2\pi f}{2R} - \frac{1}{4}\pi\right)} + e^{-j\left(\frac{2\pi f}{2R} - \frac{1}{4}\pi\right)}\right) \cdot e^{j2\pi ft} df \\
&= \frac{1}{2}\int_{\frac{1}{4}R}^{\frac{3}{4}R} e^{j\left(\frac{\pi f}{R} - \frac{1}{4}\pi + 2\pi ft\right)} + e^{-j\left(\frac{\pi f}{R} - \frac{1}{4}\pi - 2\pi ft\right)} df \\
&= \frac{1}{2}\left[\frac{1}{j\left(\frac{\pi}{R} + 2\pi t\right)} e^{j\left(\frac{\pi f}{R} - \frac{1}{4}\pi + 2\pi ft\right)} + \frac{1}{-j\left(\frac{\pi}{R} - 2\pi t\right)} e^{-j\left(\frac{\pi f}{R} - \frac{1}{4}\pi - 2\pi ft\right)}\right]_{\frac{1}{4}R}^{\frac{3}{4}R} \qquad \text{(A.9)} \\
&= C\left[Ae^{j\left(\frac{\pi f}{R} - \frac{1}{4}\pi + 2\pi ft\right)} - Be^{-j\left(\frac{\pi f}{R} - \frac{1}{4}\pi - 2\pi ft\right)}\right]_{\frac{1}{4}R}^{\frac{3}{4}R} \\
&= C \cdot \left[Ae^{j\left(\frac{\pi}{R}\cdot\frac{3}{4}R - \frac{1}{4}\pi + 2\pi t\cdot\frac{3}{4}R\right)} - Be^{-j\left(\frac{\pi}{R}\cdot\frac{3}{4}R - \frac{1}{4}\pi - 2\pi t\cdot\frac{3}{4}R\right)}\right] \\
&\quad - C \cdot \left[Ae^{j\left(\frac{\pi}{R}\cdot\frac{1}{4}R - \frac{1}{4}\pi + 2\pi t\cdot\frac{1}{4}R\right)} - Be^{-j\left(\frac{\pi}{R}\cdot\frac{1}{4}R - \frac{1}{4}\pi - 2\pi t\cdot\frac{1}{4}R\right)}\right] \\
&= C \cdot \left[jAe^{j\frac{3}{2}\pi tR} + jBe^{j\frac{3}{2}\pi tR} + 4\pi te^{j\left(\frac{1}{2}\pi tR\right)}\right] \\
&= C\left[4\pi te^{j\left(\frac{1}{2}\pi tR\right)} + 2j\frac{\pi}{R}e^{j\left(\frac{3}{2}\pi tR\right)}\right]
\end{aligned}$$

and thus

$$h_3(t) = \frac{1}{2j\left[\left(\frac{\pi}{R}\right)^2 - (2\pi t)^2\right]}\left[4\pi te^{j\left(\frac{1}{2}\pi tR\right)} + 2j\frac{\pi}{R}e^{j\left(\frac{3}{2}\pi tR\right)}\right] \qquad \text{(A.10)}$$

Conclusion

$$h_{T,RC}(t) = h_1(t) + h_2(t) + h_3(t) \qquad \text{(A.11)}$$

$$h_{T,RC}(t) = \frac{R}{2}sinc\left(\frac{1}{2}tR\right) + \frac{1}{\left(\frac{\pi}{R}\right)^2 - (2\pi t)^2}\left[\frac{2\pi}{R}\cos\left(\frac{3}{2}\pi tR\right) + 4\pi t\sin\left(\frac{1}{2}\pi tR\right)\right] \qquad \text{(A.12)}$$

or

$$h_{T,RC}(t) = \frac{1}{\pi\left(1 - 4t^2R^2\right)}\left[\frac{1}{t}\sin\left(\frac{1}{2}\pi tR\right) + 2R\cos\left(\frac{3}{2}\pi tR\right)\right] \quad . \qquad \text{(A.13)}$$

This corresponds to formula 7 in [27] if the normalisation is taken into account and $\alpha = 0.5$.

Appendix B

Q-function

The Q-function is defined as

$$Q(x) = \int_x^\infty \frac{1}{\sqrt{2\pi}} \cdot e^{-\frac{x^2}{2}} \cdot dx \quad , \tag{B.1}$$

and plotted in Figure B.1.

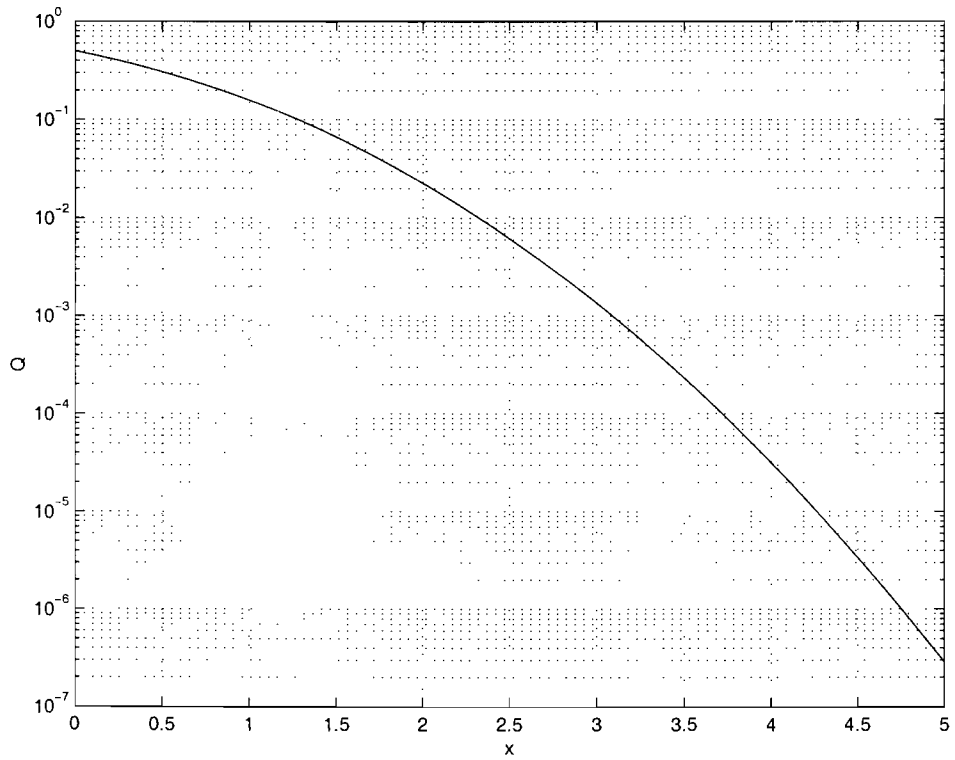

Figure B.1: **Plot of the Q-function**

Appendix C

Pictures of the Measurement Setup

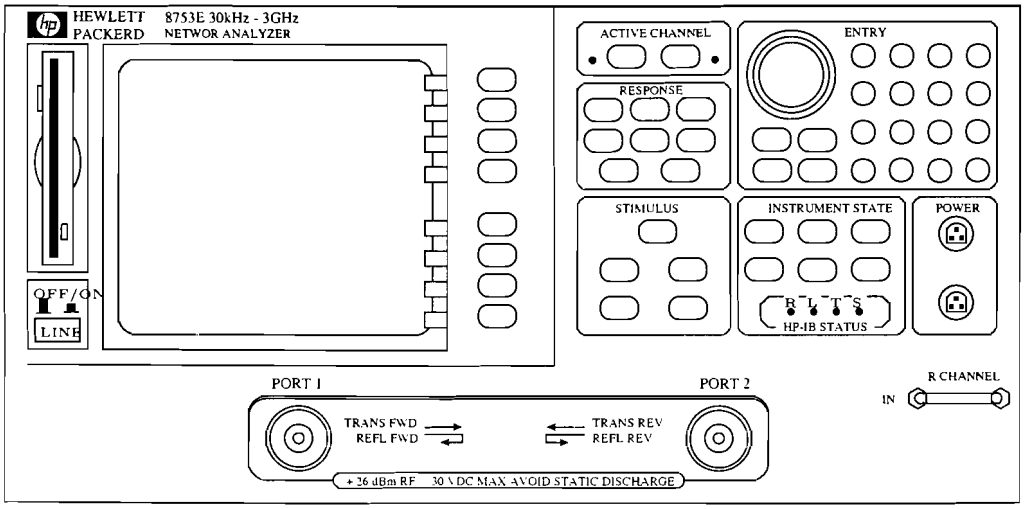

Figure C.1: **Network Analyzer.**

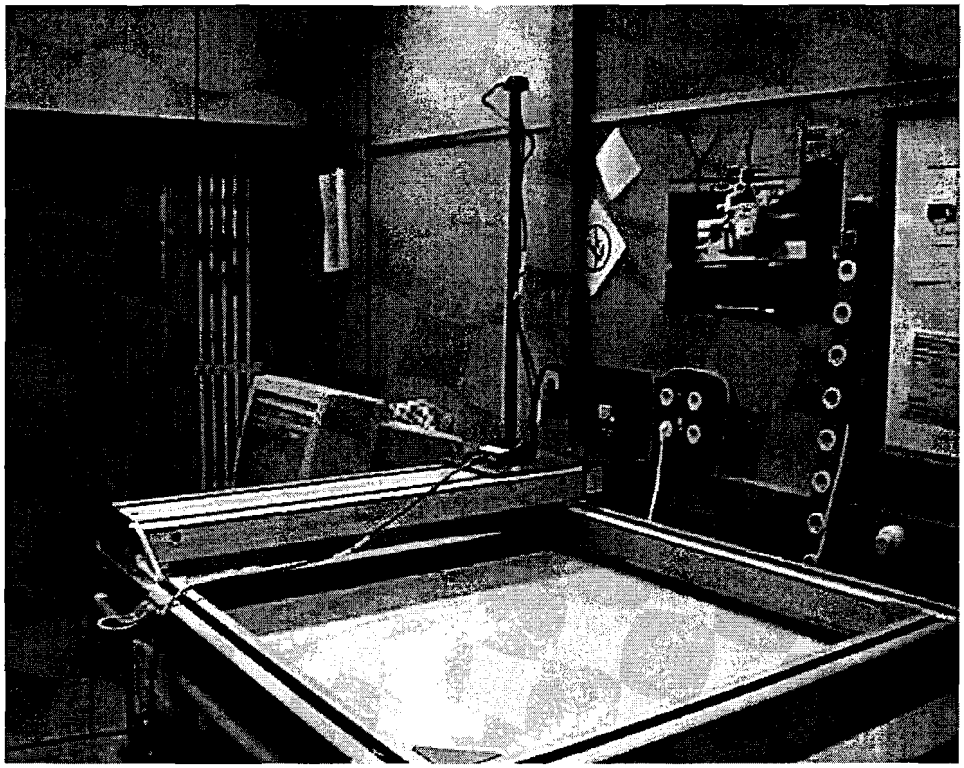

Figure C.2: **Photo of the xy-table.**

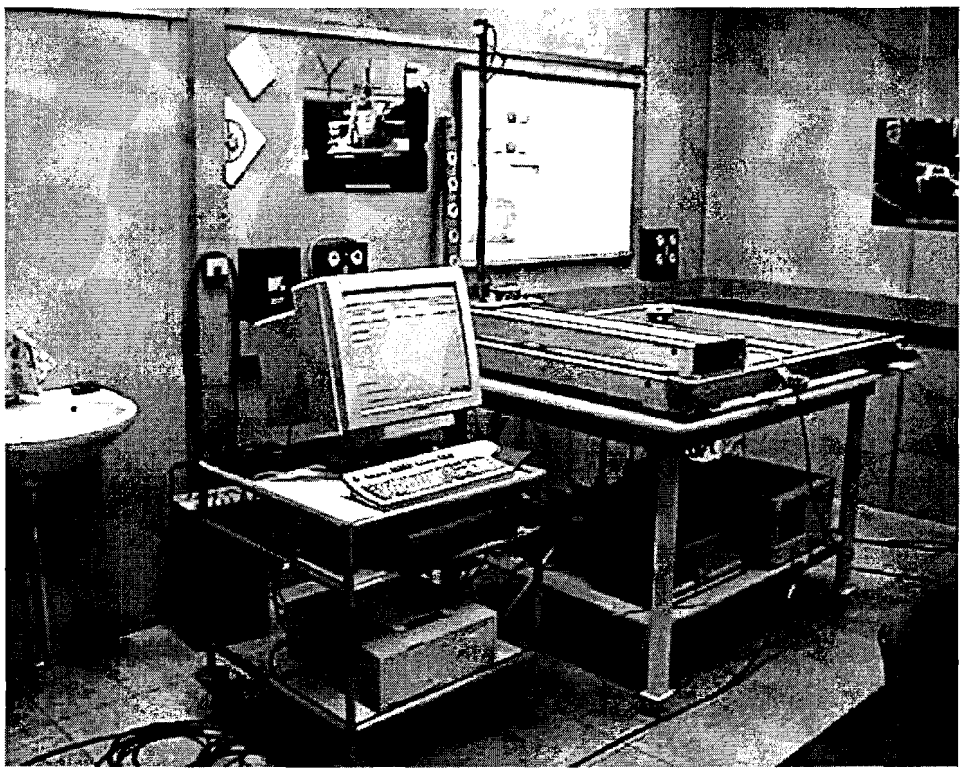

Figure C.3: **Photo of the measurement setup.**

Appendix D

Abbreviations

AWGN	Additive White Gaussian Noise
BER	Bit Error Rate
BPSK	Binary Phase Shift Keying
CDF	Cumulative Distribution Function
DECT	Digital Enhanced Cordless Telephone
DFT	Discrete Fourier Transform
DIFT	Discrete Inverse Fourier Transform
$\pi/4$ DQPSK	$\pi/4$ Differential Phase Shift Keying
FT	Fourier Transform
GSM	Global System Mobile Communications
HP VEE	Hewlett-Packard Visual Engineering Environment
IFT	Inverse Fourier Transform
ISI	Inter Symbol Interference
LOS	Line Of Sight
NLOS	Non Line Of Sight
OFDM	Orthogonal Frequency Division Multiplexing
PDF	Probability Density Function
PDP	Power Delay Profile
QPSK	Quadrature Phase Shift Keying
RF	Radio Frequency
RMS	Root Mean Square
TDL	Tapped Delay Line
UMTS	Universal Mobile Telephone System